Fabrication and Characterisation of Single-Molecule Transistors

Dissertation

zur Erlangung des
naturwissenschaftlichen Doktorgrades
der Julius-Maximilians-Universität Würzburg

vorgelegt von
Petra Fries
aus Untergruppenbach \ Baden-Württemberg

Würzburg April 2012

Eingereicht am: 30. April 2012

bei der Fakultät für Physik und Astronomie

Gutachter der Dissertation:

1. Gutachter: Prof. Dr. Laurens W. Molenkamp

2. Gutachter: Prof. Dr. Bert Hecht

Prüfer im Promotionskolloquium:

1. Prüfer: Prof. Dr. Laurens W. Molenkamp

2. Prüfer: Prof. Dr. Bert Hecht

3. Prüfer: Prof. Dr. Björn Trauzettel

Tag des Promotionskolloquiums: 08. Januar 2013

Damit das Mögliche entsteht,
muss immer wieder das
Unmögliche versucht werden.

Hermann Hesse

Contents

Zusammenfassung

Die Miniaturisierung von aktiven Komponenten und Bauteilen ist ein Schwerpunkt der Halbleiterindustrie. Die wachsenden Herausforderungen weiterhin dem Moor'sche Gesetz [1] zu folgen, indem die Anzahl der aktiven Bauteile auf einem Chip erhöht wird, die Herstellungskosten verringert werden und der Energieverbrauch minimiert wird, führt zu Bauelementgrössen von wenigen Nanometern. Diese Entwicklung wird wahrscheinlich in einigen Jahren durch die physikalischen Gesetze der Quantenmechanik begrenzt werden. Die kleinsten Bauelemente der aktuellen Generation von Halbleiterbauteilen sind 22 nm [2]. In Zukunft wird diese Grösse vergleichbar mit der Grösse von Einzelmolekülen sein. Bereits 1976 hatten Avriam und Ratner [3] die Idee einzelene Moleküle als aktive Komponenten in elektronischen Bauteilen zu nutzen. Sie schlugen vor, dass ein molekularer Gleichrichter bestehend aus einem Donator-Akzeptor π-Elektronensystem, getrennt durch eine σ-gebundene Tunnelbrücke, die Eigenschaften eines p-n Übergangs; einer Diode, zeigen würden. Diese Idee begründete das Forschungsgebiet der molekularen Elektronik. Eine interessante Zielsetzung ist hierbei, ein einzelnes Molekül als aktive elektronische Komponente zu nutzen, beispielsweise als Transistor, Schalter oder Speicherzelle.

Für die industrielle Anwendung könnten vorallem ein- und zweidimensionale Polyphenylene interessant sein. Diese Moleküle werden auch als Graphenmoleküle bezeichnet. Sie können mit verschiedenen Endgruppen, welche beispielsweise eine Bindung zu Metallelektroden gewährleisten, synthetisiert werden. Ferner können Moleküle mit speziellen Atomen oder Atomgruppen, welche dem Molekül eine definierte Funktion geben, hergestellt werden. Die Moleküle sind in verschiedenen Chemikalien lösbar und daher für selbstanbindende Prozesse aus chemischer Lösung geeignet.

Diese Arbeit zeigt ein dreidimensionales Bauteil, welches sich für die Charakterisierung von Einzelmolekülen eignet. Desweiteren kann das Bauteil auch als Einzelmolekültransistor verwendet werden. Das Bauelement besteht aus zwei Elektroden zwischen denen das Molekül gebunden ist und einer lokalen Gateelektrode auf der die beiden anderen Elektroden lithographisch sturkturiert sind. Es werden zwei verschiedene Methoden zur Herstellung der beiden Goldelektroden, Bias- und Groundelektrode, gezeigt. Zum Einen kann ein Nanokontakt direkt über Elektronenstrahllithografie strukturiert werden, außerdem besteht die Möglichkeit den Nanokontakt durch gesteuerte Elektromigration zwischen

1

zwei Elektroden zu erzeugen.

Die Herstellung von zwei Nanoelektroden durch hochauflösende Elektronenstrahllithografie wird gezeigt. Durch das Schreiben von Einzel-Pixel-Linien werden Elektronen mit einer Breite von 25 nm und einem Abstand von weniger als 10 nm strukturiert. Die Prozessausbeute von Elektroden mit einem Abstand von weniger als 5 nm liegt zwischen 50 und 60 %. Dieser Herstellungsprozess eigent sich zur Messung von einzelnen Molekülen, welche aus Lösung aufgebracht werden. Weiterhin bietet dieses Verfahren die Möglichkeit Nanodrähte oder auch Graphen-Scheiben-Moleküle mit Grössen zwischen 10 und 20 nm zu kontaktieren.

Desweiteren wird ein lithografischer Prozess zur Stukturierung der Gateelektrode entwickelt. In dieser Arbeit verwenden wir Aluminium mit einer Oxidschicht auf der Oberfläche als Gateelektrode. Dieses Material zeigt einen hohen Gate-Kopplungs-Faktor, allerdings ist es schwierig es als stabile und glatte Schicht herzustellen [4]. Wichtig ist hierbei, das Aluminium bei der Temperatur flüssigen Stickstoffs (77 K) aufzudampfen und die Oberfläche direkt nach dem Aufdampfen in einer kontrollierten Sauerstoffatmospähre zu oxidieren. Die genaue Methode wird in den Kapiteln 3 und 4 beschrieben. Durch Messen der Stabilität des Gates zeigt sich, dass 80 Prozent der Bauteile einen Leckstrom von weniger als 5 pA im Messbereich von -2 V bis 2 V aufweisen. Die Glattheit der Oberflächenschicht des Aluminiumoxides wird mittels Atom-Kraft-Mikroskop bestimmt und beträgt ungefähr 1 nm.

Für die meisten während dieser Arbeit hergestellten Bauelemente wird der Nanokontakt zwischen Bias- und Groundelektrode mittels Elektromigration ausgebildet. Die Nanostrukturen werden mittels Fotolithografie, Elektronenstrahllithografie und Schattenaufdampfen der Metallschichten erzeugt. Unsere Fotomaske erlaubt die Herstellung von 1400 Transistoren in einem Prozessdurchlauf. Der ausführliche Prozess ist in Kapitel 4 beschrieben. Die anschließende Elektromigration wird mittels einem ADwin-light-16 System für Echtzeitmessungen durchgeführt. Verschiedenste Parameter für die gesteuerte Elektromigration werden an mehr als 1000 Nanostrukturen an einem Nadelmessplatz getestet. Die Ergebnisse werden in Kapitel 5 dargestellt und diskutiert. Weitere Tests werden in einem Tieftemperaturkryostaten bei 4.2 K durchgeführt. Dabei zeigt sich dass 58 % der Nanokontakte kleiner als 5 nm sind.

Die Funktion der dreidimensonalen Bauelemente wird mittels C_{60} Buckyball-Molekülen untersucht. Hier werden Experimente an einem Tieftemperatur-Nadelmessplatz bei Temperaturen von 15 bis 20 K durchgeführt. Außerdem werden auch Messungen in einem Mischkryostaten bei Tiefsttemperatur durchgeführt. Die Messungen in der Probestation zeigen dass Bauteile ohne Moleküle gelegentlich charakteristische Kurvenverläufe in der differentiellen Leitfähigkeit aufweisen. Diese Peaks können durch Goldkörner, die sich

während der Elektromigration im Nanokontakt anlagern, erklärt werden. Das Messsignal von Gold liegt in der selben Grössenordnung wie die magntische Leitfähigkeit, die für die C_{60} Moleküle erwartet werden und erschweren dadurch eine Unterscheidung. Aus diesem Grund werden weitere Messung bei wenigen Millikelvin durchgeführt. Hierbei konnte eine Aufspaltung der Coulomb-Diamanten im magnetischen Feld beobachtet werden. Die differentielle Leitfähigkeit konnte in Abhängigkeit von der Biasspannung in vier unterschiedliche Signaturen aufgegliedert werden. Einge der Bauteile zeigten Peaks, deren Lage von der Gatespannung abhängt. Es werden weiterhin Messungen im magnetischen Feld durchgeführt. Eine Zeeman-Aufspaltung der Peaks kann beobachtet werden. Die Werte des Landé-Faktors, welche aus der Aufspaltung errechnet werden variieren stark. Für eine Interprätation dieser Ergebnisse sind ausführliche Charakterisierungen weiterer Nanokontakte notwendig.

Ferner werden auch Messergebnisse von verschiedenen Polyphenylen-Molekülen gezeigt. Es ist möglich Coulomb-Diamant-Strukturen und auch Zeeman-Aufspaltung zu messen. Ein Landé-Faktor von 5,8 wurde für kurzkettige Polyphenylene gemessen. Dieser Wert unterscheidet sich vom Wert für C_{60} Moleküle ebenso, wie von dem bekannten Wert von Gold, dem Elektrodenmaterial. Es könnte sich hier um einen typischen Wert für die graphenartigen Moleküle handeln. Die langkettigen Polyphenylene zeigen Werte für die differentielle Leitfähigkeit von 0,011 bis 9,0 $\frac{e^2}{h}$ und einem g-Faktor von 3,5. Für beide Moleküle werden nur wenige Bauelemente charakterisiert, diese ersten Ergebnisse sind sehr vielversprechend. Für eine ausführliche Untersuchung der Moleküle muss eine große Anzahl von Einzelmolekültransistoren gemessen werden.

Summary

A primary focus of the semiconductor industry is the miniaturisation of active devices. The challenge to follow Moores law [1] in increasing the number of active devices on a chip, lowering the cost for a chip and minimising the power consumption, will lead to device sizes of a few nanometer. This development will eventually be limited by the physical laws of quantum mechanics. The smallest features in the current generation of semiconductor devices is 22 nm [2]. In some years, the size will be comparable to the size of single molecules. The idea to use molecules as active building blocks in electronic devices was already suggested in 1974 by Aviram and Ratner [3]. They proposed that a molecular rectifier consisting of a donor π-system and an acceptor π-system, separated by a σ-bonded tunneling bridge, would show the characteristic of a p-n junction; a diode. With this idea the field of molecular electronics was founded. One interesting objective is now to use one single molecule as an electronic building block: as transistor, switch or memory cell.

One class of molecules which could become interesting for industry consists of one- and two-dimensional polyphenyles; so called graphene molecules. These molecules can be synthesised with different end groups for assuring a binding to metal electrodes, but also with other atoms or atom groups which could give a defined function to the molecule. They are soluble in various chemicals and therefor suitable for a self-assembling process from a chemical solution.

This thesis presents an electronic three-terminal device suitable for the characterisation of single molecules which can also be used as a single-molecule transistor. This device consists of two electrodes between which the molecule is bound and a local back gate electrode on which the other two electrodes are structured. Two different methods of fabrication of the two gold electrodes, bias and ground electrode, are presented: direct structuring of a nanogap by electron-beam lithography and the forming of the nanogap between two electrodes using controlled electromigration.

The fabrication of two nanoelectrodes by high resolution electron-beam lithography is demonstrated. By writing of single-pixel-lines, electrodes with a width of 15 nm and a separation of less than 10 nm are produced. The yield of electrodes with separation less

than 5 nm is between 50 and 60 %. This process is suitable for measurements on single molecules applied from a solution, and also to contact nanowires or graphene disks with sizes between 10 and 20 nm.

Further a process for structuring the gate electrode is developed. In our work we use aluminum with an oxide layer on top for the gate electrode. This material shows a high gate coupling but is difficult to fabricate as a smooth and stable layer [4]. Important is here to evaporate the aluminum at liquid nitrogen temperature and to oxidize the layer directly after evaporation, in a controlled oxygen atmosphere. The exact method is presented in chapters 3 and 4. Measurements of the gate stability have shown that for 80 percent of the devices, the leakage current for voltages between -2 V and 2 V is below 5 pA. The smoothness of the surface of the Al_2O_3 layer is measured by atomic force microscope to be around 1 nm.

In most of the three-terminal devices fabricated during this thesis, the nanogap between the bias and ground electrode is formed by electromigration. The nanostructures are produced with photolithography, electron-beam lithography and shadow evaporation of the metal. Our photomask allows the fabrication of 1400 transistors with one process run. The detailed process is described in chapter 4. The electromigration is performed with an ADwin-light-16 system for real time measurements. Various parameters for electromigration are tested on more than 1000 structures in a probe station. The results are discussed in chapter 5. Further tests in a cryostat at 4.2 K are performed. Here 58 % of the structures were smaller than 5 nm.

The performance of the three-terminal devices is tested with C_{60} buckyball molecules. Tests are performed on a cryogenic probe station between 15 and 20 K and in a dilution refrigerator at base temperature. The measurements in the probe station showed that three-terminal devices without molecules occasionally exhibits features in the differential conductance. These peaks result form gold grains remaining in the gap after electromigration. The signal of gold is in the same order of magnetisation conduction as the expected signal of C_{60} and makes a distinction difficult. Therefore measurements at mK temperature are performed. Here a splitting of the coulomb diamonds in a magnetic field could be observed. The differential conductance in dependence of the bias voltage could be classified in four different signatures. Some of the devices showed peaks whose position depends on the gate voltage. Here also measurements in a magnetic field are performed. A Zeeman splitting of the peaks is observed. The values of the Landé-factor calculated out of the splitting vary strongly and are not clearly understood.

Further measurements with different polyphenyle molecules are performed. It was possible to show Coulomb diamond structures and also zeeman splitting. A Landé-factor of 5.8 was measured for the short chain polyphenylene molecules. This value differs from

the results measured for C_{60} and also from the g-factor of gold, the electrode material. It could be typical for the graphene like molecules. The long chain polyphenylenes showed differential conductance from 0.011 to 9.0 $\frac{e^2}{h}$ and a g-factor of 3.5. For both molecules only a small number of devices were measured, but these first results are very promising. For a more detailed characterisation of the molecules a huge number of these single-molecule transistors needs to be investigated.

Chapter 1

Introduction

One of the most important objectives of the semiconductor industry is the miniaturisation of the active devices and therefore the reduction of the costs of the electronic components on chips. In the nineteen sixties Moore predicted that the number of logical devices on a single semiconductor chip will double every two years [1]. In the first decades after Moores prediction the semiconductor industry had to solve challenges such as mass production, the introduction of new materials and reliability. Nowadays the focus has changed. The semiconductor industry is forced to minimize fabrication costs, to improve the logical devices in performance, speed and power consumption and push further the limit of miniaturisation, which requires the application of new fabrication technologies. On the other hand, limitation imposed of the physical laws of quantum mechanics, forces the investigation of new materials and new fabrication technologies. The actual generation of semiconductor devices is fabricated with a smallest feature of 22 nm, compared to 10 μm in 1971 [2]. These technologies include the use of high resolution UV-lithography, the use of oxide layers which are only a few atomic layers thick and further the application of new materials. The on-going miniaturisation of electronic devices will reach some nanometer in the next few years. This is the size of single molecules. Hence, individual molecules will become one possibility to use as logical elements. One advantage of molecules is that their electrical properties can be modified by chemical synthesis. The engineering of specific physical properties and functionalities is possible. Further, molecules are self-assembling on surfaces in order to build molecular clusters or monolayers.

The idea of using molecules as electronic building blocks was already proposed in 1974 by Aviram and Ratner [3]. They proposed that a molecular rectifier consisting of a donor π-system and an acceptor π-system, separated by a σ-bonded tunneling bridge, would show the characteristic of a p-n junction, a diode, and in so doing, founded the field of molecular electronics. Since this time various approaches to develop molecular devices are investigated. Here, molecular devices are structures containing a very small number of single molecules or even only one molecule. The focus of single-molecule devices lies on the use of a molecule as an electronic building block: as transistor, switch or memory

cell. Research in this field unites chemistry and physics. Chemistry gives the possibility to create new molecules with special functionalities. Physics is needed to create suitable nanostructures to contact the molecules and study the transport properties.

One interesting class of molecules are the one- and two-dimensional polyphenylenes [5]. These molecules are also called graphene molecules. Graphene is a monolayer of graphite in a honey-comb like latter of carbon atoms. It has several interesting properties like thermal stability up to 500 °C, being inert to most gases, showing a very high stability of its lattice structure and having a high electrical mobility. Graphene has been theoretically studied for decades, and a good overview of the theoretical results can be found in [6] and [7]. Since 2005 it has been possible to extract single graphene layers from graphite. Geim and Novoselov presented a very simple method to exfoliate graphene from graphite [8], [9]. This was the birth of one of the currently most dynamic research topics in semi-conductor physics [10], with more than 5000 papers. The material has been published in international journals over the past 6 years. Main topics in graphene research are the investigation of the quantum hall effect [8], [11], spin-transport and manipulation experiments [12], electronic transport through suspended graphene [13] and graphene quantum dots [14]. The fabrication of transport structures on graphene, like quantum dots, is limited by the resolution of the available lithographic methods, and structures with sizes smaller than 20 nm are very difficult to fabricate. The smallest quantum dot structures reported have features of 30 nm [15], [16].

For the use of graphene in industries the application of the graphene-like molecules becomes interesting. It is possible to synthesis the molecules of different sizes from 1.4 nm (with 11 benzene rings C_{42}) up to 3.5 nm (with 91 benzene rings C_{222}) [5]. Some of these molecules are soluble and therefore good candidates for self-assembling processes. The application of these molecules in a single-molecule transistor opens various possibilities for research and industry.

The subject of this thesis is the fabrication of different three-dimensional devices for single-molecule measurements. Further the reliability of the devices is tested and measurements on C_{60} buckyball molecules are performed. Finally, first results of the measurements on one-dimensional graphene-like molecules, polyphenylenes, are presented. The content of the thesis is outlined below:

Chapter 2 gives a general overview about transport mechanisms in single-molecule transistors. Beginning with modeling the single-molecule contact as a quantum dot, the energy and electrical models are described. This is followed by a discussion of first order tunneling and Coulomb blockade. Furthermore, the three main higher order tunneling effects are explained. Elastic and inelastic co-tunneling play an important role for single-molecule transport. The occurrence of the Kondo effect for transport measurements and

the Zeeman splitting in magnetic fields is also described. The chapter closes with a short presentation of C_{60} and Pentaphenylenes.

Chapter 3 provides the ground work needed for the development of the fabrication of three-terminal devices for single-molecule measurements. The principle of the lithography process is explained. This is followed by experiments to find basic information about the properties of the needed resists. Here the focus lies on double-layer resist systems and the use of photoresists for evaporation at liquid nitrogen temperature. Finally, high resolution electron-beam lithography processes are presented. First results for nanogaps directly structured by electron-beam lithography are shown.

Chapter 4 contains the complete device fabrication process steps of optical and electron-beam lithography are explained and the results are presented. The different metal evaporation methods are discussed in detail. Further the preparation of the molecules and their application on the nanocontancts is explained.

Chapter 5 focuses on the creation of the nanogaps through controlled electromigration. First a theoretical overview of the electromigration process is given. The algorithm programmed for controlled electromigration is described and the results for different electromigration parameters are presented.

Chapter 6 presents the measurements on single-molecule contacts. Beginning with a description of the measurement set-up, the room-temperature measurements on C_{60} are discussed. Further, experiments in a dilution refrigerator are performed. Here, also the behavior of the molecules a magnetic field is observed. A discussion of the results follows the different measurements of the C_{60} molecules. The focus of this discussion lies on the distinction between molecule or gold grain, remaining after electromigration, in the nanocontact. This chapter is closed by the presentation of the results of the measurements on different pentaphenylene molecules. These molecules are investigated with this measurement method for the first time.

Chapter 2

Theory

A phenomenological description of the transport in single-molecule transistors is given in this chapter. It should be sufficient to understand the single-molecule transport measurements. The coupling of the molecules to the metallic leads and the gate electrode is discussed. The single-molecule transistor is considered in the model of a single quantum dot. The focus lies on the different tunneling effects responsible for the transport of single electrons through the molecule. Further, the Kondo effect and Zeeman splitting are described.

2.1 Transport through a single molecule

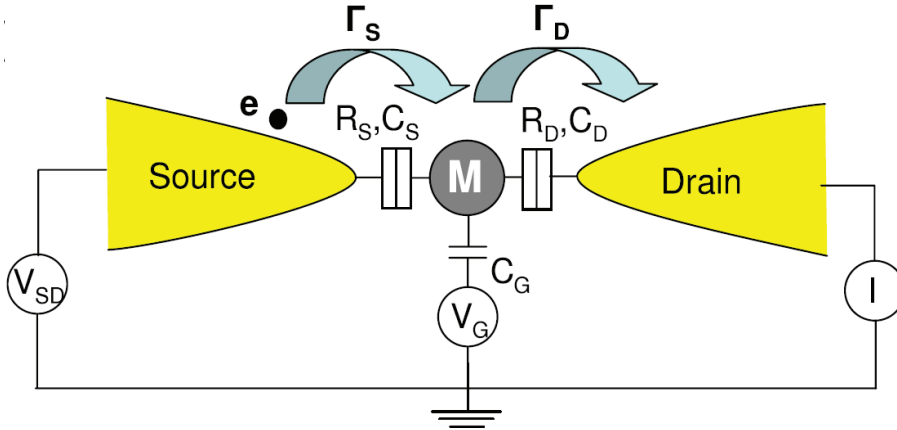## 2.1.1 Electrical model of a single-molecule transistor

Figure 2.1: *Electronic model of a single-molecule transistor. The molecule is coupled to the source and drain electrodes via a tunnel resistance and a capacitance. The coupling to the gate electrode is ideally only by a capacitance. (The figure is adapted from Osorio et al., 2008 [17].)*

The transport through a single molecule in a three-terminal device can be modeled as a quantum dot (QD) coupled between two electrodes (source and drain) [18], [19],[20]. Figure 2.1 shows a schematic of this model [17]. The molecule is ideally situated between source and drain electrode and coupled to them by tunnel barriers (Γ_S, Γ_D) with a resistance (R_S, R_D) and a capacitance (C_S, C_D). Initially the molecule is in the ground state. The coulomb repulsion of the electrons of the molecule implies that a discrete charging energy has to be overcome to a transfered through the dot. The tunneling rate depends on the tunneling barrier, this means the coupling of the QD to the metal leads. The total coupling, $\Gamma = \Gamma_S + \Gamma_D$, gives the broadening of the molecular levels. Γ can be charge-state dependent because the overlap between the wave functions of the electrodes and the molecule can vary strongly with the number of electrons N.

The gate electrode is ideally coupled only by a capacitance to the molecule. The gate capacity C_G determines the external influence on the electronic structure of the molecule. The gate serves to adjust the chemical potential of the molecule compared to the chemical potentials of source and drain electrodes. A higher gate capacitance implies that less voltage is needed to charge the molecule or further that more excited states of the molecule can be tuned. In a real three-terminal device the gate is coupled to parasitic resistances. The resulting leakage currents can be neglected if the parasitic resistance is high compared to the tunneling resistance.

2.1.2 Energy model of a single-molecule transistor

The discrete electronic spectrum of a single-molecule transistor in thermal equilibrium is illustrated in figure 2.2 a). The leads are metallic and the states are filled up to the Fermi energy $E_F=\mu_S=\mu_D$ of the system. The quantum dot is coupled to the reservoirs by tunneling barriers (see above) which are usually of the order of some electron volts (eV) and can be resolved at cryogenic temperatures. The energy splitting of a QD in the model of a particle in a spherical box scales like

$$\Delta E \propto \frac{1}{(2R)^2} \tag{2.1}$$

with R is the radius of the dot. With formula 2.1 follows that bigger molecules need lower measurement temperatures for a suitable spectral resolution. Further higher gate voltages are required to access to excited states of smaller molecules.

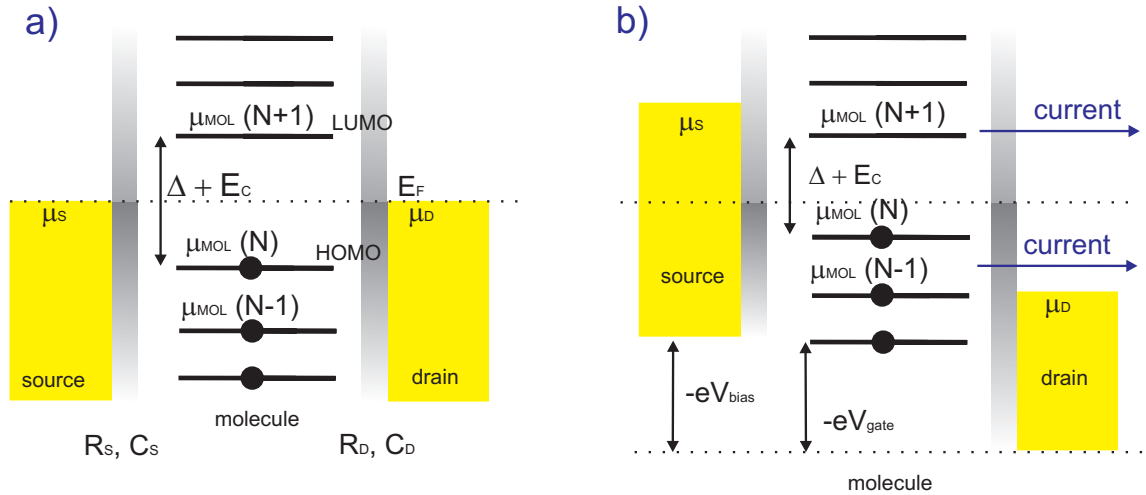Figure 2.2 a) shows a molecule without applied gate or bias voltage. The Fermi level is

Figure 2.2: *Energy models of a single-molecular transistor: a) The transistor is in thermal equilibrium. The center of the HOMO-LUMO-gap aligns to the Fermi energy of the electrodes. The total energy between HOMO and LUMO is the addition energy E_{add}. b) The application of a bias or a gate voltage can open transport channels for electron transport.*

situated between the highest occupied molecular orbital (HOMO) and the lowest unoccupied molecular level (LUMO) [21]. In this state the molecule can be neutral or already be charged with the number of N electrons on the dot. The minimum energy to add the Nth electron to the QD is the electrochemical potential $\mu(N)$:

$$\mu(N) = U(N) - U(N-1) \tag{2.2}$$

where U(N) is the total ground state energy for N electrons on the dot. The electrochemical potential $\mu(N)$ indicates the states available for transport. For the calculation of the total energy needed to add an electron to the QD, the addition Energy E_{add}, the coulomb interaction between electrons has to be considered. This energy, called charging energy E_C is given by

$$E_C = \frac{e^2}{C} \tag{2.3}$$

with C is the total capacitance of the system: $C = C_S + C_D + C_G$.
For the addition energy E_{add} follows:

$$E_{add} = E_C + \Delta \tag{2.4}$$

where Δ is the quantum level spacing. Therefore, the addition energy is the sum of an electrostatic energy of the molecule and a part of energy corresponding to the energy spectrum of the QD.

Figure 2.2 b) shows the quantum dot with applied voltage causing a current flow through the dot. The bias voltage (potential difference between source and drain) separates the electrochemical potential of source and drain electrode: $-eV_{bias} = \mu_S - \mu_D$.

Unoccupied molecular states can contribute to the electron transport if the bias voltage is high enough. An increase of the bias voltage will open more and more transport channels. The gate voltage applies an external potential which can charge or discharge the molecule and therefore shift the electronic ladder up and down. The gate voltage shifts the molecular levels through the chemical potential of the electrodes. Here, transport channels of the molecule will be opened if an molecular level is in resonance with the chemical potentials of one of the metal leads: $U(N) = U(N-1)$. Now, the system is no longer in Coulomb blockade and a current can flow between source and drain electrode in the case that a molecular level is between μ_S and μ_D. The oscillations of conductance caused by the gate voltage are called Coulomb oscillations. Out of resonance the current is suppressed and the system is in Coulomb blockade. The Coulomb peaks of high conductance are broadened by the finite temperature and the height of the tunneling barriers.

The four possible cases to obtain current flow through the molecule are illustrated in figure 2.3. The illustration shows the situations for which the transistor is conducting or blocking. The region of blocking are called Coulomb diamonds. The points on the interface between two diamonds are the charge degeneracy points, where a current can flow even if the bias voltage is infinite small. The electrochemical potential depends linearly
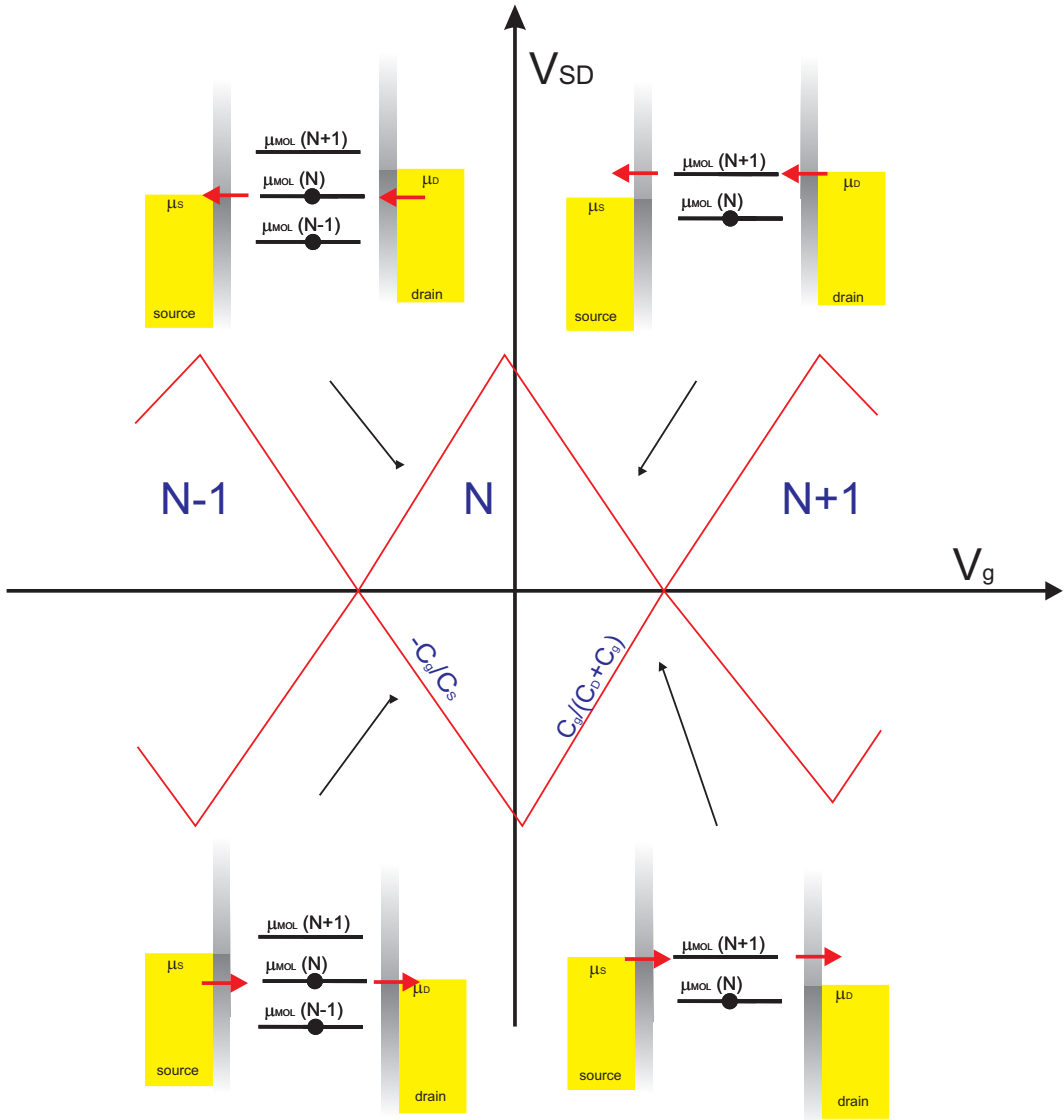
Figure 2.3: *Stability diagram of a quantum dot. Four different cases for a current flow through the QD are presented. Therefor, the coulomb blockage must be over crossed. The chemical potential of the QD (molecular energy levels) has to be equal to the chemical potentials of the source or the drain electrode.*

on the applied external voltages. Therefore it is possible to get a quantitative information about the different capacitances of the system by determining the slopes of the diamonds boundaries:

$$positive\ slope:\quad \alpha_+ = C_g/(C_D + C_g);\quad negative\ slope:\quad \alpha_- = -C_g/C_S \quad (2.5)$$

The gate coupling is defined as

$$\beta = \frac{C_g}{C} = \frac{\alpha_+ * \alpha_-}{\alpha_+ + \alpha_-} \tag{2.6}$$

and can be determined from the slopes of the Coulomb diamonds. Further it is possible to measure the size of the diamond.

2.2   First order electron tunneling

At cryogenic temperatures, the charging energy and the level spacing are much smaller than the thermal energy (E_C, $\Delta \ll k_B T$). Another important parameter to describe transport in a quantum dot is the total coupling Γ. In the weak coupling regime Γ is very small ($\Gamma \ll E_C$, Δ). The transport measurements are normally illustrated in stability diagrams as shown in figure 2.3 above. An example for quantitative measurement results is schematically shown in figure 2.4 a). The Coulomb diamonds have in first order zero conductance, higher order tunneling can cause small currents, which are usually negligeable in weak coupling regime. The number of electrons on the quantum dot in the Coulomb diamonds is an integer value (N). For higher gate voltages the next diamond is accessible and the charge on the molecule increases by N+1. It is difficult to know exactly the charge state of the molecule since the molecule can already be charged without applied voltages. This fact can make it difficult to identify the neutral charge state of the molecule.

Additionally excited states are illustrated in figure 2.4 a). The white lines, which are parallel to the diamond edges, show excited states contributing to the conductance. The energy of these excited states ΔE can be distinguished by the distance between the zero-bias axis and the crossing point of the diamond edge [22].
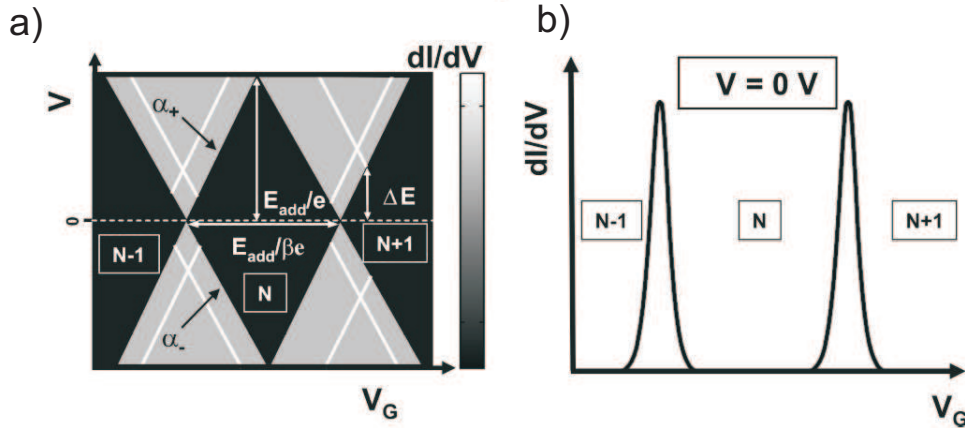

Figure 2.4: *Transport in the weak coupling regime: a) Stability diagram of a QD. The map shows the differential conductance plotted versus gate and bias voltage. The white lines illustrate the transport through excited states. b) Plot of the differential conductance dI/dV versus the gate voltage. The Coulomb peaks are measured at small bias voltage. (The figure is adapted from Osorio et al., 2008 [17].)*

The Coulomb blockade can be overcome by resonant tunneling. If a charge state $\mu_{Mol}(\mathrm{N})$ lies between the chemical potentials of source and drain electrode: $\mu_S < \mu_{Mol}(\mathrm{N}) < \mu_D$, then resonant tunneling can occur. The shift of the chemical potentials can be caused by

sweeping the bias or the gate voltage. Figure 2.4 b) shows the differential conductance measured for a sweep of the gate voltage at low bias voltage. The peaks of the differential conductance are Coulomb oscillations (see above) [23]. At these points, the two charge states of the quantum dot have the same energy. This fact allows an electron to freely hop on or off the QD.

2.3   Higher order tunneling processes

In the last section the transport through real states was described. For weak coupling of the molecule to the electrodes, only sequential tunneling effects have non-negligeable contribution. All observed electron tunneling processes are first order tunneling processes. For stronger coupling, higher order electron tunneling has to be considered. In the strong coupling regime ($\Delta \gg E_C$, $k_B T$, $\Delta(N)$), electron tunneling is dominated by elastic coherent tunneling [17]. A typical effect of this tunneling is that the Coulomb blockade is no longer clearly visible. Quantum fluctuations of the molecular charge cause smeared Coulomb diamonds. The resistance in this regime is close to the resistance quantum $R_Q = h/e^2 = 25.8$ kΩ. The strong coupling regime will not be discussed in detail. Detailed descriptions can be found in [24], [25]. There exists a third regime between weak and strong coupling: the intermediate coupling regime (1 MΩ $> R_S$, $R_D > h/e^2$). Three effects of higher order tunneling taking place in the intermediate coupling regime, are explained in this section: the elastic and inelastic co-tunneling and the Kondo effect.
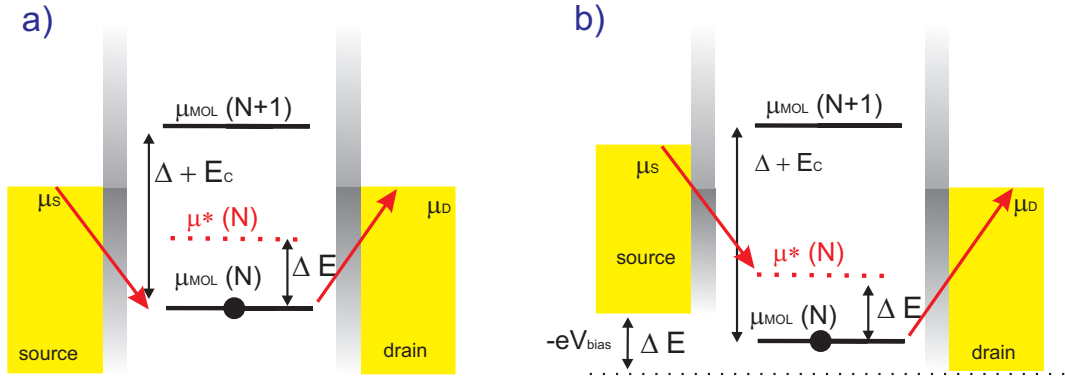
2.3.1   Elastic co-tunneling

Figure 2.5: *Transport in the intermediate coupling regime. a) Elastic co-tunneling: An electron jumps to the drain (virtual state) and is immediately replaced by an electron from the source. b) Inelastic co-tunneling: The N-th electron on a molecule state can jump from the ground state to the drain (virtual state) to be immediately replaced by an electron from the source, when $|eV_{bias}| = \Delta E$.*

An elastic co-tunneling process is shown in figure 2.5 a). Higher order tunneling processes occur through so called *virtual states*, i.e. energetically forbidden states. For coherent transport the co-tunneling process happens as a single quantum process. It is called co-tunneling because two electrons are involved in the process. An electron tunnels off the molecule from virtual state, while another electron tunnels into the molecule replacing the first electron. Considering Heisenbergs energy-time uncertainty principle this is allowed to happen in the same quantum process without violating the energy conser-

vation. The initial and the final state of the elastic co-tunneling process have the same
energy, but one electron is transported through the molecule during the process.
Elastic co-tunneling causes a rise of the conductance in the region where the transport is
forbidden by the Coulomb blockade. Therefore is a non zero background conductance in
these regions.

2.3.2 Inelastic co-tunneling

Inelastic co-tunneling adds energy to the molecule. This means that the molecule is in an
excited state after the tunneling process. Figure 2.5 b) shows such an event. The electron
tunneling into the molecule arrives here in a different excited state, than the one vacated
by the electron tunneling off the molecule. The energy difference of these two states is
ΔE. This difference of the chemical potentials can be compensated by applying a bias
voltage ($eV_{SD} = \Delta$E) as shown in figure 2.5 b). Inelastic co-tunneling causes a step in the
differential conductance. This step appears if the bias voltage compensates the difference
of the chemical potentials between the two states of the tunneling process: $eV_{SD} \geq \Delta$E.
The electron in the excited state will afterwards relax into the ground state.
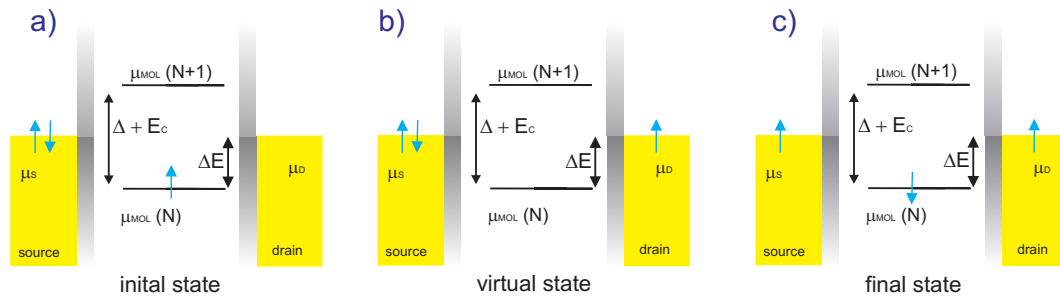
2.3.3 Kondo effect

Figure 2.6: *Spin-flip co-tunneling: a) The molecule has one spin-up electron in the ground
state. b) The electron jumps out of the molecule state (virtual state) to the drain. c) The
electron is immediately replaced by a spin-down electron from the source. A spin-flip event
is involved in the co-tunneling process.*

Another co-tunneling effect appears if the electron spin is considered, the *Kondo effect*
[26]. A molecule can have a net spin if a single localized state is spin-degenerated and only
partially filled. In the case that the QD has a net spin in its ground state, the transport of
one electron between the electrodes can be accompanied by a spin-flip event. A molecule
has a net spin and therefore a magnetic moment for an odd number of electrons, this
means one electron is unpaired and the spin is S = 1/2. There exist many theoretical
papers about the Kondo effect, which give a detailed discussion [27], [19], [28]. Here, only
a phenomenological description is provided to assist understanding of the measurements

in chapter 6 is given. The spin-flip co-tunneling process is illustrated in figure 2.6.
 A stability diagram for an odd number of electrons on a QD is shown in figure 2.7 a).
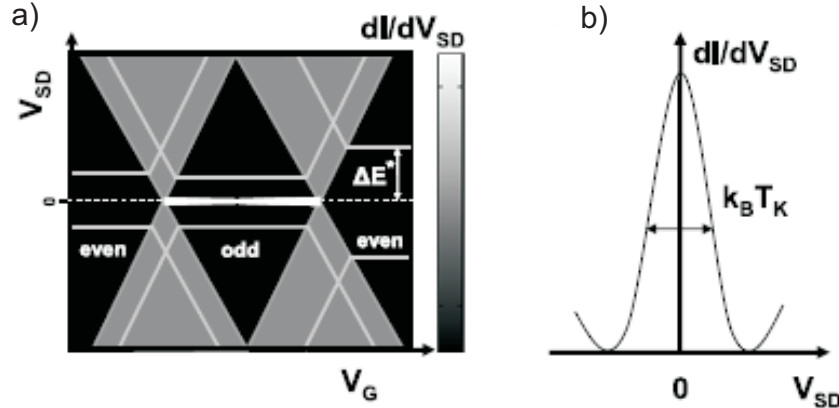

Figure 2.7: *Schematic representation of the Kondo effect. a) Stability diagram: for an odd number of electrons in the dot, the Kondo effect occurs in a zero-bias resonance (white line). b) For $T \ll T_K$ is the full width at half maximum of the Kondo resonance $\approx k_B T_K$. (The figure is adapted from Osorio et al., 2008 [17].)*

There is a zero-bias resonance in the differential conductance visible, connecting both degeneracy points in the Coulomb diamond. Figure 2.7 b) shows a Kondo resonance. The Kondo peak appears only for an odd number of electrons. The full width at half maximum (FWHM) of the Kondo peak is of the order of $k_B T_K$. Where k_B is the Boltzman constant and T_K is the Kondo temperature. For molecular devices the Kondo temperature is typically 20 K - 50 K [17].
The Kondo temperature T_K is a characteristic temperature and defined following the Anderson model as

$$T_K = \frac{1}{2}\sqrt{\Gamma E_C} exp(\frac{-\pi\epsilon}{\Gamma}) \tag{2.7}$$

where E_C is the charging energy and $-\epsilon$ is the difference between the localized state and the Fermi level of the electrodes [25]. The Kondo temperature corresponds to the coupling energy of an antiferromagnetic-exchange coupling, between the electron spin on a QD and the neighboring electrodes, caused by the Coulomb repulsion on the dot.

The application of a magnetic field lifts the spin degeneracy, splitting two previously degenerated levels into two states. This splitting, called Zeeman splitting, is given by:

$$E_Z = \Delta E \pm \frac{1}{2}g\mu_e B \tag{2.8}$$

with g is the electron g-factor and μ_e is the Bohr magnetron. Figure 2.8 shows the symmetric splitting in bias of the Kondo resonance caused by a magnetic field. The right side of the figure shows the Zeeman splitting of the differential conductance in dependence on the magnetic field and the bias voltage.
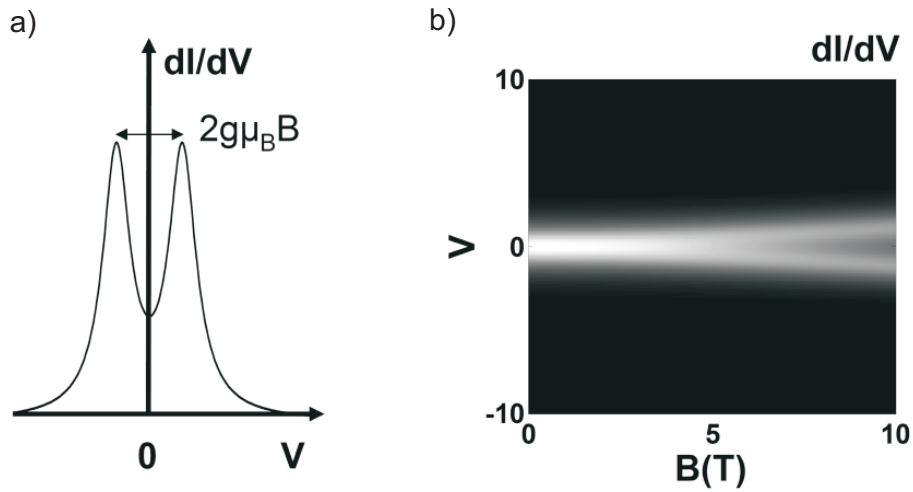

Figure 2.8: *a) Kondo resonance in presence of a magnetic field: A Zeeman splitting symmetric in bias of the peak is visible. b) Calculated gray scale plot of the differential conductance dI/dV versus V_{bias} and B. (The figure is adapted from [17].)*

2.4 Molecules

2.4.1 C_{60} molecules

C_{60} buckyballs are one of the most studied molecule in single-molecule transport measurements. Some of the most interesting results are summarised in this section and should help for the discussion of the measurement results in chapter 6.

First the energy spectrum of a free C_{60} molecule is considered. The energy levels for a neutral molecule and for a molecule with one additional electron are calculated by the Density Functional Theory (DFT) [29], [30]. These calculations are done for a free molecule. The energy levels are shown in figure 2.9. The energy difference ΔE between the HOMO and the LUMO is 1.64 eV for the neutral molecule and 1.5 eV for the charged molecule. Figure 2.9 shows the neutral fullerene five fold degenerated ground state. For the charged molecule, these levels are not longer degenerated. Figure 2.9 illustrates also that the differences between the energy levels can vary between neutral and charged molecule.

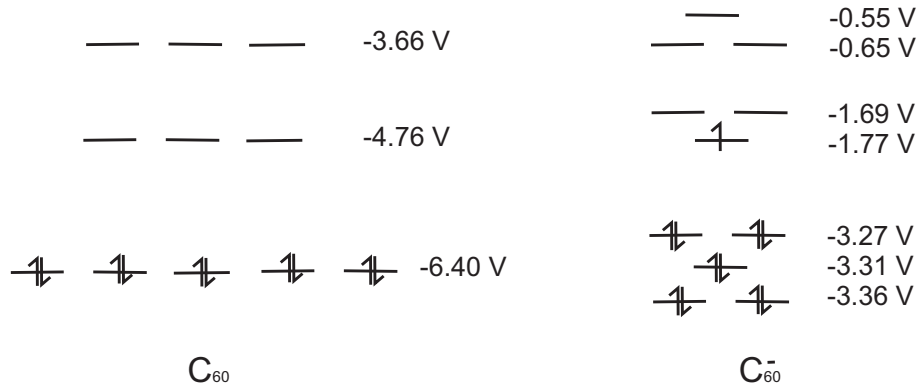Considering now a quantum dot, the charging energy E_C is capacitively coupled to its

Figure 2.9: *Calculated energy pattern for C_{60} and C_{60}^-, adapted from Green [29].*

environment. It can be estimated with the values of the electron affinity and the ionisation energy, which are

$$\mu_0 = U(C_{60}) - U(C_{60}^{1+}) \approx -7.8 eV \quad \mu_1 = U(C_{60}^{1-}) - U(C_{60}) \approx -2.8 eV \qquad (2.9)$$

The chemical potentials μ_0 and μ_1 are calculated using the DFT method [29], [30]. For the addition energy follows μ_1 - μ_0 = 5 eV. The charging energy can be estimated to be in the range $\Delta E = 1.6$ eV to $E_C = 3.4$ eV. The charging energy can also be calculated with formula 2.3, considering that the capacitance of the fullerene can be approximated with that of a sphere $4\pi\epsilon_0 R$ with R = 0.4 nm (radius of a C_{60} buckyball). This calculation gives: $E_C = 3.6$ eV. Both calculation methods give approximately the same result for a free buckyball molecule.

Now, considering a molecule between two electrodes the charging energy is different. A very easy approximation can be done for two spheres shells: an inner shell represents the C_{60} molecule with a radius $r_1 = 0.4$ nm and outer shell should model the electrodes in a distance of 1.0 nm, with $r_1 = 1.4$ nm. The capacitance can than be calculated as $4\pi\epsilon_0/(1/r_1 - 1/r_2)$ and the charging energy is calculated to be $E_C \approx 2.6$ eV. This energy follows from very simple approximations [25]. DFT calculations gave even lower charging energies [31], [32]. It is very difficult to make accurate calculations for a molecule between electrodes because details of the coupling of the molecule to the electrodes has to be taken into account.

Measurements on C_{60} molecules have been performed by various research groups. One of the most studied topics is the Kondo effect. Here the main work is done by Yu and Roch [33], [28], [34]. Figure 2.10 shows the magnetic dependence of zero bias anomalies for three different samples with C_{60} molecules measured by Roch [28]. The Landé-factor g
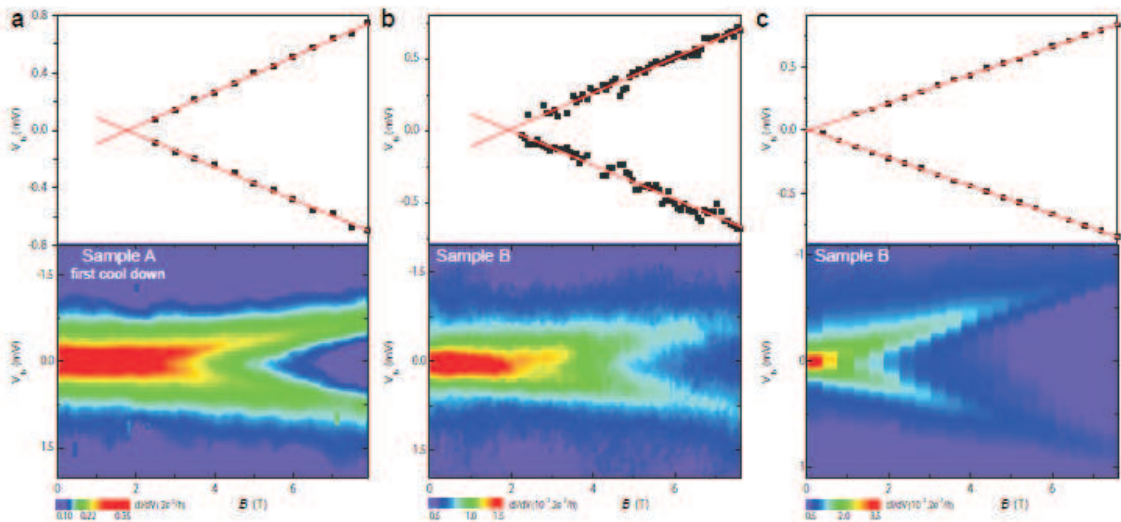

Figure 2.10: *Zeeman splitting for three different C_{60} single-molecule transistors measuerd by Roch [28].*

for the molecules presented in figure 2.10, is 1.98 [28]. This value is similar to the g-value measured in graphene quantum dots: g = 2 [35].

2.4.2 One-dimensional graphene-like molecules

This work also investigates one-dimensional polyphenylene molecules. The molecules are provided by Prof. Dr. Muellen from the Max-Planck Institute of Polymer Research in Mainz. Figure 2.11 shows the molecules. They come in four different chain length: 3.1 nm, 5.2 nm, 7.3 nm and 9.4 nm. On the ends of the chains thiol groups are synthesised.
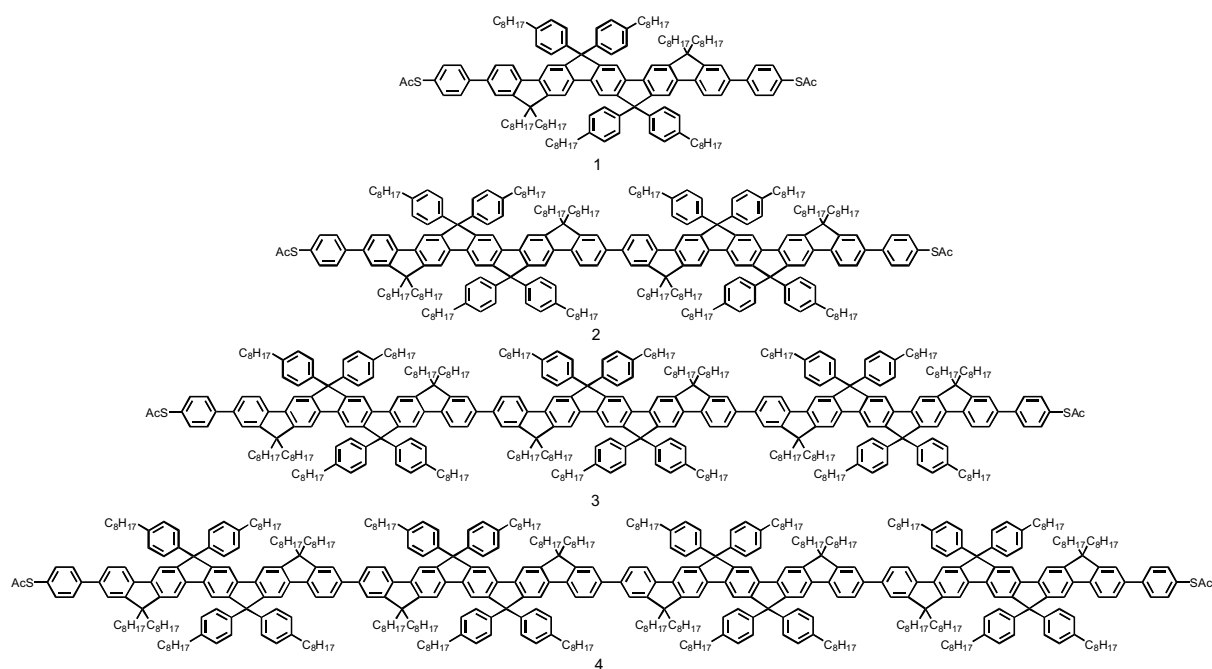
Figure 2.11: *Chemical structure of poly(ladder-type)pentaphenylenes with different chain length, with courtesy of Prof. Dr. Klaus Muellen, MPI Mainz.*

These thiol groups should enhance the binding to the gold electrodes. The poly(ladder-type pentaphenylenes) have linear monomers and so are rigidly linear [5]. The molecules are π-conjugated and are attractive for use in devices like light-emitting diodes (LEDs). The molecules can self-assemble into well defined nanostructures, if they are applied out of a solution. Furthermore, they offer the possibility of adding atoms like fluor or boron by chemical methods to change the properties of the molecules.

Chapter 3

Basic principles

An essential part of the work in this thesis was the development of the lithography processes to get a maximum yield of working single-molecular transistors. A single-molecular transistor is a three-terminal device. It is fabricated by two steps of photolithography (UVL) and one or two steps of electron-beam lithography (EBL). Each of these steps has special requirements on the lithography parameters and the resists. This chapter will give an overview of the basic lithography methods, the properties of different resists and their applications. A technology to fabricate nanometer-scaled structures to contact single molecules directly is described. The details of the single-molecular transistor fabrication is described in the next chapter.

3.1   Lithography

The fabrication of micro- and nanostructures requires lateral structuring of a substrate. Therefore the desired structure has to be imaged as a pattern onto the substrate. This process technology is called lithography. Depending on the desired structure size, the resolution of the applied technology is the limiting factor: for optical lithography, the resolution is basically dictated through the wave length of the used light source. With ultraviolet (UV) light sources, resolution down to 400 nm is possible using the mask aligner[1] in our working group. For the photolithography a resist film is exposed by UV light through a mask with a given pattern. The advantage of this method is that big regions of the substrate can be patterned with only one process step. For the desired nanoconstrictions for the molecular contacts a resolution of 400 nm is not sufficient. Using electron-beam lithography it is possible to obtain lateral structures of a few nanometer size. In case of an arbitrary pattern, it can be designed using a CAD-program and scanned with a properly focused electron beam over the substrate. The disadvantage of this method is the long exposure time because of the sequential scanning of the pattern. The general principle of lithography is described in the following enumeration and schematically shown in figure 3.1.
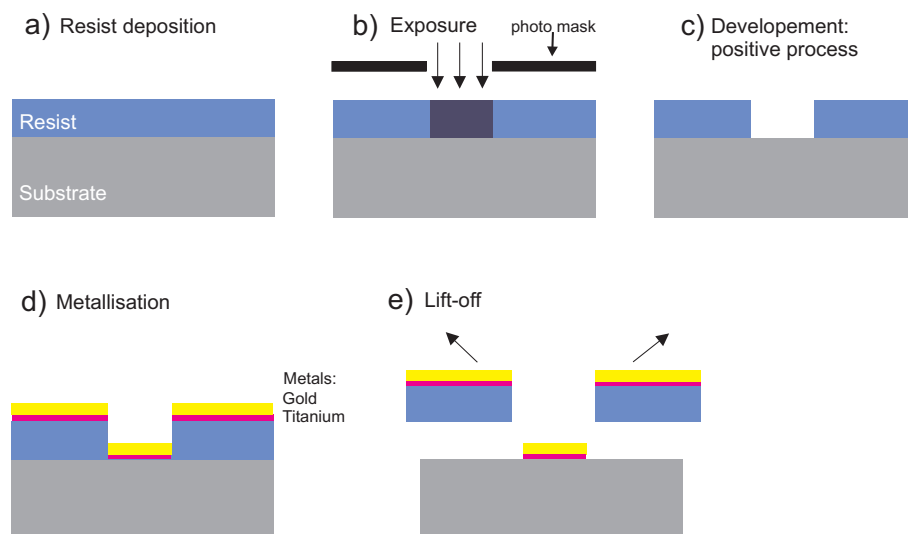

Figure 3.1: *Principle of lithography: a) resist deposition, b) exposure by UV light or an electron beam, c) development: here positive process, d) metallisation of titanium as a sticking layer and gold as a contact metal, e) lift-off process.*

1. Spin-coating of a photon- or electron sensitive resist onto the surface of a wafer. Directly afterwards the sample is baked for a defined time to vaporize the solvent out of the resist and to flow the resist.

---

[1]Karl Suss MJB 3

2. Exposure of the pattern by UV light through a mask or with a focussed electron-beam: the resist changes its properties in the exposed area.

3. Development: in a positive (negative) process the illuminated area of the resist becomes solvable (insolvable) through the application of a specific developer. The resist is removed by the developer.

4. Metallisation/Etching: in a metallisation process, a thin metal layer is deposited on the sample. Possible methods for the metallisation are electron-beam evaporation, thermal evaporation, magnetron sputtering or e.g. atomic layer deposition. In figure 3.1 titanium as a sticking layer (5 nm thick) and then gold as a contact layer (100 nm thick) are deposited by electron-beam evaporation. For the following lift-off process, the bilayer metal system has to be thinner than the thickness of the resist on the sample. For etching processes, RIE (reactive ion etching), CAIBE (chemically assisted ion beam etching) or wet chemical etching are possible technologies.

5. Lift-off: a solvent (usually acetone) to remove the resist with the metal on top of it, is applied to the sample. Only the metal on the opened area remains on the substrate. For final cleaning an additional plasma etching step is applied which removes all organic residuals on the sample surface.

3.2 Resists

The most common, positive photoresists are a combination of Novolac resin and diazon-
aphthoquinone. They are dissolved in solvents like propylene glycol methyl ether acetate.
The exposure to light yields a photochemical reaction in the resist. The exposed area
of the resists becomes dissolvable for polar solvents (developers). All resists used during
this thesis are bought from Allresist GmbH. Only photoresists on Novolac base are used
for positive lift-off processes. For the EBL the resists used are PMMAs (Polymethyl-
methacrylate). They exist with different molecular weights from 50 k to 2.2 M. Smaller
molecular weight implies that the chain length of the polymer is shorter and this yields a
higher sensitivity. The PMMA 50 k (AP-R 639.04) has for example a 20 percent higher
sensitivity than the 950 k (AP-R 679.03) [36]. For a higher difference in sensitivity copoly-
mers PMMA/MA (AP-R 617) can be used. They have a 3-4 times higher sensitivity and
a better contrast than the PMMA resists [37]. This effect can be used for the application
of bilayer resist systems. The possibilities for the use of double-layer resist systems are
described in detail in section 3.2.3.

3.2.1 Determination of the resist thickness

The thickness of the resist is important to know for a working lift-off process. Furthermore
these thicknesses are required for the application of different resists in bilayer systems.
With a profiler[2] it is possible to measure the thickness of a resist layer. The sample is
placed on a high-precision stage which moves beneath the stylus with a user defined scan
length, stylus force and speed. Surface variations move the stylus vertically and can be
transfered to height differences of the sample. The resists for EBL are spun on several
samples with different rotation speed from 3000 to 7000 rpm for 40 s to vary the layer
thickness. They were baked on a hotplate for one hour at $200\,^\circ$C or at $180\,^\circ$C. In figure 3.2
the dependence of the resist thickness on the rotation speed of the spin-coater is shown.
The thicknesses are measured over 30 μm wide scratches on five points distributed over a
1 cm^2 big wafer piece. In the processes described in section 3.3.2 and chapter 4, the resist
AP-R 679.03 is used as top layer in the double-layer systems and the other three, more
sensitive resists (AR-P 639.04, AR-P 617.06 and AR-P 617.08) are used as the bottom
layer.

3.2.2 Profiles after the development

A suitable resist profile after the developing is important for a working lift-off process. The
resist profile depends on a appropriate dose (number of photons/electrons per area) during
the exposure and the development process (developing time and developer concentration).
In general, three different profiles can exist after the development. They are shown in

---

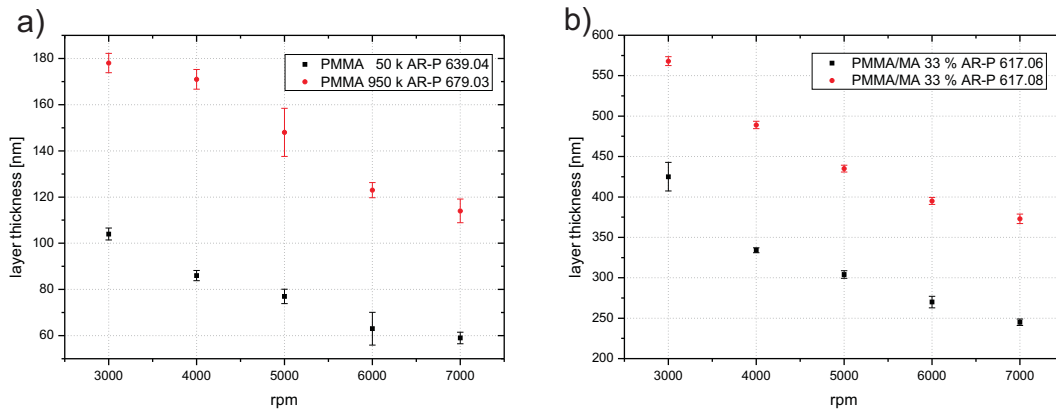[2]Dektak 6M Stylus Profiler from Veeco

Figure 3.2: *Thickness of the resists as a function of the spin-coaters rotation speed. All resists are spun on top of a wafer for 40 s and baked on a hotplate for 1 h. The resist AP-R 679.03 is baked at 180 °C, the AP-R 639.04 and the AP-R 617 at 200 °C.*

figure 3.3. The desired profile for the lift-off is the undercut (a), which guarantees a reliable lift-off process. In this case the shape is determined by the dose, and for EBL also by the reflected and back-scattered electrons. A perpendicular metallisation prevents a connection of the metal structure in the opened resist window due to sidewalls to the metal of the surface. The solvent can easily penetrate and dissolve the resist and lift-off the metal film. Resist profile (a) has to be used for high resolution structures. This profile is created by high doses during the exposure and by the use of a fast working developer. The image in the resist is formed by photoscission of the polymer chains and hence the lowering of the molecular weight. The dissolution rate R for the exposed region should be much higher than the unexposed dissolution rate R_0. In order to create the undercut profile it is important that the dissolution rate ratio $\frac{R}{R_0}$ is higher than 10 [38]. Profile (b) can work concerning the lift-off in case of a perpendicular metal evaporation only if the thickness is much thinner than the resist layer. If the metallisation is not exactly perpendicular, the flanks of the resist can be covered by metal and after the lift-off small, thin sidewalls remain on the edges of the structure (see schematic drawing 3.4). These sidewalls can cause problems in the following process steps. For example, an overlapping structure created in the next lithography step, can be broken by the sidewalls and the electrical connection of the device is interrupted. In figure 3.4 the sidewalls of the gate electrode (aluminum) destroy the connection between the nanoconstriction on top of the gate and the connecting leads to the bonding pads. This problem often occurred in the process development of the gate electrode during this thesis (see chapter 4.1.2). In the case of the overcut profile (c) in figure 3.3 the lift-off often will not work because there is no possibility for the solvent to attack the resist in the flanks of the structures to lift-off the resist and the metal. The flanks are completely covered with the metal film (f). Even if the lift-off will work, often sidewalls remain causing device failure. Profile c)
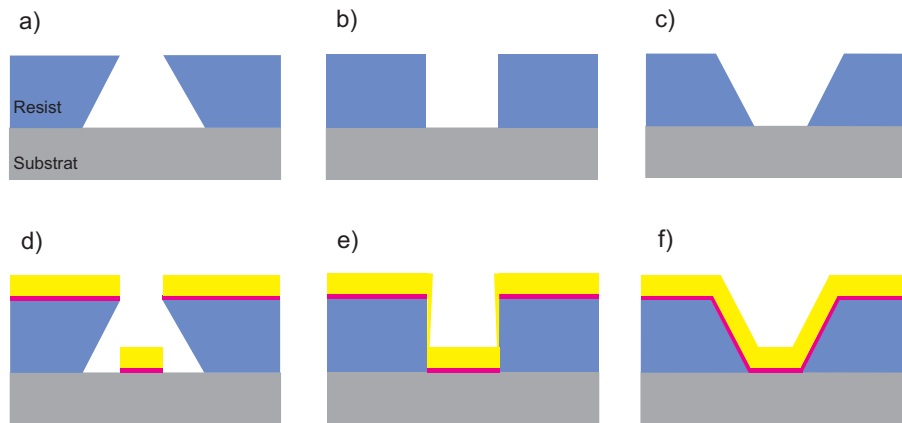
Figure 3.3: *Possible resist profiles after development: a) undercut profile, b) perpendicular profile, c) overcut profile, d) - f) after metal evaporation, lift-off will work reliable only in case of the undercut profile.*

depends on the process parameters of the development (e.g. too long development time by photoresists). In this case the dissolution rate ratio $\frac{R}{R_0}$ of the polymer is lower than 10 (see above) [38].
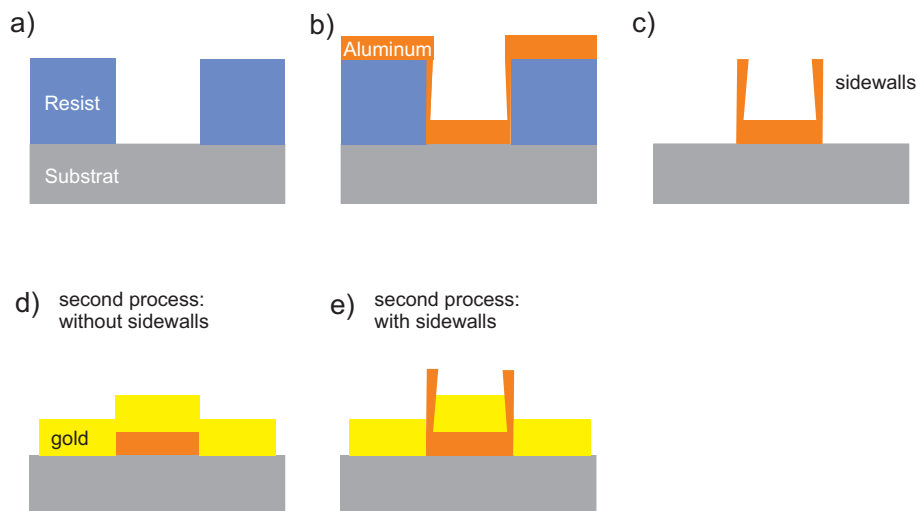

Figure 3.4: *Schematic drawing concerning sidewalls. This picture shows not the real ratios and size, it should only help to explain the problems due to sidewalls. a) perpendicular resist profile after development, b) after metal evaporation, c) after lift-off sidewalls remain on the edges of the aluminum structure, d) A second process step on top of the first layer without sidewalls in the first layer. The second gold layer is completely connected and the device is working. e) The second layer is interrupted by the sidewalls of the first one and the device can not work.*
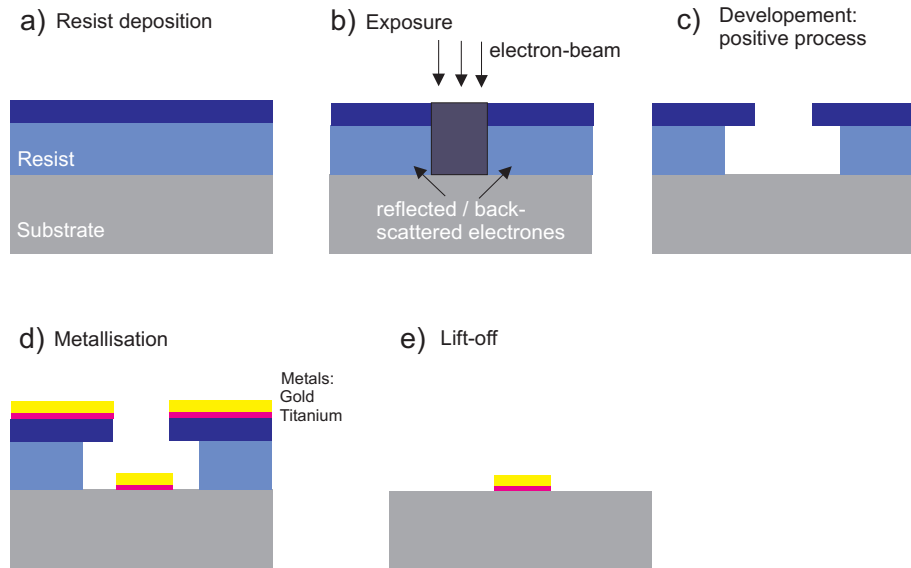
3.2.3 Double-layer resist systems

Figure 3.5: *Double-layer resist system: a) Two resists with different sensitivities are subsequently spin coated on top of a substrate. The bottom layer is more sensitive than the top layer. b) Exposure of the resist. The top layer gives the exact image projection, the bottom layer is more sensitive and additionally exposed by electrons which are backscattered by the substrate. c) Development. An undercut profile is created. d) Metallisation: There is no connection between the structure and the resist. e) Metal structure after lift-off.*

An alternative method to create an undercut profile is the implementation of a double-layer resist system. This is often done for EBL to assure a working lift-off process. Furthermore there are special bilayer resists for UVL. In general two layers of PMMA with different molecular weight and hence different sensitivities are spin coated and baked successively. The bottom layer, also called the lift-off layer, is more sensitive and creates the desired undercut. The top layer is called the image layer because of its properties to define the structure size (see fig. 3.5). In case of a big difference in sensitivities of both layers, free standing resist bridges can be created. This method is used for shadow evaporation technique which will be explained later in chapter 4.2.2 of this thesis.

3.2.4 Resists for cold evaporation

Photoresists are generally handled at room temperature and baked between 80 °C and 110 °C. Some resists are thermally stable up to 150 °C [39]. Even though most of the process parameters are described in data sheets, there is no information about the minimum temperature which the resists can support without loosing their properties. In the second step of photolithography it is important to evaporate the aluminum at liquid nitrogen temperature (77 K). The reasons are explained in section 4.1.2 in detail. To

find a suitable resist, all photoresists available were tested at 77 K. In total, six different single-layer and four double-layer resist systems from Allresist GmbH were investigated. The parameters for the resist spin coating and baking process are shown in table A.1. The samples are mounted on a special sample holder with a liquid nitrogen reservoir on the backside. After cooling down to 77 K, tempering there for 10 minutes and warming up, the resists are inspected with an optical microscope. Most of the resists are damaged by the cooling process like shown in figure 3.6. This massive damage makes a reliable lift-off process impossible. Three photoresists were not affected by the low temperature: AR-U 4060, SX-AR-N 4800/16 and AR-N 4340. More detailed information about this tests are described in the diploma thesis of Simon Moser [40].
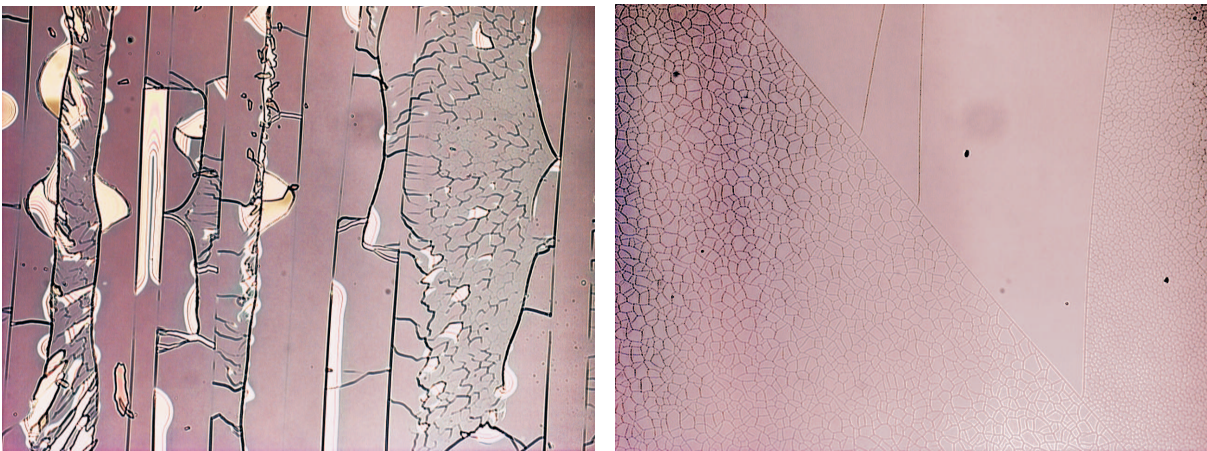

Figure 3.6: *Optical microscope images of resists taken after thermal shock testing. Left: the resist AR-P 3540 shows different cracks: long fissures and bubbles; right: the bilayer resist AR-P 5640/AR-P 3540 shows three different size of cracks in the surface.*

3.3   High resolution electron-beam lithography

For the EBL a scanning electron microscope (SEM) type LEO 1525[3] with an Elphy pattern generator[4] for EBL is used. The electron source of the SEM is a thermal Schottky-field-emission cathode (W/ZrO). The accelerator voltage of the electron beam can be controlled between 0.1 kV and 30 kV. For high resolution EBL, the maximum acceleration voltage of 30 kV is used. In theory, the resolution is limited by the wavelength of the electrons. The wavelength of an electron is defined through the de-Broglie relation. For an accelerator voltage of 30 kV the electron wave length is $7 * 10^{-12}$ m. The effective resolution is restricted by different effects. The electron beam spot has a finite dimension. The spot size depends on the focus of the electromagnetic lens system. Further, the electron-beam is shaped by forward scattering in the resist and backscattering of the electrons from the substrate. The broadening of the image due to the interaction of the electron-beam with resist and substrate is called the proximity effect in electron-beam lithography. The resolution depends also on the properties of the used resists: in particular from the thickness and the molecular weight.

3.3.1   Proximity effects

The impact of the electron-beam on a material causes interactions between the electrons and the atoms. When the electron-beam is entering the resist, it will be enlarged by scattering off the molecules of the resist. Then, the beam will be scattered further in the substrate through electron collisions at the lattice atoms. One part of these electrons will be back scattered into the resist and causes backward exposure. These both effects, forward and backscattering of the electron-beam, are limiting the resolution of the EBL in addition to the resist properties.
The Bethe-Bloch formula states that fast electrons (with higher energies) transfer less energy to the system and they are less deflected. Hence, the scattering behavior depends on the acceleration voltage of the electron beam. This can be calculated by Monte Carlo simulations and is shown in figure 3.7. A simulation of 100 electron trajectories for acceleration voltages of 10 kV and 20 kV is plotted. Low acceleration voltages enlarge the electron-beam by forward scattering, thereby the electrons of the beam are slowing down. The number of scattering processes in the substrate is low. For reasonable resist thickness, this causes an undercut in the resist profile. Therefore it is also a possibility to create the undercut for the lift-off process (see fig. 3.7 a)). The forward scattering decreases for higher acceleration voltages and the electron-beam penetrates the resist with a nearly straight trajectory. In this case, the backscattering of high energy electrons from the substrate dominates and the area is exposed with a higher dose (fig. 3.7 b)). The above described effects are called proximity effect.

---

[3]Carl Zeiss LEO 1525
[4]Raith GmbH

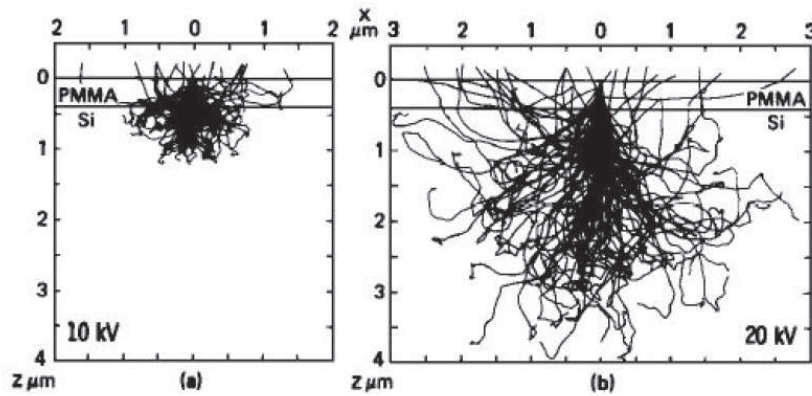The proximity effect can be divided in two effects: the *intra-* and the *inter-proximity*

Figure 3.7: *Monte Carlo simulation of 100 primary electrons trajectories in a layer of PMMA on a silicon wafer. a) The beam energy is 10 keV, scattering is low and confined to the surface area. b) For higher beam energies like 20 keV the scattering processes increase massively [41]*

effect. A schematic of these effects are shown in figure 3.8. The inter-proximity effect plays a significant role if structures are too close to each other. This means that their distance is smaller than the scattering length of the electrons. The electrons from the exposure of one structure can scatter in such a way that the area between the structures and the neighboring structure is affected by backscattered electrons. This effect has to be considered if the distance between two structures is less than a few μm. A smaller dose has to be used for the exposure at neighboring areas.

For the intra-proximity effect the dose in the center of a pattern is larger than at the edges and corners. This effect is geometric because there are less electrons contributing to the dose at the edges of a pattern.
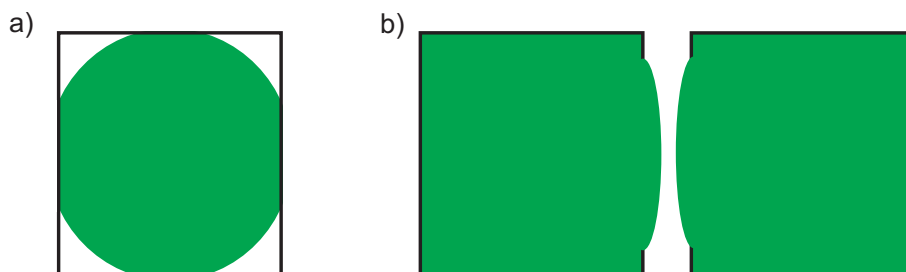

Figure 3.8: *Schematic drawing of a) the intra-proximity effect and b) the inter-proximity effect for a square.*

3.3.2   Single-pixel-lines

In this section, some of the high resolution EBL results are presented. The task is to structure a line with a gap in the middle, which is small enough to trap a single molecule (see schematic 3.9). For the available molecules a gap size of less than 10 nm is needed. It was shown in [42] that it is possible to write 6 nm wide Au/Pd lines with the available EBL system. These structures were not continuous and only three nanometer thick. For pure Au the lines were 8 nm thick, the width depends on the grains size of the evaporated Au. In [42] it is reported that Au lines with a width of 15 nm were continuous. These lines were defined as single-pixel-lines (SPL) in the Elphy system. This means that a line with a thickness of 0 nm (one pixel) is written by the pattern generator. So, the width of exposure is the broadening of the electron-beam. Further, the line width depends on the molecule size of the used resists. The used bilayer resist system for this structures was PMMA 50 k as lift-off layer and PMMA 200 k as image layer. Lehmann showed the limits of the EBL system, but his structures were not suitable for measurements.

In this work it was tried to produce a continuous line with only a single, a few nanometer
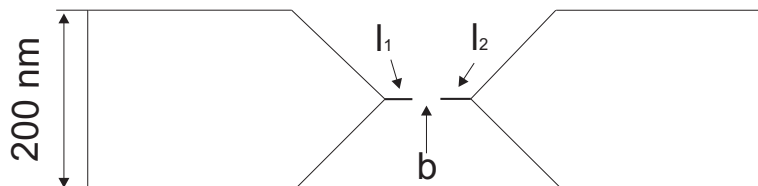

Figure 3.9: *Schematic image of the exposed structures. l_1 and l_2 are the lengths of the single-pixel-lines. b is the defined size of the gap.*

sized gap in its center as shown in the schematic drawing of figure 3.9. The structures should be usable for single-molecule measurements. For SPLs, the EBL software sequentially writes points with a distance equal to the step size to each other. During the exposure the finite diameter of the electron-beam and the proximity effect broaden the sequence of points to a thin, continuous line. Two lines with a gap in the middle like in figure 3.9 are exposed, for high beam doses a thin line will be formed. The minimum step size for the exposure is 1.25 nm (by 16-bit AD-converter in a $81,92 \times 81,92 \ \mu m^2$ write-field), this means that the gap size has to be a multiple of this value. Due to the inter-proximity effect, it is difficult to process lines with small gap sizes. The line dose is determined in several dose tests. It is not possible to resolve less than 10 nm with the used resist system. Due to the definition of the gap between the two lines and the granularity of the evaporated gold, a discontinuity can be built. Too high line dose yields to a continuous line. There, the gap can be formed by electromigration. Too low dose leads to gaps bigger than 10 nm.

A bilayer resist system consisting of AP-R 679.03 (PMMA 950 k) as top layer and AP-R 639.04 (PMMA 50 k) as bottom layer is used for the EBL of the single-pixel-lines. The top layer has a high contrast, but a low sensitivity. This is different from the resist system

in [42], [43]. The exact process data are noted in Appendix B.1. The exposure is realised
at 30 keV. The beam focusing is done by a 3-point focus correction on the working dis-
tance of the Elphy system. The software is correcting differences in the working distance
on the sample surface in the focus mode. The beam current was 0.136 nA, an aperture
of 20 μm is used for these experiments. The resolution of the system is set to 2 pixel
which corresponds to a step size of 2.5 nm. The area dose for the 200 nm electrodes is
set to 1200 $\frac{\mu C}{cm^2}$. The line dose of the single-pixel-lines is slightly varied between different
structures. Table 3.1 shows the exposure parameters and results for different samples.

The gap sizes b which are defined by the pattern generator are 5 and 10 nm, respec-

set gap size b [nm]	length l_1 [nm]	length l_2 [nm]	line dose $\left[\frac{\mu C}{cm}\right]$	real gap size g [nm]	number of structures
5	50	45	1350 - 1485	>30	39
5	50	45	1404 - 1553	< 3	21
5	50	45	1472 - 1755	line	12
10	45	45	1350 - 1485	>30	42
10	45	45	1431 - 1553	< 3	12
10	45	45	1431 - 1755	line	18

Table 3.1: *Overview of the parameters and the results of the exposure of single-pixel-lines.
The real gap size is determined by SEM measurements. The total number of structures for
each set gap size b is 72.*

tively. The dose was varied from 1350 to 1755 $\frac{\mu C}{cm}$. After the exposure 8 nm of gold are
evaporated at low rates from a distance of one meter at the upper evaporation chamber
of the electron beam evaporation machine. The structures are inspected with the SEM
and the gap sizes g are measured.

It is not possible to resolve gaps smaller than 3 nm with the SEM. For these samples the
resistance is determined in 2-point-configuration by current and voltage measurements.
They showed all resistances higher than 10 GΩ. This implies that there is a very small
gap. In table 3.1, the line dose ranges for gaps bigger than 30 nm, small gaps ($\leq$ 3 nm)
and lines are overlapping. This fact is due to the position of the structures on the sam-
ple and the focusing of the electron beam. Even with the 3-point-alignment it was not
possible to assure a precise focusing over an area of 10 mm^2. Also, the proximity effect
from the bigger structures influences the exposure of the SPLs. The best results were
achieved in dose ranges from 1404 - 1553 $\frac{\mu C}{cm}$ and 1431 - 1553 $\frac{\mu C}{cm}$. The yield of working
structures with a given gap size b of 5 nm is 29 % and for 10 nm gap size is 17 %. For
later experiments a dose range from 1485 - 1553 $\frac{\mu C}{cm}$ is used. Here the yield of working
nanogaps is between 50 and 60 %. Figure 3.10 illustrates a nanoconstriction with a gap
smaller than 3 nm in its center. The gap is in the region of the red circle. For structures
with small continuous lines a gap was produced by electromigration (see chapter 5). A
4 nm gap built with this technology is shown in figure 3.11. All process parameters are

given in tabular form in Appendix B.

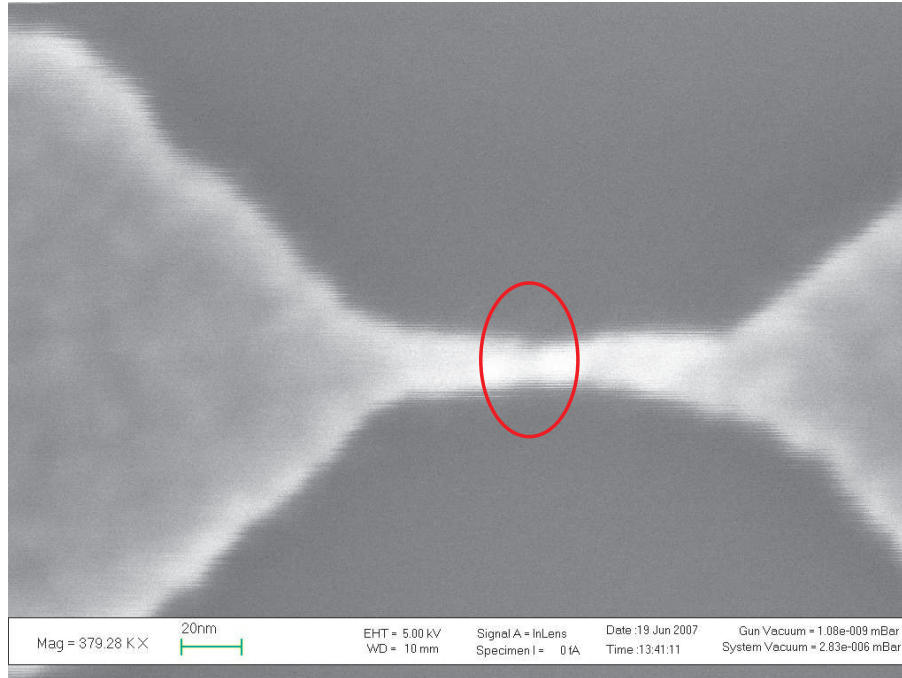The challenge for this high resolution EBL is the precise beam focusing. It has to be

Figure 3.10: *SEM image of a structure with a single-pixel-line in the middle. The single-pixel-line has a gap which is not resolvable in its center (red circle) with the SEM. The gap is smaller than 3 nm. The I-V-measurement shows a resistance bigger than 10 GΩ.*

done at high magnifications and next to the structures. If the structures are only a few micrometer separated from each other the 3-point-focus-alignment of the systems works well, but if the structures cover an area of a square centimeter like for our single molecule transistors the area is too big for a precise focusing. This technology is only suitable for single samples, not for our mask with 100 structures exposed in one process step.
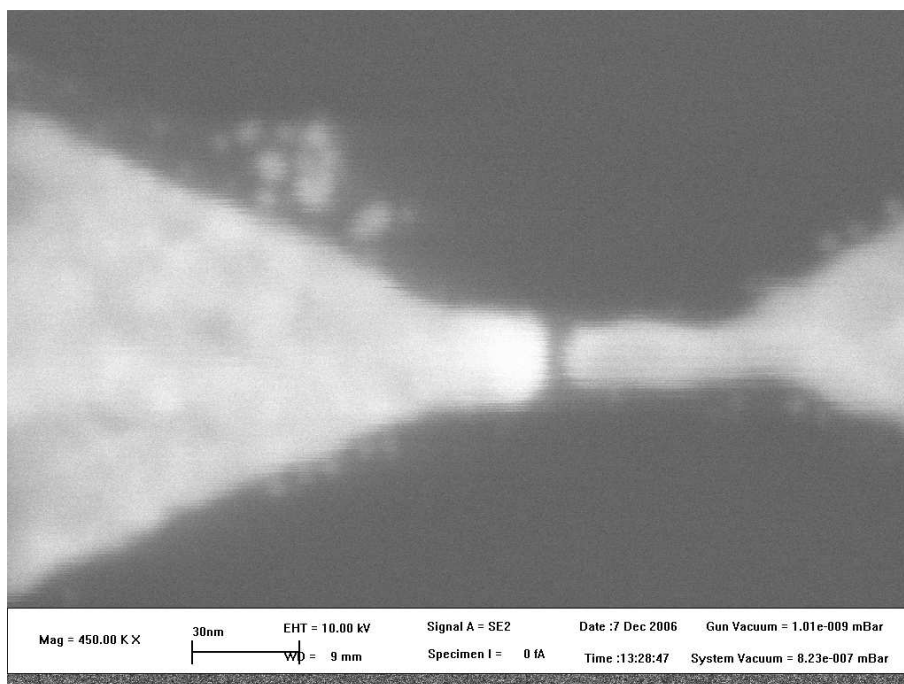
Figure 3.11: *SEM image of a structure with a single-pixel-line in the middle. The single-pixel-line has a width of 10 nm and a gap of 4 nm in its center. This gap was created by electromigration (see chapter 5) in a continuous, 15 nm wide SPL after lithography.*

Chapter 4

Fabrication of three terminal devices

A single-molecule transistor (SMT) is a three-terminal device. In the ideal situation the molecule is trapped between two electrodes (bias and ground electrode) and the energy levels of the molecule are controlled by a back gate. The SMT is processed by two steps of optical lithography and one or two steps of electron-beam lithography (EBL). A schematic drawing of a SMT is shown in figure 4.1.

Different designs for the SMTs are proposed by the groups of Herre van der Zant and
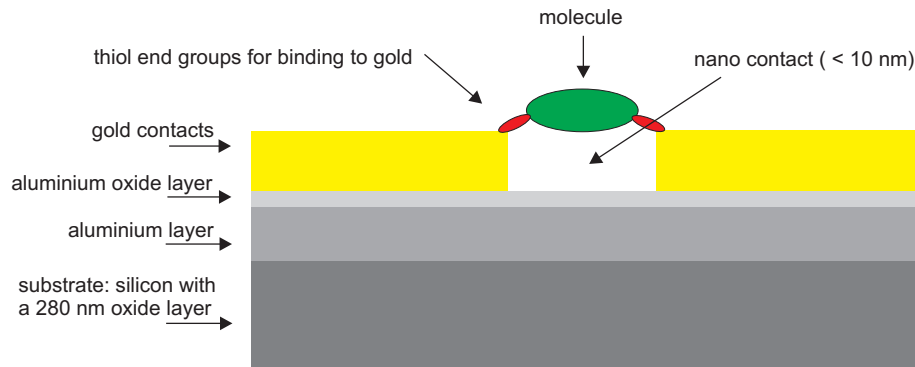

Figure 4.1: *Schematic drawing of a single-molecule transistor: The substrate is silicon with a silicon oxide layer on top. On top of the substrate, the aluminum/aluminum oxide gate is structured. The nanogap is processed by EBL and electromigration. A molecule can be bound between the gap with or without thiol end groups.*

Franck Balestro [44], [4], [45], [17], [46]. In this thesis, both approaches are applied. Because of the design of the sample holders in the cryostats, 18 contacts can be used. Therefore, there are 14 nanocontacts on one structure, one common bias/ground contact and one common gate contact. The ground and the gate contact are double bonded. Figure 4.2 shows a structure after the optical lithographies. The optical mask gives the possibility to create an array of 100 structures, this means 1400 nanoconstrictions all together. The inner part with the nanoconstrictions is shown later in section 4.2.

In this chapter, the development of the nanolithography and the complete fabrication pro-

43

cess for the three-terminal devices is described. First, the optical lithography is discussed. A crucial point is the development of the cold evaporation process for the aluminum oxide gate. This section is followed by a discussion of the electron-beam lithography for the nanoconstrictions. Here, focus lies on two technologies: shadow evaporation and structuring of small lines. The nanogap in these structures is created by electromigration (see chapter 5). It is also possible to structure gaps directly by shadow evaporation. The gap size of this structures is about 10 nm. This process is described in this chapter. At last, the preparation and deposition of the molecules is explained.

4.1   Photolithography

4.1.1   Gold contact pads

The contact pads, the leads to the inner part of the structures, the common ground electrodes and the alignment marks for the following steps are all made by a first step of optical lithography. The process has to be optimized with respect to two aspects: (i) the 2-μm sized alignment marks for the e-beam lithography should have a clearly defined shape, (ii) it is important for the following process steps that the ground electrode has no sidewalls on its edges (see section 3.2.2). The process parameters have to be optimized for each series of samples, because the photoresist characteristics depends on the time of storage. The photoresist concentration can change over time due to evaporation of the solvent in the resist.

The Allresist GmbH photoresist AR-P 5350 is used for this process step [47]. It is a positively working resist for UVL, which generates an undercut profile and is suitable for lift-off processes. The resist is spun for 40 s at 5000 rpm onto the substrate. This gives a layer thickness of about 900 nm. After baking the sample for 5 min at 105 °C on a hotplate, the structures are illuminated in an UV mask aligner in the hard contact mode to obtain good alignment marks. Then, the structures are developed with Allresist GmbH developer AR 300-26, carefully rinsed with water and blown dry. By electron-beam evaporation 5 nm of titanium as a sticking layer and 50 nm of gold are evaporated with a rate of 0.5 nm/s onto the sample. The lift-off process is done in acetone at 50 °C and sonication for some minutes is used to get rid of possible sidewalls on the edges of the structures. The detailed recipes are shown in the Appendix C.2. The structure is shown in figure 4.2 a).

4.1.2   Aluminum oxide gate

In three-terminal devices, the orbital energy levels E_n can be shifted by the potential of the gate electrode V_G. The ratio of the shift in E_n to the applied gate electrode potential eV_G is the coupling parameter β. This gate coupling parameter should be as high as possible to access as many charge states as possible. The most frequently used gate insulator material is thermally grown SiO_2 on top of heavily doped silicon substrates. Another possibility for a gate is an aluminum layer with a native oxide layer structured on top of SiO_2 layers on silicon substrates [4]. The aluminum gates with an oxide thickness of about 3 nm have a gate coupling of around 0.1 and the breakthrough voltage is between 2 and 3 V or even higher. This gives the possibility to shift the potential of the molecular levels by $\pm$ 0.3 eV. In silicon devices with an oxide layer thickness of 250 nm, the gate coupling is about 10^{-3} with a typical breakthrough voltage of 100 V. This gives a potential shift of $\pm$ 0.1 eV [4]. For the reason of higher gate coupling, aluminum is chosen as a gate material.
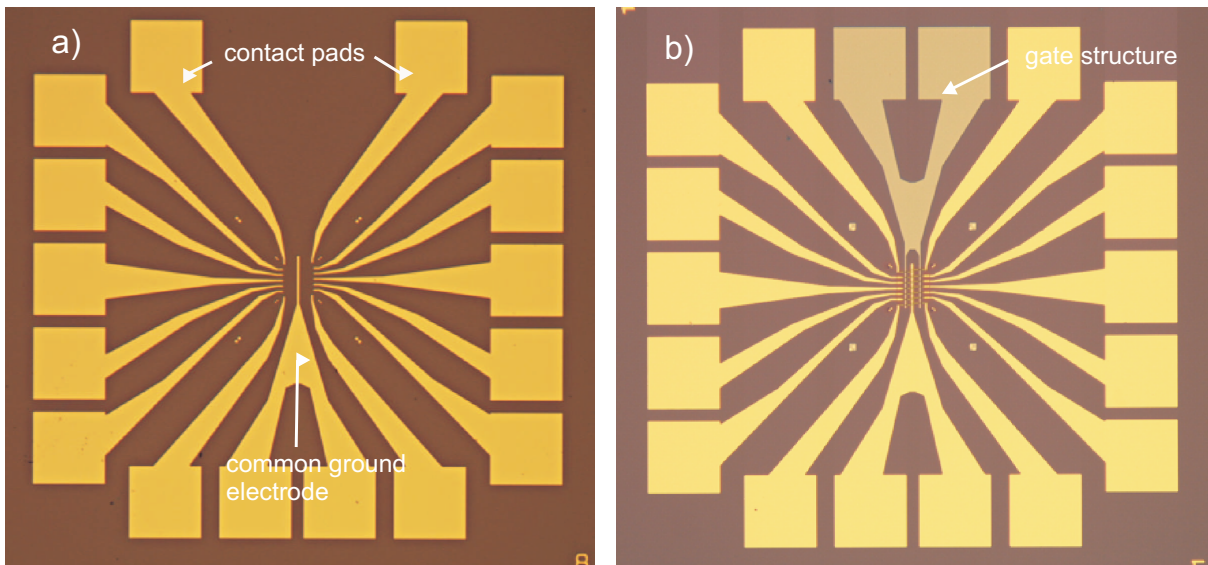
Figure 4.2: *a) Optical micrographs of a structure after the first step of optical lithography. The golden contact pads and their connection leads to the inner part are shown. b) Image after the second step of optical lithography. The aluminum oxide gate is visible in the gap from structure a).*

Aluminum oxide grown at room temperature contains various defects. The bonding is mostly ionic and the coordination numbers are higher than for example in silicon oxide. Therefore Al_2O_3 is a poorer glass former and has a higher concentration of non equilibrium defects because the oxide network is less able to relax, to rebound and to remove defects. This leads to a grainy structure surface. Furthermore, aluminum forms islands on the surface of the substrate during the evaporation and yields a very rough structure [48]. If the surface of the gate oxide is too rough, it is possible that thin nanostructures on top of the gate will be interrupted by grains of the Al_2O_3 layer.

Amorphous aluminum can be grown at liquid nitrogen temperatures. The cold grown aluminum can configure its interface bonding to minimize the number of interface defects. Furthermore the dielectric constant is isotropic so that fluctuations in polarization from differently orientated oxide grains will not scatter carriers. There are no grain boundaries in amorphous phases. Amorphous aluminum oxide can be grown by cold evaporation and subsequent thermal[1] oxidation. This process is often followed by plasma oxidation. Plasma oxidation leads to a thicker and more stable oxide because the ozone or oxygen radicals created in the plasma are much more reactive than pure oxygen and can penetrate deeper into the surface of the aluminum layer [48].

Design and application of the sample holder for cold evaporation

A sample holder for the evaporation of metal at low temperatures is developed. It is

---

[1]at room temperature

designed with a reservoir for liquid nitrogen on its backside to cool the sample . The liquid nitrogen can be filled into the reservoir by a tube and it is possible to blow it out after the evaporation with nitrogen gas or a hot air gun to warm up the sample holder. The sample holder is screwed on top of the evaporation machine and separated by a valve from the high vacuum evaporation chamber. This load lock can be pumped separately and can be flushed with pure oxygen gas to oxidize the sample after the evaporation. The oxygen pressure is controlled by a needle valve. The sample holder is shown in figure 4.3.
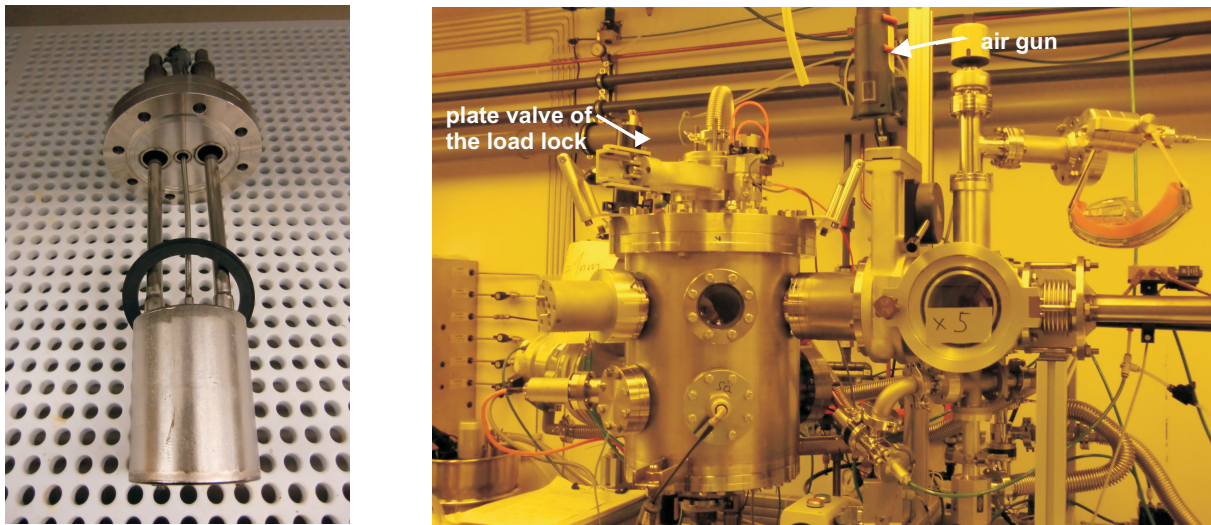

Figure 4.3: *Left: sample holder for the cold evaporation of aluminum. The nitrogen is filled in the reservoir by the steel tube on the left side. The sample is screwed on the bottom of the holder. Right: the evaporation machine with the possibility to separate the sample from the chamber by a valve, to heat and to oxidize the sample in the load lock.*

4.1.2.1 Dependence of the aluminum surface roughness on substrate and evaporation rate

Different evaporation tests are performed to find the best parameters for the growth of the aluminum/aluminum oxide layer with the new sample holder. First, the influence of the substrate and the evaporation rate to the layer roughness of aluminum is tested. It is important for the growth of the Al_2O_3 that the aluminum layer is very smooth. A smooth layer surface indicates a more stable oxide layer and the reliable e-beam lithography on top of the layer (see section 4.2). Pieces of the SiO_2/Si substrate are mounted on the sample holder and evaporated with 25 nm of aluminum using different rates. In the second test, a 3 nm thin layer of titanium is evaporated before the aluminum layer. For the growth of gold on SiO_2 it is important to evaporate firstly titanium as sticking layer on the substrate. Here, the idea is to check if the growth starting with a thin Ti layer makes the Al smoother. The roughness of the samples is measured with an atomic force

microscope (AFM). Scans over an area of 10 μm^2 with a resolution of 128 x 128 pixel were performed and the arithmetic mean deviation and the root mean square deviation (RMSD) of the surface height is calculated with the AFM software. The results are displayed in figure 4.4 a). For rates below 0.2 nm/s the electron gun for the evaporation is running unstable. This fact leads to a very irregular metal deposition and a rough surface structure. For higher rates, the roughness decreases and the difference between the layer with titanium and without is very low. This shows that the titanium sticking layer has very small influence to the surface roughness of the aluminum.
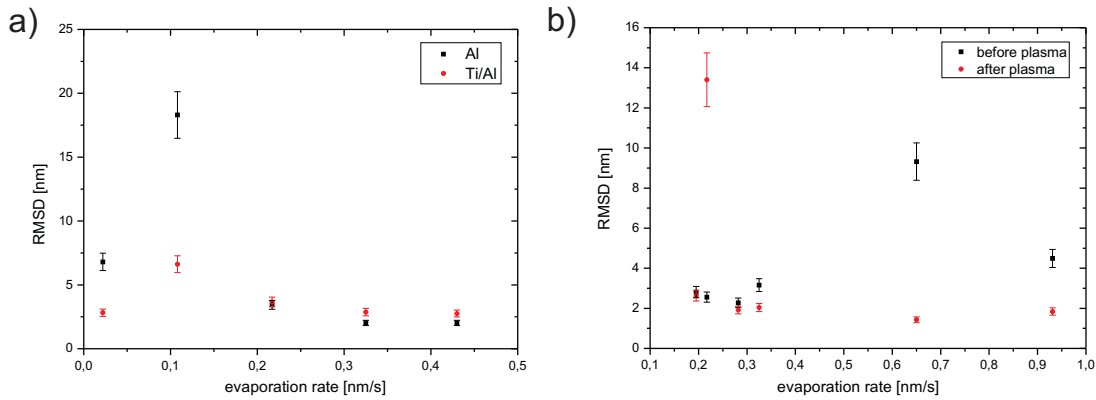

Figure 4.4: *a) Dependence of the surface roughness on the evaporation rate and the substrate. The root mean square deviation (RMSD) of a 10 x 10 μm big area is measured with an AFM. Low evaporation rates of aluminum show high roughness which is a sign for an unstable evaporation. For rates above 0.2 nm/s, the aluminum and the aluminum with a 3 nm titanium layer below show marginal differences. b) Dependence of the surface roughness on the evaporation rate before and after plasma oxidation. With one exception, the surface is smoother after an additional step of plasma oxidation.*

4.1.2.2 Dependence of the aluminum oxide roughness with and without plasma oxidation

Knechten et al. report that plasma oxidation gives thicker and more stable Al_2O_3 layers [48]. To see its influence, the surface of the Al_2O_3 layer is investigated before and after plasma oxidation. The aluminum is grown under liquid nitrogen temperature with different evaporation rates (higher than 0.2 nm/s) and thermally oxidized in the load lock for 30 minutes under pure oxygen with pressure of 100 mbar. Then, the surface is inspected with the AFM as described above. After that, the samples are oxidized in a plasma asher for 8 minutes at 1 mbar oxygen pressure and with a power of 200 W. The results are illustrated in figure 4.4 b). Most of the RMSD values are smaller after the additional plasma oxidation, hence the surface of the oxide is smoother. The difficulty of the comparison of

the measurement before and after plasma oxidation is that the area which is scanned with the AFM is not exactly the same. A second issue is that the sample can be contaminated by the AFM measurement and during the transfer out of the clean room. This can be the reasons of the high RMSD value for a rate of 0.22 nm/s.

4.1.2.3 Dependence of the aluminum oxide roughness on the power of the plasma oxidation

Furthermore, the influence of the plasma power on the aluminum oxide roughness is tested. With the available PICO plasma asher the power is tunable from 0 to 200 W. Two samples are oxidized at 50, 100, 150 and 200 W respectively at 1 mbar pressure for 10 minutes. The roughness is measured with an AFM as described above. The RMSD is shown in figure 4.5 a). For a plasma power of 100 W, the oxide roughness is smaller than 1 nm and similar for both samples. With this result and the conclusions of the experiments described above, the following process is proposed for the Al_2O_3 gate layer:

- evaporation of 25 nm aluminum at liquid nitrogen temperature with rate of 0.43 nm/s at a pressure of 10^{-6} mbar,

- slowly warming up the sample to room temperature,

- filling of the load lock with pure oxygen at a pressure of 100 mbar for 30 minutes

- plasma treatment at 1 mbar and a power of 100 W for 10 minutes.

4.1.2.4 Leakage current through the gate oxide

On 50 structures the gate leakage current is measured in a cold probe station at 15 K. A DC-voltage measurement in 3-point configuration (two needles to measure the voltage drop over the nanoconstriction and one needle to apply the gate voltage), with a large series resistor to determine the current, is performed. The results are shown in figure 4.5 b). Most of the gate structures show resistances of more than 30 GΩ for a gate voltage sweep from -2 to 2 V. The leakage current is below 5 pA. The measurements are performed on a test sample after electromigration (see chapter 5). During electromigration, the sample is exposed to immense thermal stress. This can lift the gold structure off the Al_2O_3 layer and further destroy the nanoconstriction. Also, defects in the oxide layer can lead to leakage currents.

4.1.2.5 Fabrication process for the aluminum oxide gate

For the aluminum evaporation at liquid nitrogen temperature not all resists are suitable. In chapter 3 and in appendix A.1 a list of all tested resists is shown. Some of the resists
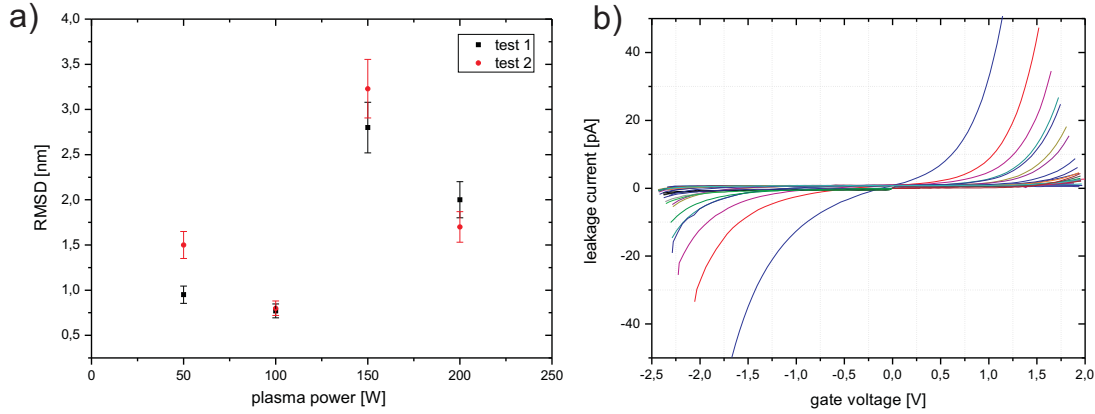
Figure 4.5: *a) Dependence of the surface roughness to the plasma power. All sample are evaporated with a rate of 0.43 nm/s. The test is performed twice to check the reliability of the results. For 100 Watt, the RMSD is smaller than 1 nm. b) Leakage current measurement: The leakage current for 50 gate structures is measured over a gate voltage range from -2 to 2 V. 80 percent of the structures show a leakage current below 5 pA.*

are cracking due to the cooling process (see fig. 3.6). In this case, the lift-off process is not possible anymore because the evaporated metal can penetrate into this cracks. For the aluminum gate, the photoresist AR-U 4060 is chosen [49]. This resist is suitable for cold evaporation and not damaged at liquid nitrogen temperature. It is a photoresist which is normally used for negative processes (image reversal resist), but it can also be applied in positive processes. The resist is spun for 40 s at 5000 rpm onto the substrate and baked for 2 min at 94 °C on a hotplate. The structures are carefully aligned with the alignment marks using maximal microscope magnification of the UV mask aligner. Then, the sample is illuminated in hard contact mode. The development is done with Allresist developer AR 300-26 and carefully rinsed with water and blown dry. The process parameters are described in detail in Appendix C.3. After this, 25 nm of aluminum are evaporated at moderate rates of about 0.43 nm/s at 77 K. Too slow and too fast evaporation rates yields in higher surface roughness. After evaporation, the sample is slowly warmed up to room temperature in the load-lock. Then, the load-lock is flooded with pure oxygen to a pressure of around 100 mbar for 10 to 30 minutes. Afterwards, the sample is transfered to the plasma asher and oxidized for 10 minutes in 100 W oxygen plasma at 1 mbar. The used photoresist AR-U 4060 is stable to the plasma for this time. After plasma oxidation the lift-off is done in acetone at 50 °C. A short sonication pulse is applied to avoid sidewalls on the gate electrodes. With these parameters, it was possible to get a very smooth surface. Atomic force microscope measurements on this samples showed a surface roughness of around 1 nm. For further treatment it is important to use no chemicals which are etching or attacking the thin aluminum oxide layer on top of the

gate structure (for example developers for optical resists, HF, etc.). The aluminum gate structure is shown in figure 4.2 b).

4.2   Electron-beam lithography

The nanoconstrictions in which the gaps for the molecules are formed by electromigration are created by electron-beam lithography. Two different designs are tested: shadow evaporation under a resist bridge and direct writing of narrow lines. For the following electromigration it is very important that the constrictions are pure gold, very thin and small to provide conditions for controlled electormigration. The reasons are discussed in detail in chapter 5.

4.2.1   Sample preparation

After all optical lithography steps, the sample is cleaned in the plasma asher for 10 minutes at 100 W. This removes all process chemicals from the UVL.

Due to the inadequate precision of the alignment of the two steps of optical lithography, the positions of the aluminum oxide gate structures are slightly varied over the sample. Therefore it is not possible to align the EBL and the photolithography part without a few μm shift between the gold and aluminum oxide structures. In Figure 4.7 the misalignment is shown. The misalignment is defined by the difference between the to distances d_1 and d_2. Hence different files with slightly changed distances, adjusted to the real electrode locations, are used. First the results after the two photolithography steps are checked in the SEM at 5 kV in the In-Lens-detector mode. This correction is introduced into the design files of the structures in Elphy.

4.2.2   Shadow evaporation

A common method to create nanoconstrictions for electromigration is shadow evaporation [50], [51], [46]. A bilayer resist system is used to create resist bridges. Two resists with different sensitivities and contrast are applied. Normally, double-layer resist systems are used to achieve a reliably working lift-off process (see section 3.2.3). The top layer (image layer) gives the exact geometry of the structure. Therefore, a resist with high contrast, that means a very sharp change from exposed to unexposed area, is used. The bottom layer is a resist with lower contrast, but higher sensitivity to produce an undercut for a good lift-off. For resists with higher sensitivity, less exposure energy (electron dose) is needed. Additionally, by backscattering of the electron beam from the substrate, a wider area of the sensitive bottom resist layer is exposed and gives, after the development, an undercut in respect to the top layer of resist. This undercut after exposure and development is shown in figure 4.7.

To create a resist bridge, a bottom layer resist with a very high sensitivity is needed. PMMA/MAs have a three to four times higher sensitivity than common PMMA resists [37]. Figure 4.7 shows a structure with the bilayer resist system after development. It is clearly visible that the bottom layer is much more sensitive and a much bigger area
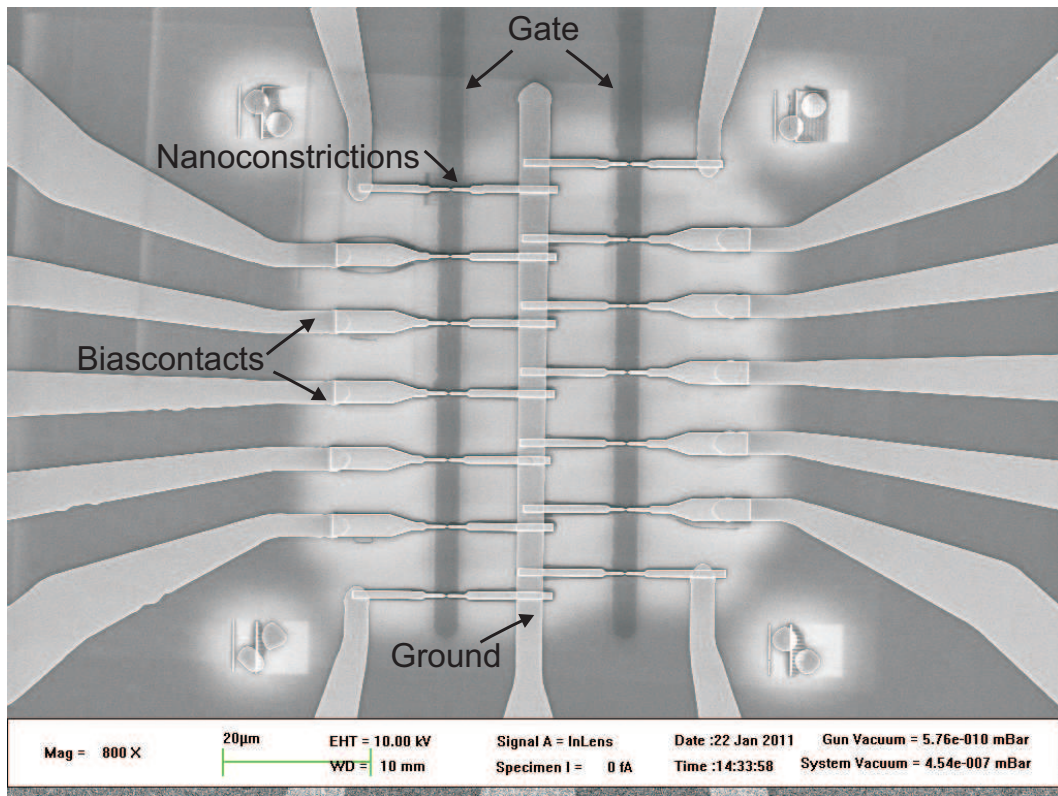
Figure 4.6: *SEM image of the inner part of one structure. The gate and the ground electrodes are visible. The nanoconstrictions are in the middle on the gate.*
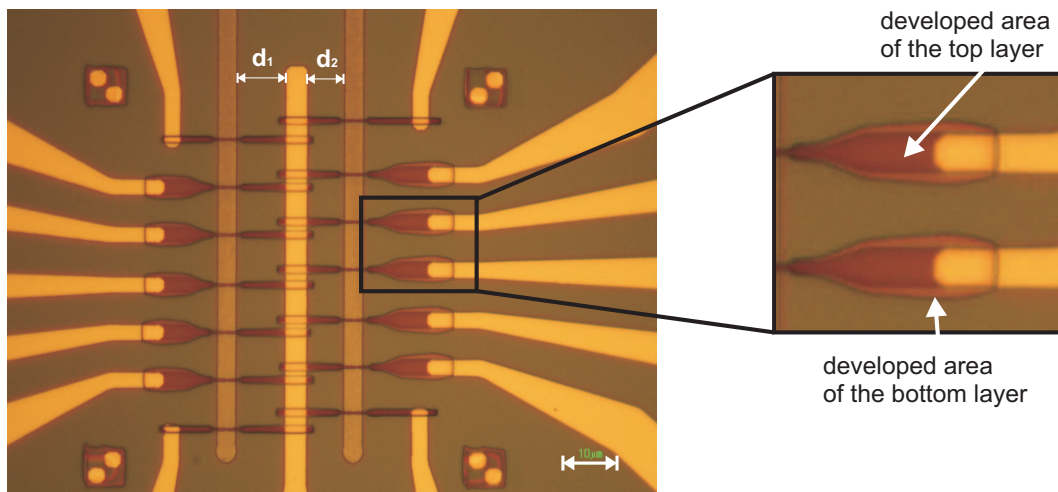

Figure 4.7: *Structure after exposure and development. The darker region of the exposed structure marks the shape of the top layer resist. The brighter edges of the structures indicate the developed area of the bottom layer. An undercut of several hundreds of nanometers is created by this bilayer resist system. The distances d_1 and d_2 show the misalignment between the two steps of photolithography (explained in section 4.2.1). The white scale bar corresponds to 10 μm.*

is affected by the electron beam exposure and electron backscattering. The undercut is around 300 nm. This is enough to create a resist bridge with of 100 nm width.

In figure 4.8 the complete process is schematically shown. First, a double-layer resist
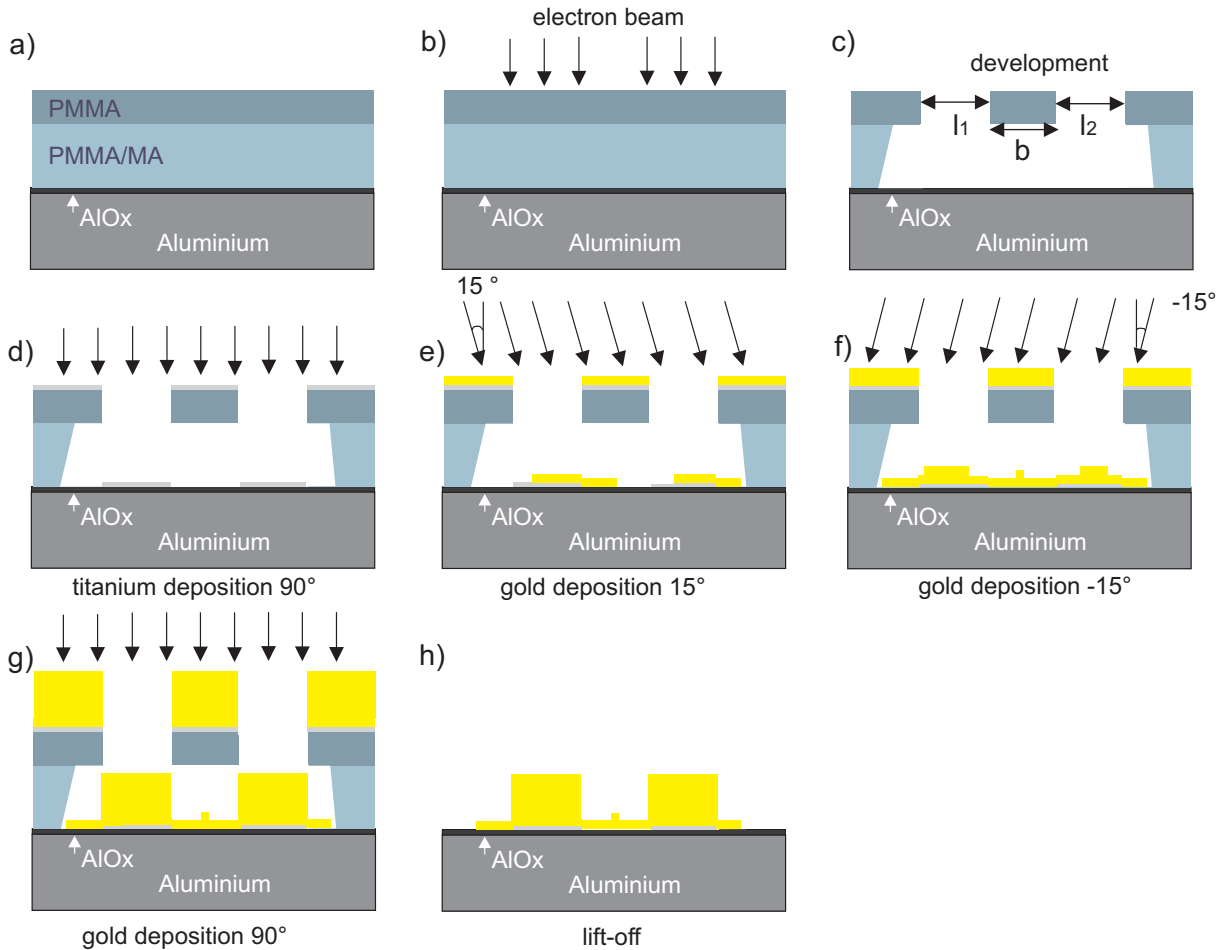

Figure 4.8: *Schematics of the shadow evaporation process. a) A bilayer resist is spun onto the substrate. b) and c) Exposure and development of the exposed area. In the bottom layer, an undercut is created. It has to be considered that the length of the exposed structures l1 and l2 are more than 10 μm. The length b of the resist bridge is only 100 nm. The structure is zoomed in horizontal direction for better understanding and easier drawing. From d) to g) the subsequent evaporation steps are shown. First a sticking layer of titanium is evaporated, followed by the angle evaporation of the nanoconstriction and the deposition of 100 nm gold to connect the EBL structures with the ones created by optical lithography. h) shows the finished nanostructure after lift-off.*

system with Allresist PMMA/MA 33 % (AR-P 617 S1 (8%) as bottom layer is spin-coated at 6000 rpm for 40 s and baked at 210 °C for 60 minutes. This resist has a layer thickness of 395 nm for these spin-coating parameters (see figure 3.2). As a top layer, PMMA AR-P 679 (950 K, 3 %) is spin-coated at 6000 rpm for 40 s and baked at 180 °C for 60 minutes.

This top layer resist requires a much higher area beam dose than the bottom layer. The area beam dose is determined by dose tests for the 100 nm wide and 100 nm separated structures. Structures which are 100 nm or smaller are exposed with an electron-beam energy of 30 keV using a 30 μm aperature with an area dose of 1050 μC/cm^2. For bigger structures, an area dose of 500 μC/cm^2 is adequate. After the exposure, the development in isopropanol with a temperature of 25 °C for one minute is done. This is followed by a dip of some seconds in a sonicator. Then, the sample is rinsed for one minute in water. A resist brigde as shown in Figure 4.8 c) is formed.

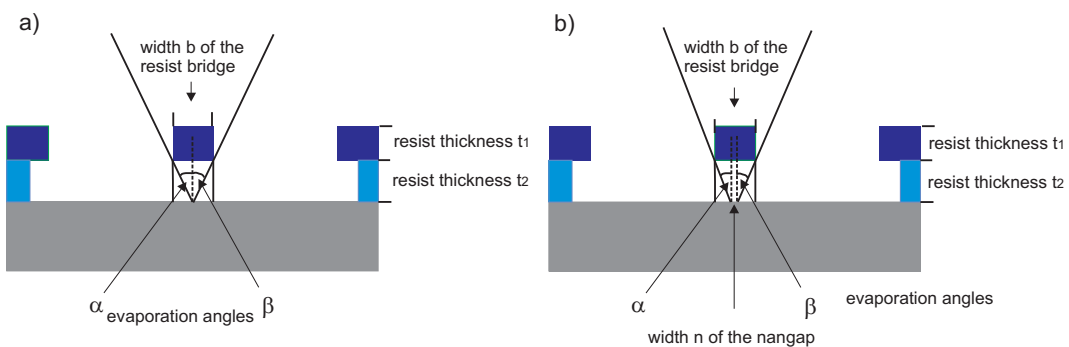The most critical step in the process is the shadow evaporation itself. The angles for the

Figure 4.9: *Schematics of the angle calculation: a) Calculation of the angles α and β for overlapping structure suitable for electromigration. b) Calculation of the angles α and β for nanocontacts n with a separation.*
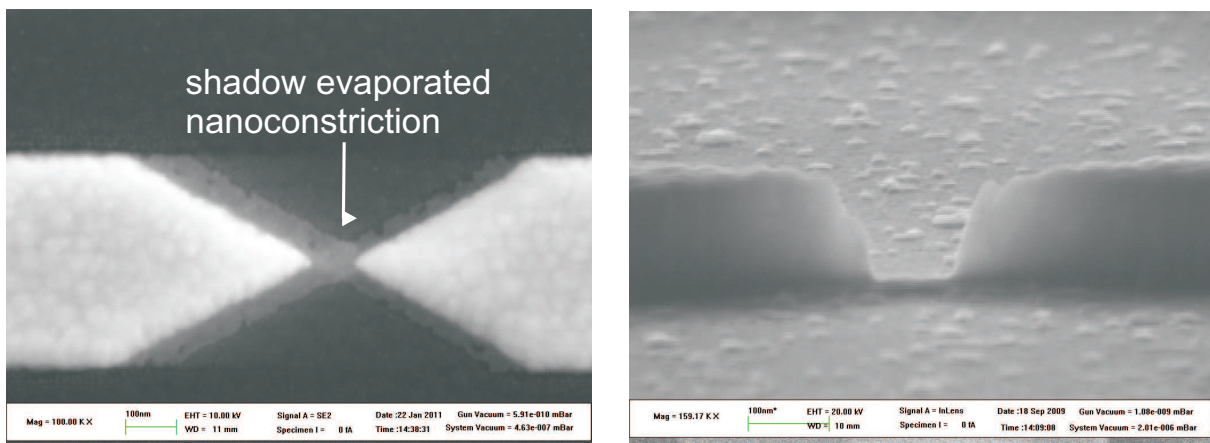

Figure 4.10: *a) Nanoconstriction after shadow evaporation. The brighter structure is the exposed image and for the stability 130 nm thick. Clearly visible is the shadow of the structure, which is overlapping in the middle. The shadow evaporation is pure gold around 8 nm thick. b) Side view of the nanoconstriction: In the middle of the gate the thinner part created through the shadow evaporation is visible. The outer connection lines have to be thicker than the gate to be not interrupted by the roughness of the bottom surface.*

evaporation are calculated by geometric considerations (see figure 4.9 a)). With equation 4.1 the evaporation angles α and β depend on the thickness of the bottom layer resist t_2 and the width of the resist bridge b:

$$\alpha = \beta = \arctan \frac{b}{2t_2} \tag{4.1}$$

For a resist bridge with a width of 100 nm and a thickness of the bottom resist layer of 400 nm, an evaporation angle of 7.2° from each side gives a contact. To have an complete, guaranteed overlap from both sides an angle of 15° is used, because it is difficult to set a precise angle at the evaporation machine. Also, it is very important that the sample is mounted in the correct angle on the sample holder. The first three evaporation steps are done in the upper evaporation chamber of the electron-beam evaporator. There the sample is one meter away from the metal-source and the electron-gun used to evaporate the metal and thus, it is not affected by heating. Furthermore, the control over the deposition rate is more reliable in this position. First, the sample plane is kept perpendicular to the evaporated metal source. About 2 nm of titanium are deposited at a rate of 0.03 nm/s. This layer serves as sticking layer for the gold leads which are connecting the high resolution structures made by EBL to the optical lithography structures. It is important for subsequent electromigration that there is no titanium deposited under the resist bridge (figure 4.8 d)). Then, the manipulator is tilt to an angle of about 15 ° and 8 nm of gold are evaporated at a rate of 0.045 nm/s. The material is now deposited under the resist bridge. The process is repeated for -15°. An overlap of the thin gold layers under the resist bridge is created (figure 4.8 e) and f). The overlap has a thickness of about 16 nm and a width of about 50 nm. This is now the predetermined breaking point for the electromigration process. For the last evaporation step,the sample is mounted in the lower position of the machine. There, due to the shorter distance, the evaporation is 6.66 times faster. The sample is mounted in a perpendicular position and 100 nm gold are evaporated with a rate of 0.5 nm/s to connect the nanoconstriction with the contact pads (figure 4.8 g). After metal deposition the lift-off process is done in 50°C acetone for several hours. Figure 4.10 shows the top and the side view of an overlapping nanoconstriction before electromigration.

Furthermore, shadow evaporation gives the facility to create a nanogap n directly, without electromigration. This technology gives the possibility to structure big molecules ($\geq$ 10 nm) which are already deposited on the wafer. This could be interesting for graphene molecules or discs [5]. In figure 4.9 b) the geometric reflection for the evaporation of nanocontacts with a separation n is shown. Equation 4.1 is modified to 4.2:

$$\alpha = \beta = \arctan \frac{b-n}{2t_2} \tag{4.2}$$

The size of the nanogap depends on the width of the resist bridge, the evaporation angles and the resist thickness. The resist thickness can be considered as stable. The width of

the resist bridge is determined by dose tests. The adjustment of the evaporation angles is crucial. It can be done with an accuracy of $\pm$ 5 °. For the e-beam lithography a double-layer resist system with the resist PMMA 50 k (bottom layer, 90 nm thick) and PMMA 950 k is applied. The PMMA 50 k (AR-P 639.04) is spin-coated at 3000 rpm for 40 s and baked at 200 °C for 60 minutes. The top layer resist (AP-R 679.03) is spin-coated at 5000 rpm for 40 s and baked at 160 °C for 60 minutes. The process parameters for the exposure and development correspond to the parameters mentioned above and in table C.5 of the Appendix. Table 4.1 shows the variation of exposure and evaporation parameters for three different samples. The width n between the nanocontacts is measured with the SEM. It is possible to create nanogaps by shadow evaporation with sizes between 5 and 50 nm. The dose for the e-beam exposure is determined by dose tests and it is the most important parameter of the sample fabrication. Reproducible results are obtained for small resist bridges with a width smaller than 50 nm. An 11 nm sized gap is shown in figure 4.11.

width b of the resist bridge in nm	evaporation angle of the gold layer in °	thickness of the gold layer in nm	width n of the nanogap in nm
100	$\pm (30 \pm 5)$	10	65 - 100
50	$\pm (30 \pm 5)$	10	33 - 14, connection
20	$\pm (30 \pm 5)$	10	25 - 11, connection
100	$\pm (20 \pm 5)$	10	90 - 100
50	$\pm (20 \pm 5)$	10	30 - 40
40	$\pm (20 \pm 5)$	10	17 - 20
30	$\pm (20 \pm 5)$	10	13 - 20, connection
20	$\pm (20 \pm 5)$	10	connection
10	$\pm (20 \pm 5)$	10	connection
20	$\pm (20 \pm 5)$	7	<3 - 10, connection
10	$\pm (20 \pm 5)$	7	5 - 40, connection

Table 4.1:   *Results of the shadow evaporation by variations of the different exposure and evaporation parameters. The error of the evaporation angle is estimated by practical experience. The different width of the nanocontacts for the same evaporation parameters depend on the position of the structure on the sample and the exposure dose which is varied.*

4.2.3   Lines

A second possibility for the geometry of the nanoconstrictions is to write a small line which gives the predetermined breaking point for the electromigration. The width of the lines is 30 nm or less. For the reasons discussed in chapter 3.3.2, the width is not defined
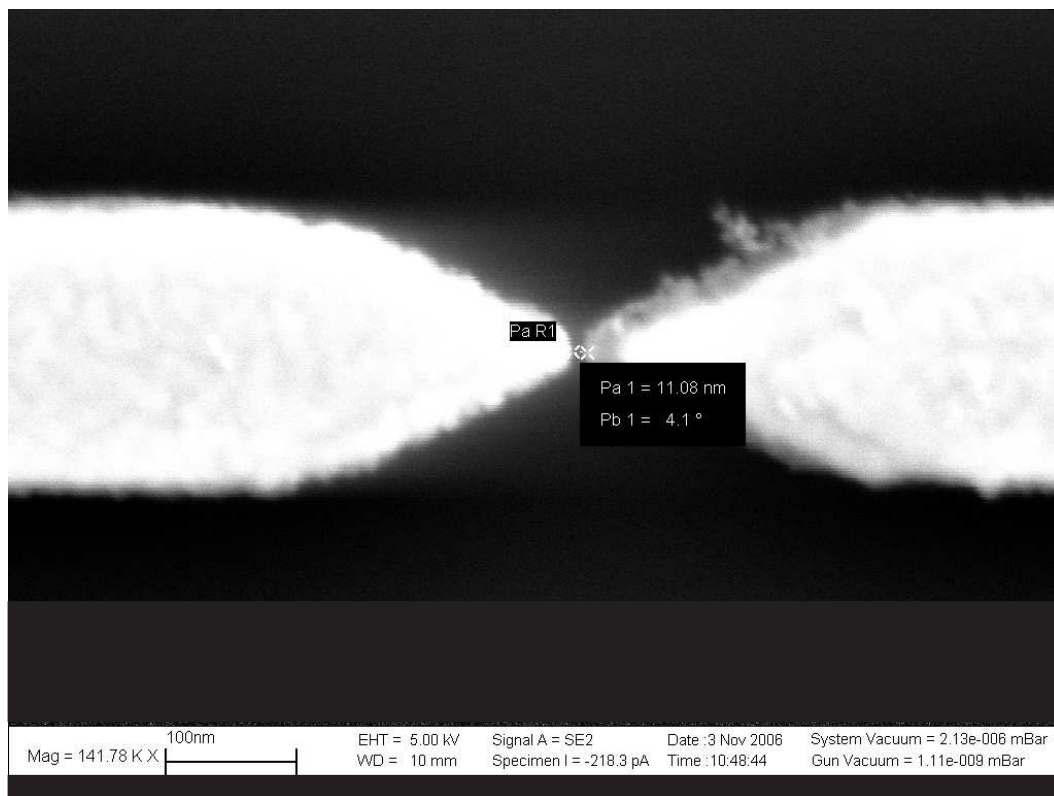
Figure 4.11: Shadow evaporated nanocontact: the shadow evaporation is done only from the right side. The width n of the contact is 11 nm.

as single pixel lines. Dose test showed that a width of 30 nm is reliable to write over an area of 1 cm^2. For this geometry a second EBL step is inevitable. After the first process step, the writing of the lines in the middle of the gate structure, at the second step the lines have to be connected to the contact pads created by UVL.

For the first step the resist PMMA AP-R 679 (950 K, 3 %) is spin-coated at 6000 rpm for 40 s and baked at 180 °C for 60 minutes. The exposure is performed with an acceleration voltage of 30 keV. The aperature of 10 μm is chosen and a step size of 2.5 nm selected. The dose for the 30 nm wide nanoconstriction was determined by dose tests. The exact values are presented in the Appendix C. The focus and the stigmation are adjusted at a magnification of 150000. This is important for the small structures. After the exposure the development is done in isopropanol for 60 seconds. For the evaporation the upper chamber is chosen. 10 nm of pure gold are evaporated with a rate of 0.045 nm/s. The lift-off is done in acetone at 50 °C.

For the second EBL step to connect the nanoconstriction with the UVL part the recipe of the shadow evaporation is used. This bilayer resist system has a very big undercut and is suitable for a working lift off process. The exact recipe is listed in Appendix C.6.

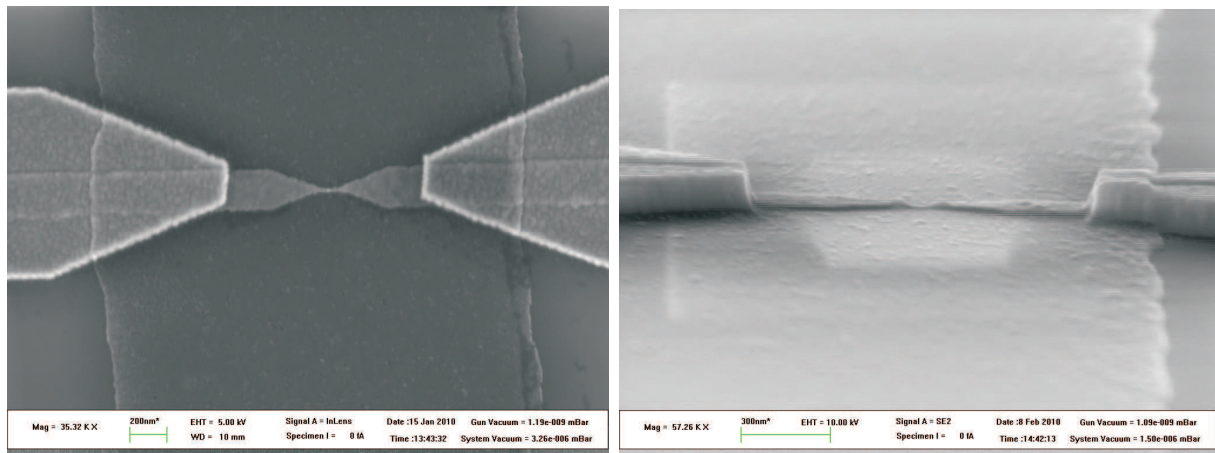The advantage of this geometry is that the evaporation of the gold is perpendicular

Figure 4.12: *a)SEM picture of a 20 nm wide line. b) Sideview of the line.*

and so no mistakes can happen during the evaporation. Furthermore, the width of the nanoconstriction can be changed and the thickness is defined by the evaporation and not from the overlap of the shadows. However, the disadvantage is the second step of EBL, which takes another 3 hours for one sample with 1400 nanoconstrictions.

4.3   Molecule deposition

Different molecules are measured during the work of this thesis. The molecules are usually delivered in highly purified crystal form and are stored in a dry, non-corrosive environment. For deposition, the molecules are dissolved in adequate solvents. The solvent must be able to solve the molecule and its vapor pressure should be low enough that it does not evaporate fast at room temperature. Possible solvents are dichloromethane, chloroform, toluene and tetrahydrofuran. For its handling toluene is chosen for our solutions. Solutions with different concentrations are prepared (0.1 mmol - 0.1 mol). The concentrations for the different molecules measured in this thesis is given in chapter 6. To dissolve the molecules completely in the solvent and to avoid clustering of the molecules the solution is treated for several hours in a sonicator at 50 °C. Then, the solution is kept for several days in a refrigerator at 5 °C. The molecular clusters can sink down whereas the small molecules stay in the upper part of the solution.

The molecules can be applied on the sample before or after the electromigration. For measurements in the probe station both is possible but for measurements in the cryostat it is easier to do it before mounting the sample. To bring the molecules on the sample, a droplet of the solution is pipetted over the structures and after a few seconds blown away with nitrogen gas. This process is repeated several times to increase the chance that molecules bind on the sample surface. The samples is than glued into a chip carrier and bonded. The gold contact pads are bonded with gold wire. The Al_2O_3 gate is bonded with aluminum wire, gold wires are not sticking on aluminum oxide surface. After bonding, the sample is mounted into the cryostat as fast as possible to avoid contamination from the environment.

Chapter 5

Electromigration

Various possibilities exist to create molecular junctions. These include mechanical breaking technique [52], electrochemical deposition [53], lithographic structuring (chapter 3 and 4) and electromigration [50]. In this thesis all gaps used for single-molecule measurements are fabricated by electromigration (EM). Electromigration is forced atomic diffusion due to high electric fields and high electric current densities [54], [55]. At very high current densities (10^5 to 10^6 $\frac{A}{cm^2}$) the conduction electrons can transmit momentum to the atom cores in the lattice, through impacts at defects and grain boundaries [56]. This fact leads to a motion of the atoms in current direction, to a material transport in the conductor and finally to an interruption or a gap in itself. It is known as one of the most common defects in integrated circuits since the early sixties [54]. At this time scientist started to investigate the mechanisms of electromigration to limit the destruction of integrated circuits. The theoretical basics to explain the EM were postulated by James Black and Ilan Blech in the sixties and seventies [54], [55]. In 1999 H. Park started to use controlled electromigration to form nanogaps in thin gold nanowires for single-molecule transport [50]. It is possible to create nanometer spaced electrodes with this technique. Another method for the EM with controlled feed back loops at room temperature was published in 2005 [51]. In this thesis both technologies are tested in a cold probe station at 15 K. The results are discussed in section 5.3. First a theoretical approach to the mechanism of the EM is given in section 5.1. In section 5.2 the explored algorithms are described.

5.1 Electromigration mechanism

The first theoretical descriptions for the explanation of electromigration were done by James Black and Ilan Blech in the sixties and seventies [54], [55]. They investigated the electromigration phenomenon in thin aluminum films used at this time in the fabrication of semiconductor devices. Here a short microscopic description based on the investigations of Black and Blech is given to understand the process of EM. A detailed description of EM was given by Lloyd in a review [57]. The theoretical approach is reported by Sorbello [58].

In a metallic conductor a high electric DC current can cause a mass flux of metallic atoms. This process is called electromigration and based on atomic diffusion. The metal atoms are kept together in the metal lattice due to their valence electrons. At the same time acts a repulsive force between the positive charged lattice atom cores. That means that the atom cores are situated in a potential well, in which they can thermally oscillate. The kinetic energy of the ions in a material is statistically distributed and follows the Boltzmann distribution (see figure 5.1).

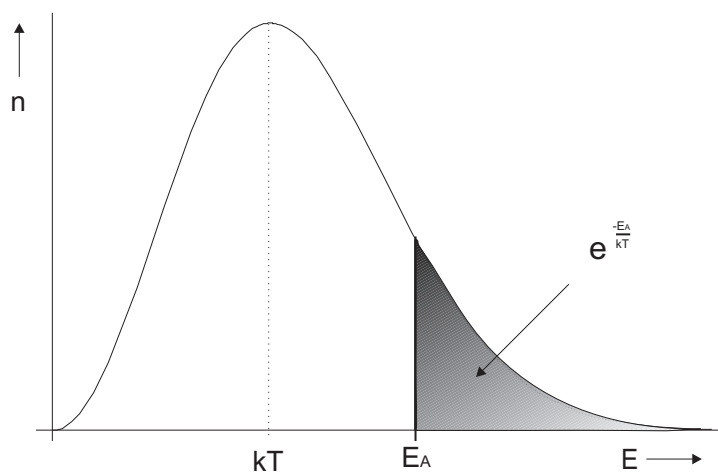Corresponding to this distribution a particular percentage of the atoms has a kinetic

Figure 5.1: *Boltzmann distribution*

energy with a value higher than the activation energy. This part of the atoms has a high enough kinetic energy to change its lattice position. The part p of atoms with energies higher than E_A is described by the equation of the Boltzmann distribution:

$$p = exp(-\frac{E_A}{kT}) \qquad (5.1)$$

with k is the Boltzmann constant and T as absolute temperature. In figure 5.1 this part of the atoms is illustrated by the dark area under the curve. Atoms in this region are

able to diffuse or to fall back into the potential well. The diffusive process of atoms in their lattice is called self-diffusion and is an isotropic, temperature dependent, statistical process which will not cause a net mass flux if there does not exist a concentration or chemical gradient. Other sources for electron scattering than thermally excited lattice ions are defects in the lattice like grain boundaries, surfaces and vacancies. These defects are more important for electromigration. For atomic diffusion a pathway, which can be given through these defects, is inevitable. Atomic diffusion is a random process without a defined direction. The application of an external electric field to the material causes an electron flow. The directed conducting electrons scatter at the atomic defects and a net flow of matter in the direction of the current is caused. Figure 5.2 shows the forces acting onto the atoms in the metal lattice.

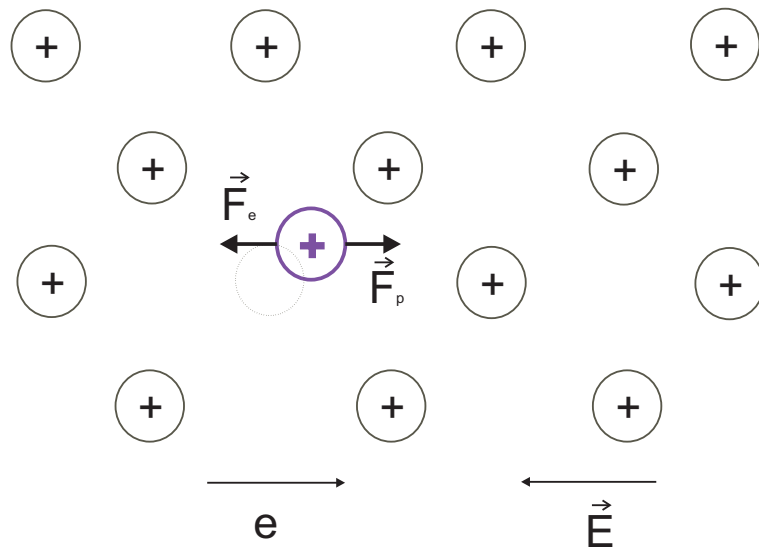The process of electromigration is traditionally described by the use of an electrostatic

Figure 5.2: *Schematic drawing of the forces onto the metal ions caused by the electric field and through the flow of the conduction electrons.*

analogue [57]. Two forces act onto the metal atoms: the electrostatic force $\vec{F}_e$ due to an external electrical field $\vec{E}$ and the force $\vec{F}_p$ due to the momentum exchange between flowing charge carriers and the atom cores. The resultant force is

$$\vec{F} = \vec{F}_e + \vec{F}_p \tag{5.2}$$

This driving force, also called electron wind force, can be expressed by

$$\vec{F} = Z^* e \vec{E} \tag{5.3}$$

where Z^* is the effective charge number, e is the elementary charge and $\vec{E}$ is the electric field. The electric field $\vec{E}$ can be expressed by

$$\vec{E} = \rho\vec{j} \tag{5.4}$$

with ρ the metal resistivity and $\vec{j}$ the current density of the electrical conductor. The effective charge number Z^* is divided into an electrostatic part Z_{el} and a wind part Z_w as

$$Z^* = Z_{el} + Z_w \tag{5.5}$$

and has been expressed by Huntington [59] as

$$Z^* = \frac{1}{2}\left(\frac{\rho_d N}{\rho N_d}\right)\frac{m^*}{|m^*|} \tag{5.6}$$

where ρ_d is the specific defect resistivity, N is the density of conduction electrons, ρ is the metal resistivity, N_d is the defect density and m^* is the effective mass of the electron near the Fermi surface taking part in the momentum exchange. F in equation 5.3 can be positive or negative depending on the sign of the effective mass of the charge carriers m^*. The Einstein relation for diffusion in a potential field and the electrostatic analogue of equation 5.3 gives the drift velocity v_{em} of metal atoms due to the electromigration force

$$v_{em} = \frac{DF}{kT} = \frac{DZ^*e\rho j}{kT}. \tag{5.7}$$

The diffusion coefficient D is defined as a product of the diffusion constant D_0 with the part p of the atoms, which have energies higher than the activation energy E_A

$$D = D_0 exp(-\frac{E_A}{kT}). \tag{5.8}$$

From equation 5.7 follows that the mass flux is directly proportional to the current density and to the diffusion constant. The drift velocity v_{em} is a function of the diffusion pathway and the temperature dependent activation energy E_A of the diffusion mechanism. For a mass flux density $\vec{J}$ due to the above described mechanisms, follows

$$\vec{J} = \frac{NeZ^*\rho\vec{j}}{kT}D_0 exp(-\frac{E_A}{kT}) \tag{5.9}$$

where N is the density of metallic ions.

Furthermore, the mass transport depends on the sum of the chemical potentials that act on the diffusing metal atoms. For qualitative observations, the concentration gradient of vacancies is the most important chemical potential for atomic transport. More about other potentials, like stress gradient, can be found in [57]. In absence of stress gradients, the mass flux is the sum of the chemical potentials due to the concentration gradient and the electromigration driving force (see equation 5.9)

$$J = D \left(\frac{\partial c}{\partial x} - \frac{Z^* e \rho j}{kT} c \right) \tag{5.10}$$

where c is the vacancy concentration [57]. From equation 5.10 it follows that electromigration will only cause a gap if there is a divergence in the vacancy flux somewhere within the nanoconstriction, that allows the formation of extrusions. Otherwise the gold atoms will be transported from one gold contact pad to the other one [60]. A directed vacancy flux can be created through gradients in the temperature and in the grain structure or by material gradients.

For the devices in this thesis all three gradients lead to the formation of the nanogaps. The design of the nanoconstrictions defines directly a gradient in material and in the grain structure. The thickness of the gold in the shadow evaporated nanoconstrictions is between 10 and 16 nm, compared to the 100 nm of the leads. Figure 4.10 b) in section 4.2.2 shows the difference in height. Furthermore the geometry of the structure is narrowed in its center to have a predetermined breaking point. The use of pure gold for the nanoconstriction without the titanium sticking layer on top of the aluminum oxide gate, avoids the diffusion between this two materials. The same arguments go for the narrow lines in section 4.2.3.

5.2   Electromigration algorithm

The use of electromigration to fabricate metallic electrodes with nanometer separation
was first reported by Park in 1999 [50]. He fabricated the nanoconstrictions by shadow
evaporation (see section 4.2.2). The gap formation was done by controlled passage of current
through the nanoconstriction. The bias voltage was ramped through a 100 Ω series
resistor with a rate of 300 mV/s. The voltage drop across a nanowire was monitored in
a four-probe configuration. The conductance of the nanowire was calculated and moni-
tored during the breaking process. The electromigration was performed at liquid-helium
temperature. Park claimed in his paper that the gap size achieved with this algorithm
was about 1 nm. The final tunnel resistance of the constrictions measured after EM was
between 10^5 and 10^{11} Ω[1].

In 2005, Strachan et al. reported about the fabrication of nanogaps in ambient envi-
ronment by a controlled feedback loop [51]. They fabricated the nanostructures also by
electron-beam lithography and shadow evaporation. The electromigration is performed
by a succession of voltage ramps while monitoring the current and the conductance. The
conductance is initially measured for comparisons during the following voltage ramps.
When the conductance decreases by a certain threshold percentage (from 1 - 150 %) the
voltage is ramped down to arrest the breaking of the nanowire. The ramping procedure
is then repeated with a higher threshold to form slowly the nanogap. The formation of a
nanogap, with a resistance of about 10 GΩ using this method, takes between one and two
hours. Faster EM due to higher thresholds degrades the reproducibility of the process[2].

These first nanogaps produced by electromigration were structured on Si/SiO_2 substrates.
In later experiments the nanoconstrictions were structured on a local Al/Al_2O_3 gate elec-
trodes [44], [46]. The EM algorithms used in these publications were also active feedback
loops, comparable to [51]. The goal in this thesis was to have a high yield of nanogaps.
Different algorithms are investigated to find the optimal electromigration parameters. The
first tests are performed on a probe station with four probes at room temperature. The
measurement setup was equipped with a 16-bit voltage output card 6208V from Adlink
as voltage source and nanovoltmeters 34420A from Agilent for the voltage measurement.
The measurements were controlled by a LabView program. The reaction time of the
setup was in the range of milliseconds. The yield of gaps smaller than 10 nm was about
60 % of the structures, but only 5 % were smaller than 5 nm [61]. This yield was not
suitable for the measurements of single-molecules in a dilution refridgerator. The most
critical parameter for the control of the EM is the reaction time to stop the voltage ramp.
An ADwin-light-16 system is specified for real time measurements and suitable for the
control of electromigration. The ADwin system is optimized for short process cycle times

---

[1]This is a summarised description of the process and the results of the paper from Park [50]
[2]The description of this process is a summarisation of the results of the paper from Strachan [51]

in a range of microseconds. It is especially designed for real time measurements. The ADwin box has its own signal processor with a reaction time of 300 ns included [62]. An integrated timer allows a time resolution of 25 ns. The ADwin system performs measurements independent of the computer but is in continuous data exchange via USB with it. The measurement programs for the ADwin are written in a BASIC syntax, ADbasic, compiled and loaded onto the ADwin box. The communication between ADwin and the PC is performed by an ActiveX interface as a part of a LabView library. The electrical circuit used for the electromigration is illustrated in figure 5.3.
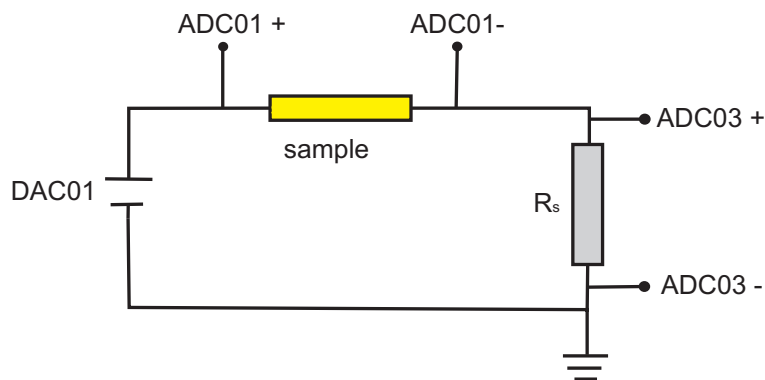
Figure 5.3: *Electromigration circuit diagram: The voltage is applied to a reference resistor in series with the nanoconstriction indicated by a second resistor (sample) in the circuitry. The voltage source is the analogue voltage output of the ADwin card (DAC01). The voltage drops over the sample and over the reference resistor are measured by the differential inputs (ADC01 and ADC03) of the ADwin card. The card is controlled by a PC.*

Furthermore the ADwin-light-16 system has two analogue voltage outputs (DAC) and eight analogue input channels. The analogue inputs (ADC) work differentially and are handled by a single multiplexer. The time limitation of the system is given by the maximum settling time of 6.55 μs for a maximum voltage of 20 V and the A/D sampling rate. The 16-bit A/D converters have a resolution of 305.175 μV, if the whole range of 20 V is used. The sampling rates are determined by a conversion time of 10 μs. The disadvantage of the system is its low input resistance of 30 kΩ. In this thesis the ADwin-light-16 system is only used for the electromigration process. The single-molecule measurements are done with common log-in amplifiers. More details about the Adwin-light-16 system are described in [62].

The circuit for the electromigration is given in figure 5.3. For the current measurements a reference resistor is wired in series with the sample. The total resistance of the measurement circuit should be between 10 and 500 Ω. For the use of a cryostat inset with a high lead resistance ($\approx$ 500 Ω), a small series resistor (10 Ω) has to be used. The voltage is applied by the ADwin-light-16 system. The voltage drop over reference resistor

and sample are read out by the ADwin box. The program is designed for a feedback loop. An example process for the electromigration is shown in figure 5.4. First the initial resistance of the sample is determined. Then the voltage is ramped up and the sample resistance is measured. If the resistance is in a certain interval, electromigration is attempted. The voltage is ramped up at a given sweep rate and the resistance of the sample is measured. As soon as the resistance of the structure has changed a certain percentage, the applied voltage is immediately reduced. Than the voltage is ramped up again. This cycle is repeated until the voltage or the resistance reaches the termination point for the electromigration conditions.

The following parameters for the electromigration can be controlled by the user:

- the minimal and maximal resistance for the electromigration to be attempted in Ω,

- the sweep rate for the ramped up voltage in V/s,

- the resistance change per ramping cycle in %,

- the voltage to ramp back during one cycle in %,

- the terminating voltage in V,

- the terminating resistance in Ω.

The program gives the possibility to perform the electromigration by the above mentioned active feedback loop. Furthermore it is possible to set the resistance change per ramping cycle to very high values (1000 % or even higher). In this case the voltage is ramped up to the terminating value and the process stopped by this criterium or when the terminating resistance is achieved. The EM is than performed only by ramping the voltage up to the breaking of the nanoconstriction and not by the active feedback loop. A printed and completely commented version of the program is given in [40].
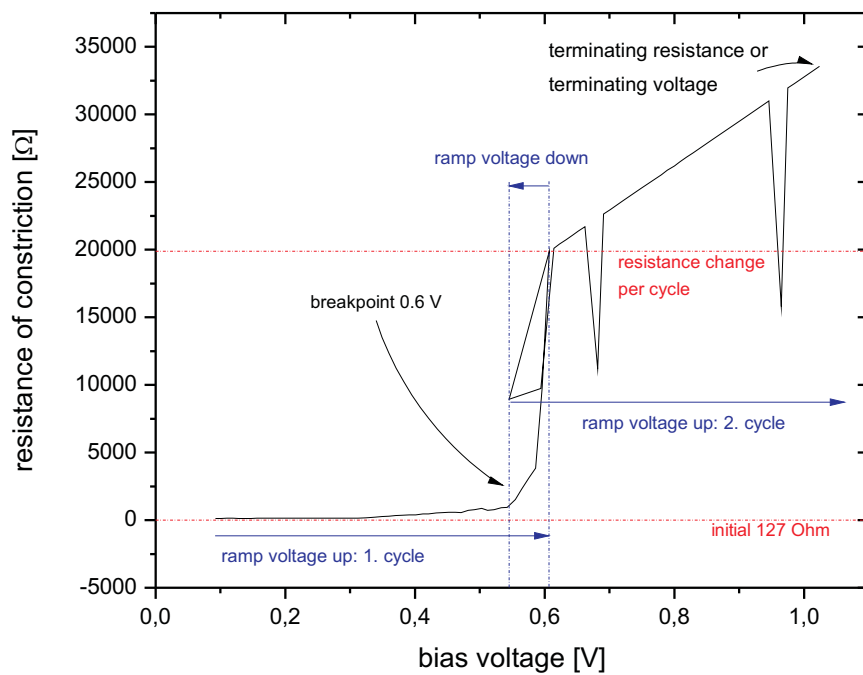
Figure 5.4: *Electromigration cycle: The initial resistance is measured. Then the voltage is ramped up until the resistance changes certain percentage or value (here 20 kΩ). The voltage is ramped down to a user defined fraction and up again. The cycle is repeated until the voltage or the resistance reaches a certain defined terminating value (here 1 V). The figure is adapted from [40].*

5.3   Electromigration results

First, statistical electromigration tests are done to gain an understanding of the influence of different parameters onto the electromigration process and on the gap size. The tests are performed in a probe station[3] with 4 probes. The probe station is a flow cryostat and can be cooled down to 15 K by liquid helium. For the tests a sample with 700 shadow evaporated nanoconstrictions is used. Due to lift-off problems and process errors in total 641 structures were suitable for EM. The measurements are performed at a temperature below 50 K. Because of the amount of structures, several cooling cycles were necessary. The electromigration program is divided in two parts: the determination of the initial resistance of the sample and the active feedback loop. Figure 5.5 a) shows the initial resistances for all nanoconstrictions on the test sample. The maximum of the histogram is at about 88 Ω with a standard deviation of 23 Ω. The initial resistance gives an indication of the gold thickness of the nanoconstriction. Ideally, the resistance should be between 80 Ω and 200 Ω. Lower values indicate a very thick gold layer (more than 15 nm) and are not suitable for electromigration. Previous tests showed that very high current densities are needed to migrate low ohmic constrictions. Then, the EM process was difficult to control and melting of the nanoconstriction often occured or the local gate was destroyed. Higher initial resistance values indicate an incomplete, thin layer or a very rough and grainy surface. Here the difficulty was the total resistance of the circuit (series resistor, wiring and sample). It was not possible to reach high enough current densities for a controlled EM [61].

For the electromigration tests three parameters were varied: the percentage of resistance change, the fraction of the voltage to which is ramped back and the final resistance to stop the process (terminating resistance). For each set of parameters at least 14 constrictions from one structure were tested. A typical EM process is shown in figure 5.5 b). Here, a low series resistance (100 Ω) for the current determination is used. Several loops are realised. The percentage of the resistance change is set to low values. The figure shows the resistance development (black) and the bias voltage (red) over time. The fraction to which the bias voltage is back ramped was 0.5 for this example. The final resistance was set to 30 kΩ. Figure 5.5 b) shows the EM done with an active feedback loop process according to Strachan et al. [51].

After the EM the sample was analysed in the SEM and the gap widths were measured (at 10 keV with 30 μm aperture). With the available SEM it is not possible to resolve structure sizes smaller than 5 nm. All unresolvable structures were considered to have sizes between 0 and 5 nm. Further, the topology of the electromigrated nanoconstrictions was difficult to determine. Figure 5.6 shows different structures after EM. It is visible that the gap topology is different and unresolvable in detail. Schematic 5.7 shows side views of possible topologies. The different gap topology made the measurement of the gap size difficult. Furthermore, it had to be considered that the topology and the gap size
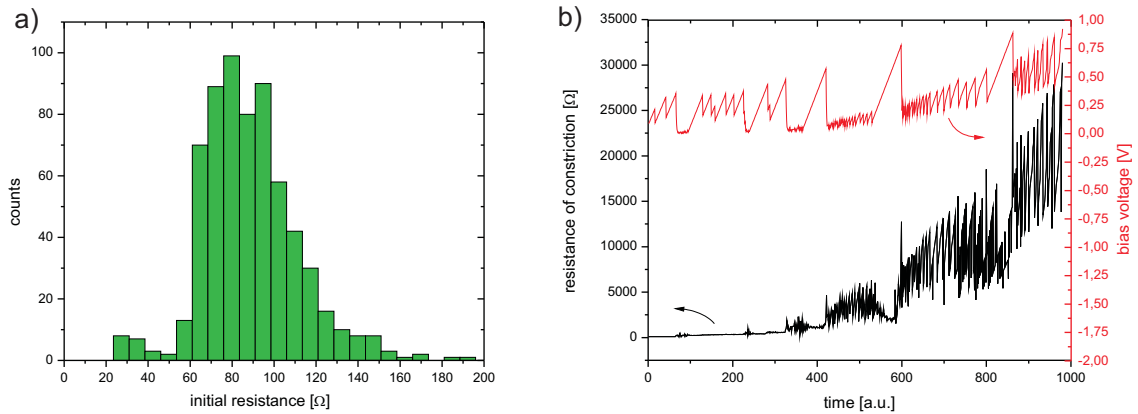
---

[3]desert cryogenics

Figure 5.5: *a) Distribution of the initial resistances measured before the electromigration. b) Typical electromigration process. Several cycles are needed for the migration. The development of the resistance (black) and the ramped bias voltage (red) are shown over time. The figure is adapted from [40].*
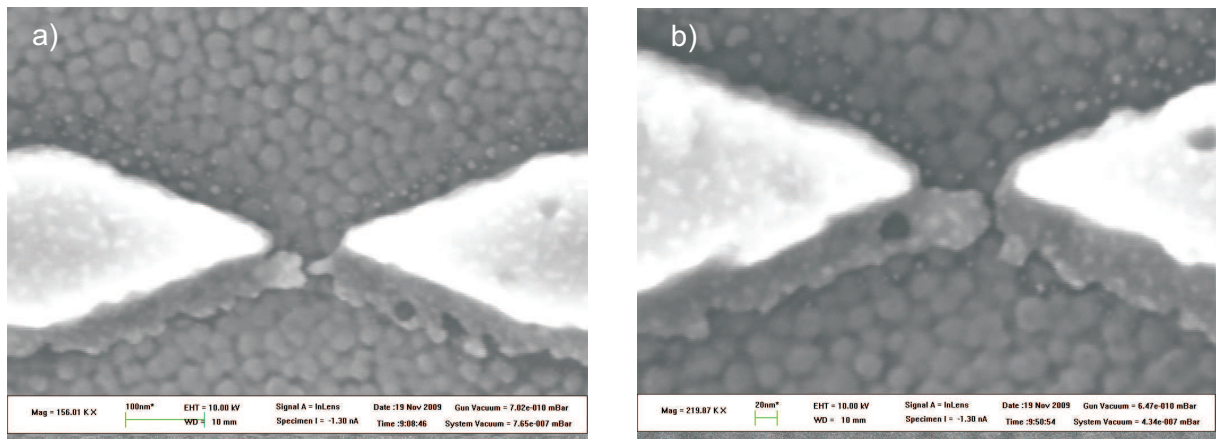

Figure 5.6: *Two nanoconstrictions after the electromigration. The gap sizes are smaller than 5 nm. Due to the topology of the gaps it is difficult to determine the gap size by SEM measurements.*
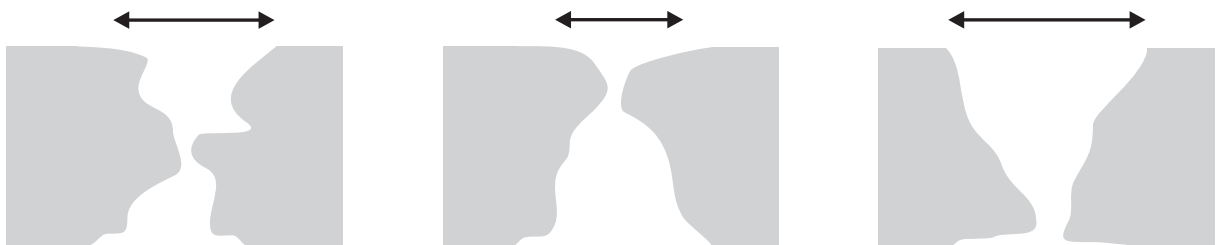

Figure 5.7: *Side view of possible topologies of the nanogaps after electromigration. The arrows show the distance which is visible with the SEM in the top view and the measured gap size.*

can change at room temperature. The values measured after the electromigration, give only an upper limit for the real gap widths. However, the measurement of the gap size by SEM can give an idea about the influence of the electromigration parameter variation.

Figure 5.8 a) shows a histogram of the measured gap sizes. For 17 constrictions, illus-
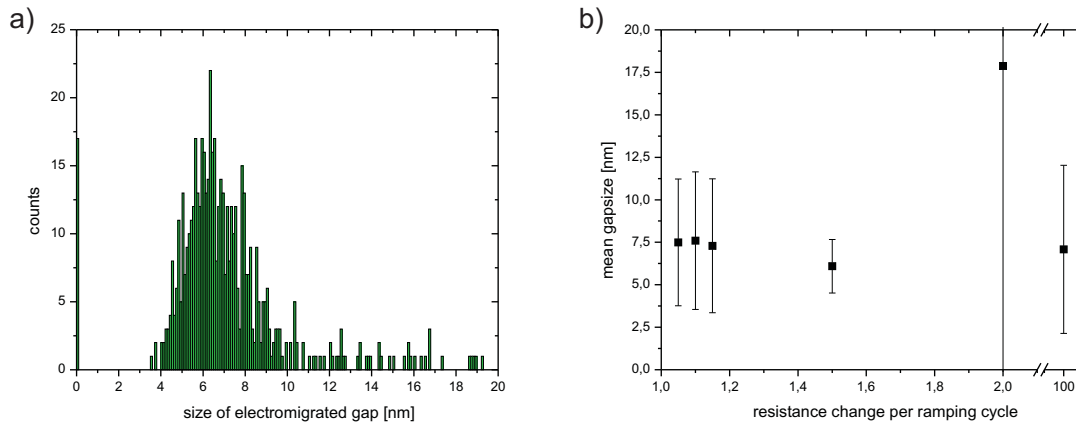
Figure 5.8: *a) Distribution of the gap sizes after EM. b) Dependence of the mean gap size from the factor of resistance change before ramping the voltage back. The figures are adapted from [40].*

trated in figure 5.8 a) with a gap size of 0 nm, the EM was not successful and they were still connected. In total, 86 gaps were unresolvable by the SEM measurement and had a width between 0 and 5 nm. Further, 2 gaps were bigger than 100 nm. The figure shows a mean value of 7.8 nm for the gap size with a standard deviation of 5.2 nm. In the figure the above mentioned unresolvable gaps were not included.

The dependence of the percentage of resistance change before ramping the voltage back on the gap size is shown in figure 5.8 b). The factors of the resistance change at which the voltage is ramped back were 1.05, 1.10, 1.15, 1.50, 2.00 and 100. For the lesser factors a behavior like shown in figure 5.5 b) is observed. The factor 100 leads to only one ramp. Therefore the bias voltage is ramped up to the breaking point of the nanoconstriction. Low factors correspond to long cycle times. Strachan et al. reported that higher factors and faster EM decrease the reproducibility of the process and often very big gaps are formed [51]. This behavior was not observed during the tests. The mean value and the standard deviation of the gap sizes in figure 5.8 a) do not show high variations. Only the values for the factor 2.0 attract attention. The high standard deviation is due to the fact, that a small number of nanoconstrictions was migrated with this parameter. The smallest mean value and standard deviation is achieved for a factor of 1.5. This factor gives also a reasonable time for the process.

Further, the fraction of the last voltage of one cycle, to which the bias voltage is ramped back, is examined. Figure 5.9 a) shows that there is no clear dependence between this
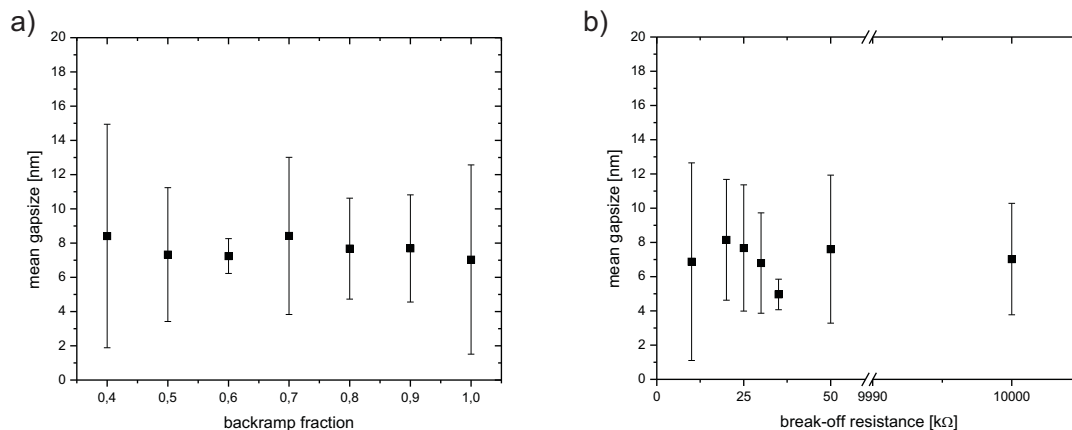
Figure 5.9: *a) Dependence of the mean gap size from the factor to which the voltage is ramped back after a cycle. b) Dependence of the mean gap size from the terminating resistance. The figures are adapted from [40].*

fraction and the resulting gap size. In the last test, the end value of the resistance at which the voltage ramp is interrupted and set to 0 V, is investigated. The electromigration stops not immediately after the voltage is taken away. The atoms with high energies are still moving and the gap is formed. Figure 5.9 b) illustrates the dependence of the break-off resistance and the gap size. The best results are obtained at 35 kΩ.

Electromigration in a dilution refrigerator at 4.2 K

Single-molecule measurements are performed at very low temperatures. Therefore the measurements and the electromigration have to be done in a dilution refrigerator. Here, in total 78 nanoconstrictions are migrated and from 28 of them, the gap sizes are measured. The breaking behavior of the nanoconstrictions at 4.2 K is different from that at 15 K. Figure 5.10 a) shows the electromigration from 11 structures where the voltage is ramped up without loops. The initial resistance of the nanoconstrictions was between 70 and 140 Ω. The termination voltage is set to 2 V and the termination resistance is set to 20 or 50 kΩ. The breaking voltage of every constriction is different, but most of the gaps are smaller than 5 nm and suitable for single-molecule measurements. On the right side of figure 5.10 an electromigration performed with the active feedback loop is shown. Here only 5 ramps are needed to migrate the nanoconstriction. At 15 K normally more than 20 ramps are necessary for the EM (see figure 5.5 b)). The inset shows the behavior of the resistance for the first 4 ramps.

The initial resistance of the investigated nanoconstrictions is shown in figure 5.11 a). The initial resistance of the constrictions is between 50 and 700 Ω. Most of the structures have an initial resistance of about 100 Ω. The gap sizes of 28 structures are measured
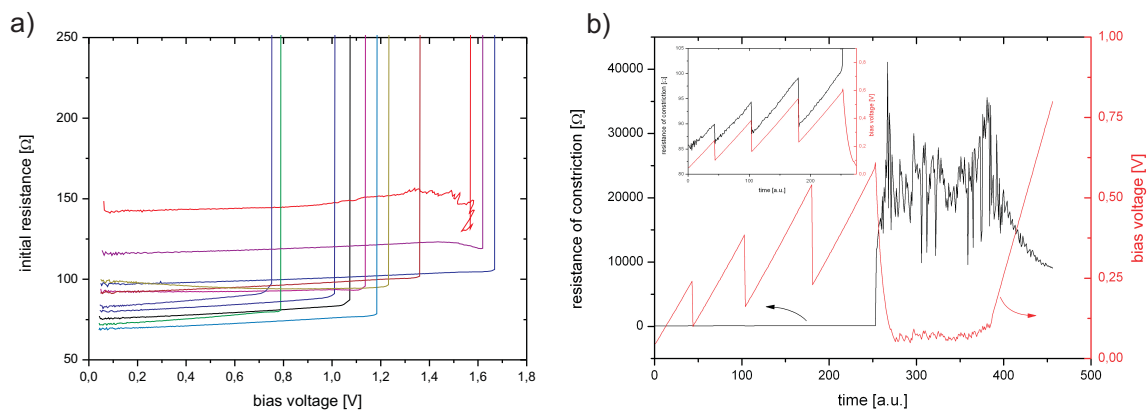
Figure 5.10: *a) Electromigration of 11 nanoconstrictios by ramping up the bias voltage. b) Electromigration on a nanoconstriction with the active feedback loop like described above. The inset shows low ohmic behavior of the resistance and the voltage for the first 4 ramps in detail. The resistance (black) changes at the end of the 4th ramp to 20 kΩ. The voltage (red) is ramped up to a maximum voltage of 0.8 V.*
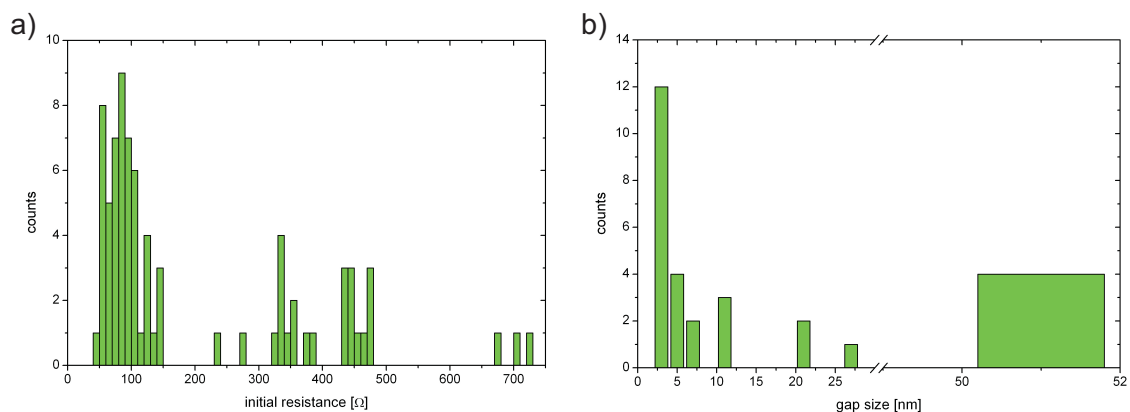

Figure 5.11: *a) Histogram of the distribution of the initial resistance of 78 nanoconstrictions electromigrated in the dilution fridge. b) Histogram of the gap sizes of 28 nanoconstrictions after the electromigration measured by SEM. The column at 3 nm shows the not resolvable gaps, the column at 50 nm indicates the constrictions with bigger gaps melted during the EM process.*

like described above by SEM and the results are shown in figure 5.11 b). The column at a gap size of 3 nm indicates all gaps that are not resolvable by SEM measurement. Most of the gaps were smaller than 10 nm and suitable for single molecule measurements. The column at 50 nm shows the gaps which were bigger than 50 nm. For these structures the EM process was not successful and the nanoconstrictions are melted.

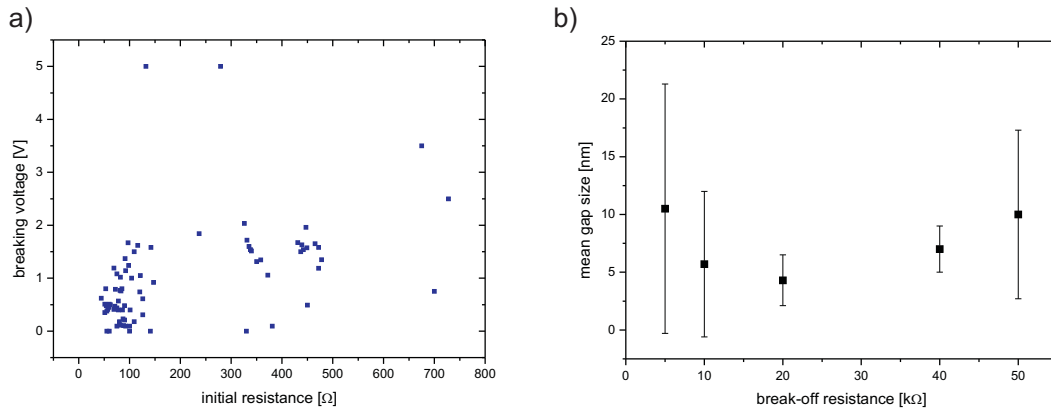In the dilution fridge the following parameters of the electromigration are varied: the

Figure 5.12: *a) Dependence of the breaking voltage on the initial resistance of the nanocon-strictions. For smaller initial resistance in the most cases a smaller breaking voltage is needed. b) Dependence of the mean gap size from the break-off resistance. The smallest gaps are obtained with a break-off resistance of 20 kΩ.*

size of the reference resistor, the maximum resistance and the feedback mechanism itself, between one ramp or several ramps. The initial resistance, the breaking voltage, the breaking resistance and the gap size are investigated to find the best parameters for the EM. The dependence of the breaking voltage from the initial resistance is shown in figure 5.12 a). For lower initial resistances the breaking voltage of the nanoconstriction is also lower. This is consistent with the observations described above and signifies a working EM process. Figure 5.12 b) shows the dependence of the mean gap size from the break-off resistance for the electromigration process. The smallest mean gap size with a very low standard deviation is at 20 kΩ. This value is smaller than for the electromigration at 15 K.

The reference resistor is varied between 10 Ω, 100 Ω, 333 Ω and 472 Ω. The structures with a high initial resistance are migrated with a 10 Ω reference resistor in series to keep the total resistance of the circuit small. The breaking voltage of these structures is mostly above 1 V. The high breaking voltage is due to the high initial resistance, the series resistance is not important in this case. Further some of the constrictions with initial resistance of around 100 Ω are migrated with the 10 Ω series resistor. Here, the breaking voltage is very small and in all cases under 0.40 V, but more than 10 ramps are needed for the EM process and the gap sizes showed no peculiarities. For the other three values of the reference resistor the behavior of the electromigration is similar. The breaking voltage shows no dependence from the series resistor, only from the initial resistance of the nanoconstrictions. For most of the migrations between 3 and 6 voltage ramps are needed. For the electromigration with only one ramp, like shown in figure 5.10 a), higher breaking voltages are obtained than for the EM with more ramps. However, the gap sizes are smaller with one voltage ramp than with more voltage ramps.

One problem appeared for some of the structures during the electromigration. For a not working electromigration (gap sizes ≥ 20 nm), it came sometimes to a massive heating of the sample or a complete destruction of the nanoconstriction. Thereby the thin gate oxide is destroyed and the gate is leaking after the EM. Then it is not possible for all constrictions structured on this local gate to apply a gate voltage. To avoid this problem in future it is advised to make the complete EM not before the measurements, but to migrate one structure and the next after the measurements of the first are finished.

The electromigration at low temperatures shows a certain behavior visible in the SEM
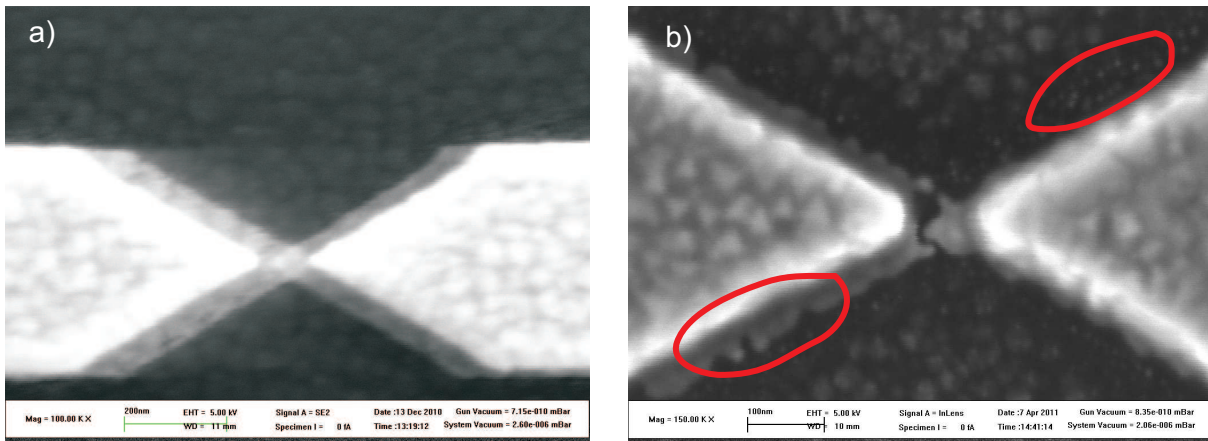
Figure 5.13: *a) Nanoconstriction before the electromigration process. The uniformity of the shadow evaporated structure is visible. b) Nanoconstriction after the electromigration at 4.2 K. In the red circle on the left side the formation of harbors on the edges of the shadow evaporated structure is visible. The red circle on the right side shows gold grains formed due to the material transport by the EM.*

pictures. Figure 5.13 shows a shadow evaporated nanoconstriction before and after electromigration. The shadow is very uniform in figure 5.13 a). The mass transport is visible in image 5.13 b) which is taken after the EM. In the red circle on the left side it is visible that a harbor like structure is formed on the edge of the shadow. The gap itself shows the same structure. In the red circle on the right side small, a few nm sized gold grains are visible. The thin shadow has vanished and only a few, very small, round grains remained. This phenomenon is observed on all structures electromigrated at low temperatures.

Chapter 6

Measurement of single molecules

The interpretation of electrical measurements on three-terminal devices with molecules applied, is always challenging. For nanogaps formed by electromigration it is further complicated by to the possible formation of small gold grains in the gap (see chapter 5). These gold grains can show conduction characteristics similar to the signals expected from the molecules.

Furthermore it is not possible to characterise first the gaps after electromigration without molecules applied. The sample has to be cooled down to base temperature and than to be measured. For the application of the molecules the sample need to be warmed up to room temperature and afterwards it has to be cooled down again. This reasonable sounding procedure is not possible for the electromigrated samples, because the thin gold forming the electrodes is not stable at room temperature and the gap size and its topology change at temperatures above 200 K [4]. This chapter shows a way to perform consistency measurements on well characterised C_{60} buckyballs.

First the measurement set-ups and the measurement technique is introduced. Followed by a section about these measurements on C_{60} buckyballs. Their aim is to get informations about the reliability of the nanogaps created by electromigration. These tests are performed at a cryogenic probe station at 15 K. First the nanogaps were characterised directly after the electromigration to get informations about possible gold grains in the gaps after the electromigration process (EM). Then the solvent toluene without molecules is applied to the structures to check its possible influence onto the measurements. At last the molecules are brought onto the nanogaps and measured at 15 K. Further measurements of C_{60} molecules are performed in a dilution refrigerator at base temperature. The next section describes the distinction between single-molecules and post electromigration gold grains in the nanogap. Finally the measurements of pentaphenylene molecules with different chain length are described and discussed.

6.1   Measurement set-up

The measurements are performed with low frequency lock-in technique. Lock-in amplifiers can be used to measure the differential conductance $\partial I/\partial V$ [63]. The simplified measurement circuit is illustrated in figure 6.1.

The single-molecule transistor is depicted in the middle of the circuit as the wiring sym-
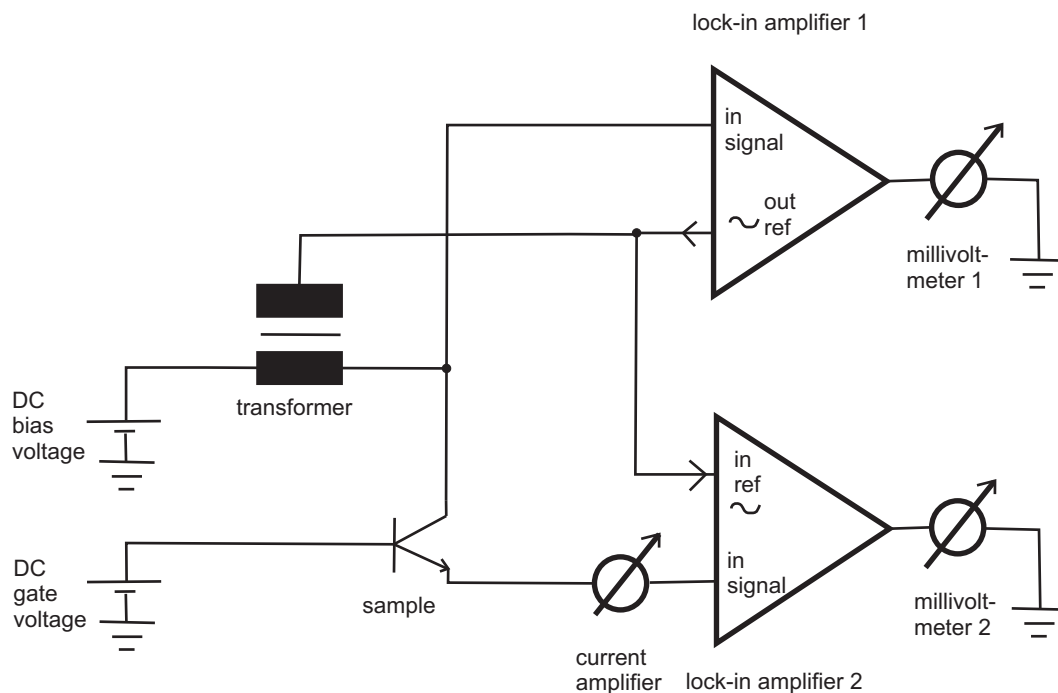

Figure 6.1: *Measurement circuit diagram: The sample is shown with the symbol of a transistor. The DC voltage for bias and gate is applied by a PCI- card. The AC voltage is generated by one of the lock-in amplifier and added to the DC signal by a transformer. To simplify the circuit, the voltage dividers and the pi-filters are not drawn.*

bol of a transistor. A DC voltage is applied through a 16-bit analog voltage output card[1] from the computer. The AC voltage signal is generated by one of the lock-in amplifier and modulated onto the DC voltage by a transformer. This signal serves also as reference signal for the second lock-in amplifier. The voltage drop over the sample is read-out by the first lock-in amplifier, which in turn is read-out by a millivoltmeter. The current flowing through the transistor is measured by a current amplifier[2]. The signal of this amplifier is transfered to the second lock-in amplifier and also read-out with a millivoltmeter. Various voltage dividers and pi-filters are implemented into the circuit to adjust the voltage and to reduce the noise on the signals (*not shown in figure 6.1*).

---

[1]Adlink PCI-card 6208V, 16-bit, 8 analogue output channels, $\pm$ 10 V from Agilent
[2]Ithaco 1211 current pre-amplifier

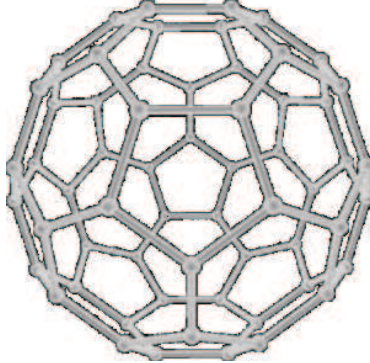## 6.2   Measurements of C_{60} molecules

Figure 6.2: *Chemical structure of a C_{60} buckyball molecule.*

In the last years various experiments were performed on C_{60} based single-molecule transistors (SMT). The Kondo effect in C_{60} SMTs was shown by Roch and Yu in 2008 [28], [33]. Various other tunnel effects on SMTs with C_{60} have also been reported. We aim here to compare to this literature to confirm the presence of C_{60} in the gap. After formation of the nanogap by electromigration, it is possible that gold grains, instead of a single-molecule, are bound between the electrodes of the transistor and are responsible for the tunneling current. To get a feeling of the difference of tunneling through gold grains or clusters and C_{60} molecules, consistency measurements at 15 K were performed on a cryogenic cold probe station. This measurement set-up allows the measurement of a large number of samples without warming-up the sample chamber. The measurements at low temperatures (below 4 K) are performed in a dilution refrigerator. There, the number of nanoconstrictions is limited by wiring restriction to 14. The behavior of the C_{60} SMTs in electric and magnetic fields is investigated for several samples at around 100 mK.

6.2.1   Consistency measurements at 15 K

Many of the consistency measurements were performed by Andreas Kempf and a more detailed discussions about the set-up are reported in his bachelor thesis [64]. Here, the focus lies on the summary and interpretation of his results and the comparison of these results to further measurements performed in a dilution refrigerator at low temperatures. The temperature during the measurements is kept between 15 and 20 K by regulation of the liquid helium flow through the cooling system of the probe station. The probe station is used because a big number of nanoconstrictons can be characterised without a sample change. Further a sample change can be done in a few hours. For the consistency measurements one sample with 700 structures is used. The electromigration is performed and directly afterwards the nanoconstrictions are characterised by sweeps of the bias and gate voltage. The differential conductance is measured with the set-up described in section

6.1. To test for reproducibility all voltage sweeps are repeated three or four times. The single-molecules are available in crystal form. For their application in transistors, first they are diluted in a solvent and than pipetted over the nanoconstrictions (see section 4.3). For the consistency measurements first the nanoconstrictions without molecules are investigated. Than the pure solvent is applied to the sample and further structures are measured. At last the solution of single-molecules and solvent is pipetted onto the sample and more nanoconstrictions are characterised.

6.2.1.1   Measurement of the tunneling behavior without molecules or solvent

The tunneling behavior of 153 nanoconstrictions, after electromigration and without application of single-molecules or solvent, is investigated. Due to a very small overlap after the shadow evaporation, the electromigration worked only for 41 % of the structures. The other nanoconstrictions were not connected and had already a gap. During the measurements most of the constrictions showed resistances above 10 MΩ (resistances higher than 10 MΩ are not measurable the used set-up, see [64]). Only three of the 153 measured structures showed measureable tunnel currents. Two of them indicate an electromigration process due to the measurements, the third structure shows coulomb peaks in the gate sweeps. In figure 6.3 a) four bias voltage sweeps vs. differential conductance are plotted. During the second sweep the differential conductance increases significantly and stays stable for the next sweeps. This behavior can be explained through a change of the size of the nanogap during the measurement. Here, it is possible that a gold grain is absorbed by an electrode due to the change of the voltage from negative to positive values. The bigger gap shows now a different, but stable tunnel behavior. Further, gold grains or clusters can reorganzied due to the relativley high measurement temperature or the direction of the applied DC current. The gate voltage sweeps in figure 6.3 b) show a weak, almost linear dependence on the differential conductance signifying an empty gap without or only with weak coupled gold grains.

  The third structure has different characteristics (see figure 6.4). The first bias voltage sweep shows a symmetric curve around zero voltage and therefore direct tunneling. In figure 6.4 it is obvious that for the following three sweeps the signal is unstable and changes for each sweep. The rise of the signal for negative bias voltages is reproducible, but the position of the peaks is different. That fact concludes an instable behavior of the gap. The gate voltage sweeps indicate clearly visible coulomb peaks. The first sweep in figure 6.4 b) shows four, the next sweeps only two minimum. The shift of the big minimum in the second sweep can be explained by charge transfer as a result of opposite sweep direction. The Coulomb peaks (minimum) signify that one or more gold grains are situated in the gap and the molecular states are excited by the gate voltage sweeps.
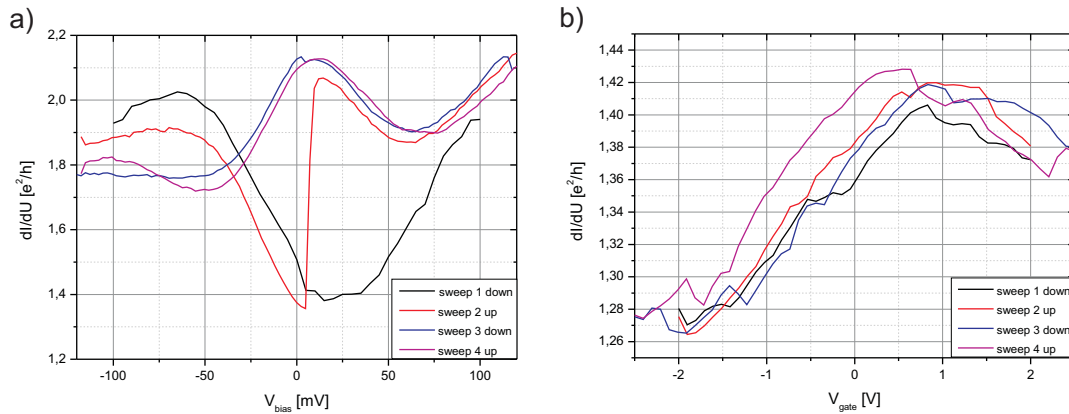
Figure 6.3: *a) Bias voltage sweeps: During the second sweep an electromigration process occurs. After the EM a stable behavior is obtained. b) Gate voltage sweeps of the same structure: The sweeps are reproducible and show no specific behavior or peaks. Similar curves are measured very often for further structures.*
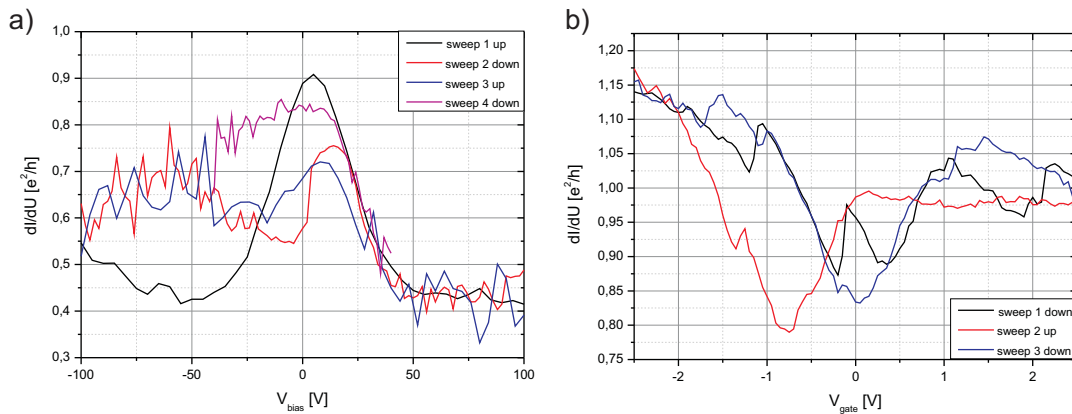

Figure 6.4: *a) Bias voltage sweeps: The first measurement shows a stable signal, the others a very unstable behavior. b) Gate voltage sweeps of the same structure: The curves show minimum in the differential conductance (Coulomb peaks). The shift between the minimum is a hysteresis caused by charging effects of the gate due to the sweep direction.*

6.2.1.2   Measurement of the tunneling behavior with solvent

The solvent toluene is applied to the sample and afterwards another 179 nanoconstrictions are migrated and characterised. Here, the electromigration of 48 % of the structures was successful. Again, only three of the nanoconstrictions had measurable signals.

The first constriction (see figure 6.5 a)) has similar values for the differential conductivity as illustrated before in figure 6.3 b). The curves are very noisy and show no clear peaks. Probably, this behavior indicates also a weakly coupled gold grain. The bias voltage
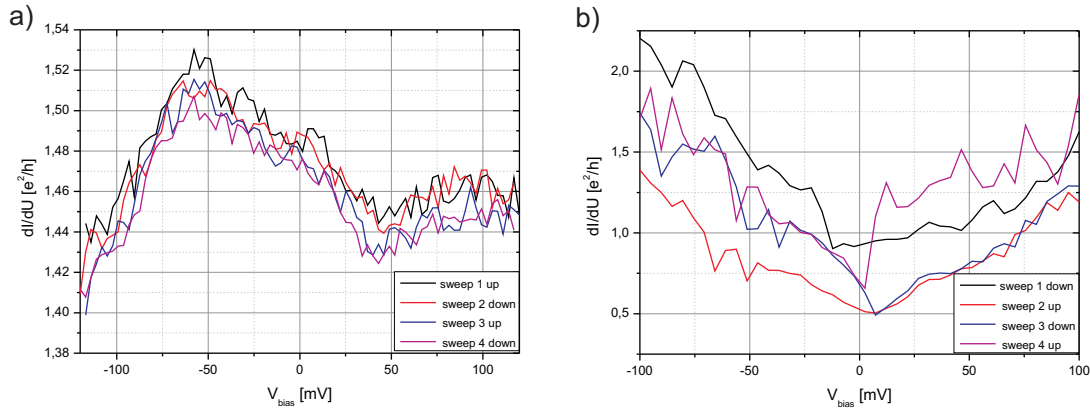
Figure 6.5: *a) and b) Bias voltage sweeps of two different structures: Both show a noisy signal without characteristic peaks. The values of the differential conductance are comparable to figure 6.3 a).*

sweeps of the another structure are shown in figure 6.5 b). A minimum around 0 V is visible. The values of the differential conductance are comparable to the bias voltage sweeps in figure 6.3 a). Therefore it is likely that here also gold grains are bound in the gap and responsible for the tunnel current. The third transistor (figure 6.6 a)) has the
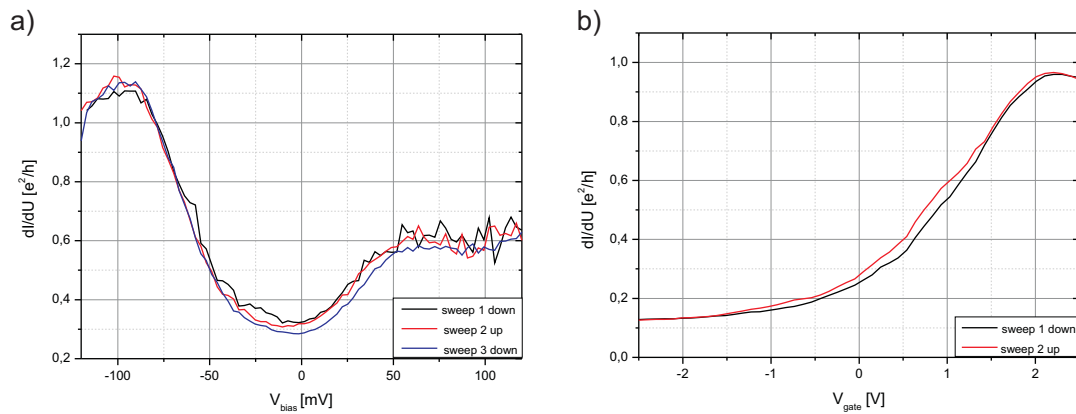
Figure 6.6: *a) Bias voltage sweeps: A minimum in the differential conductance at 0 mV is visible. The measured curves reproduce well. b) Gate voltage sweeps of the same structure: The slope of the curves is representative for the measurements in this section.*

lowest values for the differential conductance again around a bias voltage of 0 V. The curves for the sweeps reproduce well. The nearly constant signal for bias voltages above 50 mV indicates direct tunneling. The gate voltage sweeps (figure 6.6 b)) show a typical characteristics measured for most of the transistors in this section. The linear decrease of the signal without peaks or other features is also reported in [17].

It was not possible to find a difference in the measured characteristics between transistors with and without solvent. Thus it can be concluded that the solvent molecule do not bind into the gaps and influence the measurement.

6.2.1.3   Measurement of the tunneling behavior with molecules and solvent

After the application of the C_{60} molecules solved in toluene, 266 nanoconstrictions were characterised. Here, also only for 42 % of the structures the electromigration worked well. However, seven transistors showed a measureable differential resistance between 10 and 100 $k\Omega$.

The results of the measurements with molecules can be classified into two characteristics
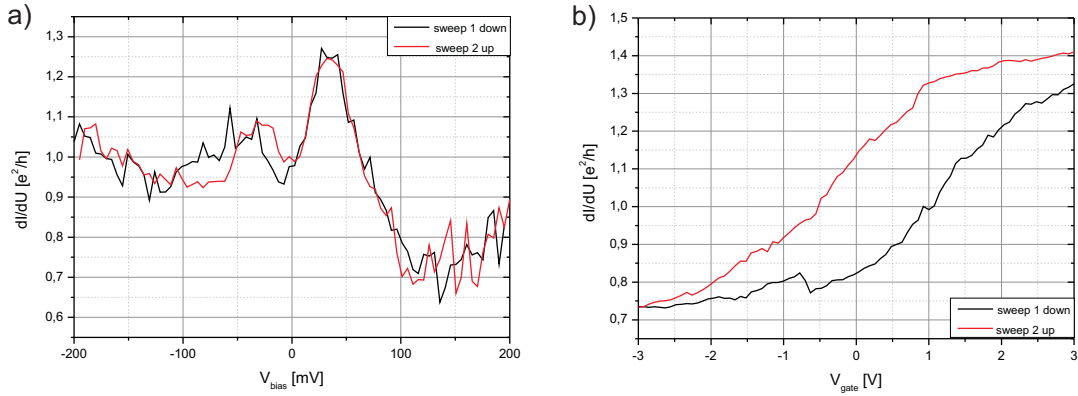
Figure 6.7: *a) Bias voltage sweeps: A peak in the differential conductance at 30 mV bias voltage is visible. The curve is very noisy. b) Gate voltage sweeps of another nanoconstriction: A hysteresis in the gate voltage sweep of more than 1 V is shown indicating problems with the gate oxide.*

comparing the values for the differential conductance and the peak positions. Figure 6.7 shows a typical curve measured for three different structures. The values of $\partial I/\partial V$ are between 0.60 and 1.30 $\frac{e^2}{h}$. The bias voltage sweeps are very noisy a sign for an unstable behavior of the nanogap. The gate voltage sweeps do not indicate charging effects. The characteristics of these samples is comparable to figure 6.4 and also to the bias voltage sweep of figure 6.6. In these nanoconstrictions the behavior is assumed as electron tunneling through gold clusters in the nanogaps. The same assumption can be done here. Mainly the gate voltage sweeps show no clear peaks. The hysteresis between the two sweeps with opposite sweep direction in figure 6.7 indicate an unstable gate. This hysteresis is observed for most of the structures on the complete sample and suggests to problems with charging.

Further nanoconstrictions show bias voltage sweeps with a clear maximum. Figure 6.8 shows two of these curves. Here, the differential conductance is between 0.40 and 1.0 $\frac{e^2}{h}$
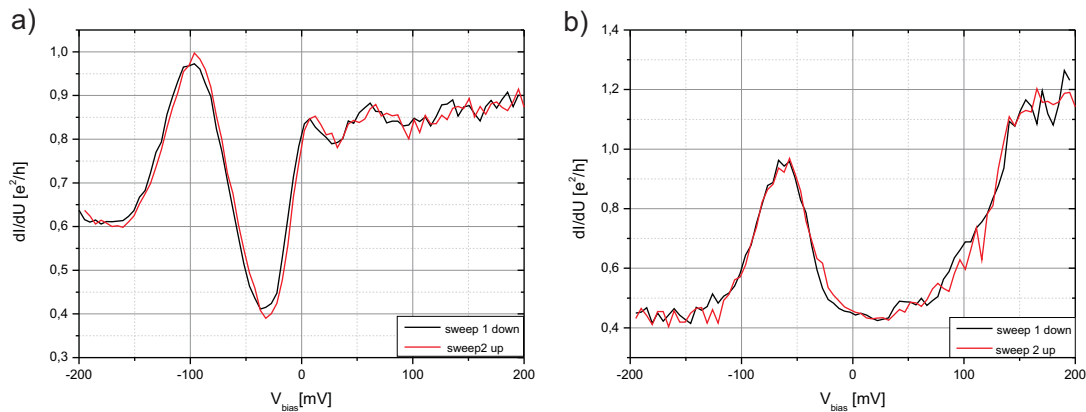
Figure 6.8: *a) and b) Bias voltage sweeps of two different nanogaps: Both samples show a characteristic slope with peaks. The gate voltage sweeps for these samples showed no interesting features.*

and therefore lower than for the structures showed above. However, the gate sweeps gave similar behavior as illustrated in figure 6.7 b). The characteristics of these nanogaps can be compared to the structures without single-molecules in figure 6.4 and 6.6.

Another nanoconstriction shows a double peak around 0 V in the bias sweep (see figure
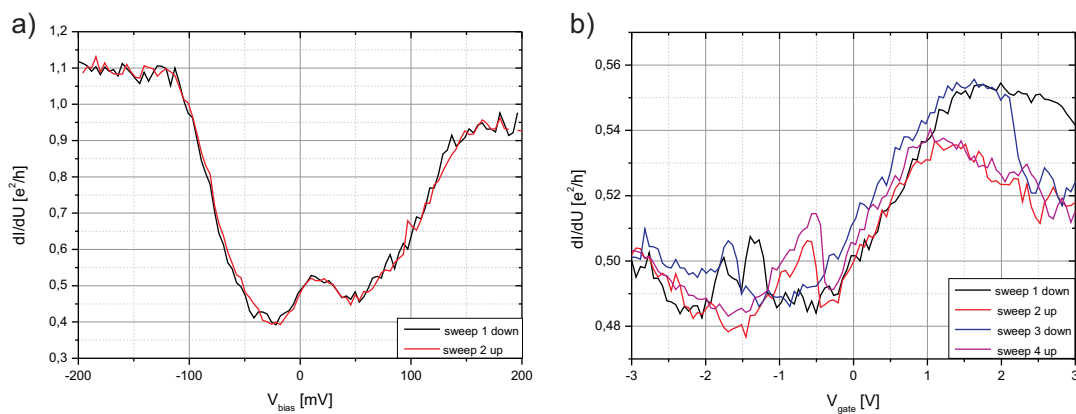
Figure 6.9: *a) Bias voltage sweeps: A reproducible peak around 0 mV is visible. b) Gate voltage sweeps of the same nanogap: The sweeps show features dependent on the sweep direction.*

6.9). The values of the differential conductance are similar to the graphs in figure 6.8. In the gate voltage sweep is an unstable behavior visible. It has to be mentioned that the two sweeps done in the same sweep direction correspond to each other good. It is possible that here a weak coupled C_{60} molecule is measured.

For high quality measurements the temperature has to be in the mK-range. There-fore further measurements are performed in an dilution refrigerator. This set-up gives in addition the possibility to apply a magnetic field up to $\pm$ 11 T.

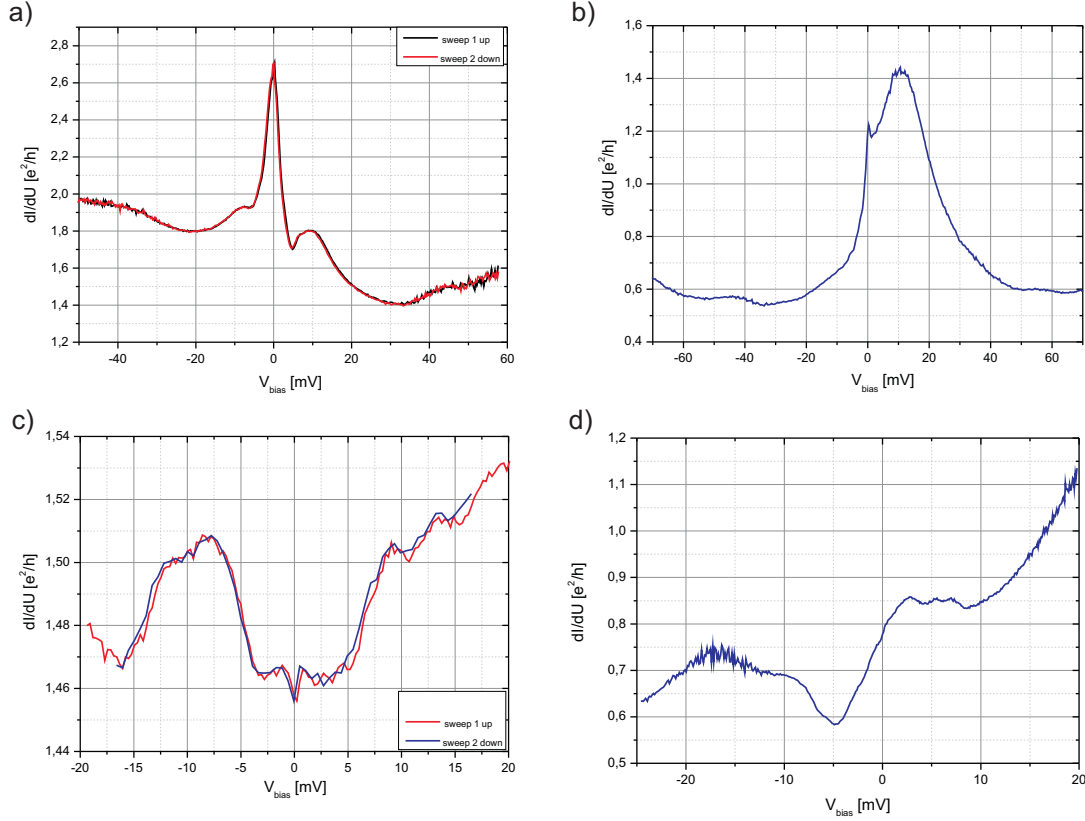## 6.2.2   Conductivity at low temperatures

Figure 6.10: *Characterisation of nanogaps with C_{60} molecules. The differential conductance is plotted as a function of the bias voltage in the range of interest. a) Typical signal obtained for 9 nanogaps. A maximum peak at a bias voltage of 0 V is visible. The differential conductances of these peaks are between 2.0 and 3.2 $\frac{e^2}{h}$. Often a smaller shoulder like peak near the main peak is visible. b) Signal obtained for 7 nanoconstrictions. Here the maximum peak is not at 0 V. The maximum values of these peaks are normally between 0.9 and 1.5 $\frac{e^2}{h}$. c) Signal sequence of further constrictions. The signal changes reproducible in a small range of the differential conductance and shows no clear peaks. d) Ascending slope investigated for 5 nanogaps. The signal shows a minimum and a maximum with the maximal gradient at a bias voltage of 0 V.*

Various samples with C_{60} molecules were investigated at base temperature in a dilution refrigerator. The molecules are applied to the structures as described in section 4.3. After the application of the molecules the samples are mounted on the sample holders on the inset of the cryostat. The inset was transferred into the cryostat as fast as possible and immediately cooled down. The electromigration was performed at 4.2 or 1.2 K. After electromigration, the cryostat was cooled down to base temperature. The measurements were done with the circuit described in section 6.1.

First the differential conductance as a function of the bias voltage is measured. The results of all measured structures can be classified in 4 categories. These different signatures are shown in figure 6.10. The signal type shown in figure 6.10 a) is found for 9 structures. The differential conductance shows a maximum at a bias voltage of 0 V. These maximums have values between 2.0 and 3.2 $\frac{e^2}{h}$. Often a small shoulder of one side of the main peak is visible. In figure 6.10 b) a typical curve obtained for 7 structures is illustrated. These structures have there maximum peak at negative or positive bias voltages. The peak values are smaller, between 0.9 and 1.5 $\frac{e^2}{h}$. Figure 6.10 c) shows a completely different behavior. The curve shows no clear peaks and the differential conductance changes only in a very small range. These signatures are observed for 4 structures. In figure 6.10 d) another characteristics is illustrated. The curves have minimums and maximums. The maximal gradient of the differential conductance is at a bias voltage of 0 V. These signatures are seen at 5 nanoconstrictions.

The measurement results of some structures could not be classified in these 4 categories.
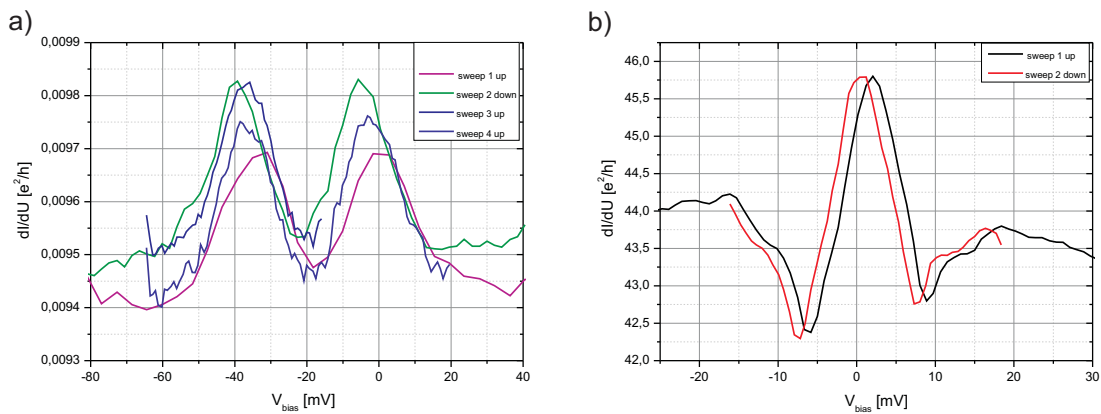

Figure 6.11: *The differential conductance plotted as a function of the bias voltage for two nanogaps. a) A few of the nanogaps showed values a few orders of magnitude lower. Here two peaks and a minimum at a bias voltage of 0 V is visible. b) Also significant higher values for the conductivity are measured. Here a maximum peak at 45,5 $\frac{e^2}{h}$ is shown. This value is more than one order of magnitude higher than the average of the measured signals.*

Some structures had values for the differential conductivity some orders of magnitude lower or higher than shown in figure 6.10. Figure 6.11 shows two typical examples. On the left side a curve with very low conductance is illustrated. The right curve has a very high differential conductance. Similar curves are measured for a few other constrictions, but not often enough to consider the results for the classification in the categories.

For a more detailed characterisation of the nanogaps, gate voltage sweeps and magnetic field sweeps are performed for the gaps which showed a promising signature in the bias
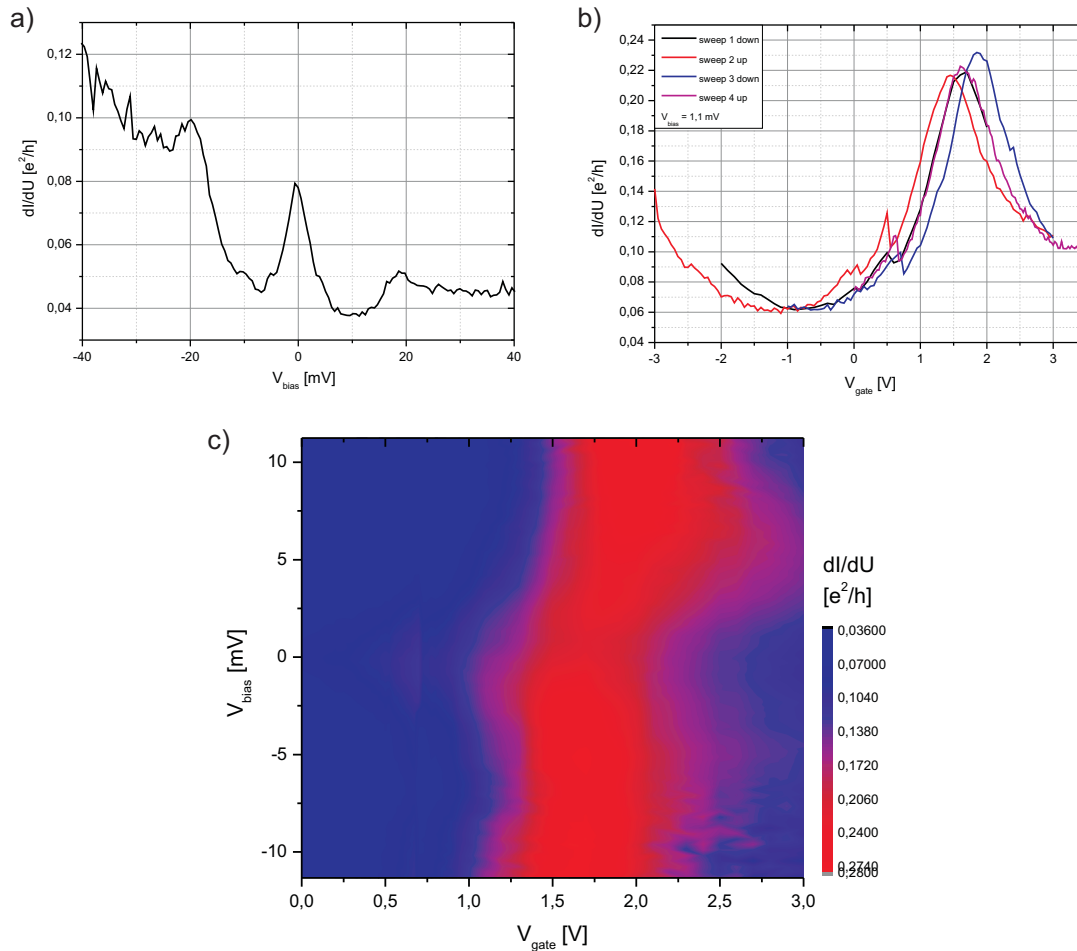
Figure 6.12: *a) Differential conductance plotted as a function of the bias voltage at a gate voltage of 0 V. A peak at a bias voltage of 0 V is visible. b) Differential conductance plotted as a function of the gate voltage by a fixed bias voltage of 1.1 mV. The peak is shifted to higher gate voltages. Further a small hysteresis depending on the sweep direction is visible. c) Stability diagram of the differential conductance: the bias voltage is plotted versus the gate voltage. The differential conductance has a maximum (red region) between 1.5 V and 2.0 V gate voltage.*

voltage sweeps. The left side of figure 6.12 shows the bias voltage sweep of a structure which falls outside the 4 categories above. On the right side the corresponding gate voltage sweeps done at 1.1 mV bias voltage are illustrated. The gate voltage sweeps show also a maximum but not at 0 V. The peak is shifted to values between 1.4 and 1.8 V. A hysteresis between the different sweeps is visible. Figure 6.12 c) shows the stability diagram of the differential conductance taken over the range of the bias voltage with the peak in its center. There are also the maximum values of the differential conductance around 1.7 V. There is no Coulomb diamond structure visible. The shift of the maximum

peak of the conductance in the gate sweeps can be caused by a leakage in the gate oxide. It was a problem for some structures that the gate oxide was destroyed by the heat impact during the electromigration.

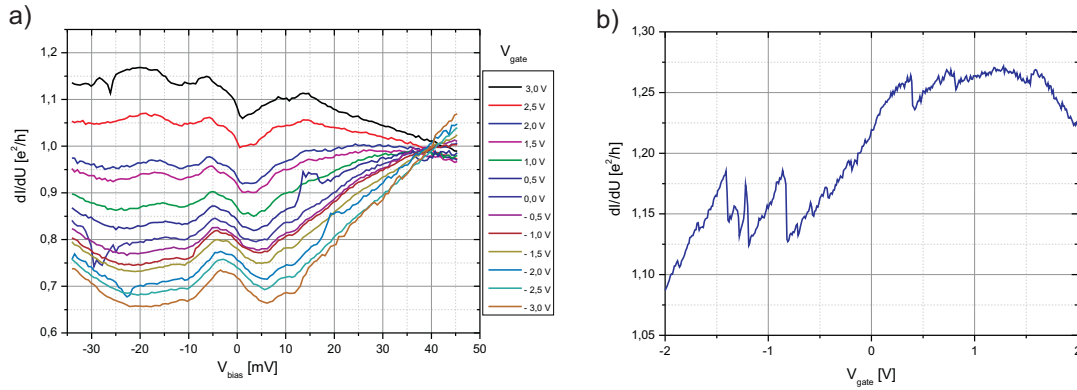Instabilities of the gate oxide can also be identified from the results shown in figure

Figure 6.13: *a) Differential conductance measured over a nanogap plotted as a function of the swept bias voltage. The different curves correspond to different applied gate voltages. Higher gate voltage shows a higher differential conductance. The signature of the curves depends not on the gate voltage. b) Differential conductance as a function of the gate voltage. The curve shows some jumps indicating instabilities of the gate electrode.*

6.13. This structure was on the same sample as the nanogap from figure 6.12. Figure 6.13 a) shows bias voltage sweeps at different gate voltages. The black curve at 3.0 V of gate voltage has the highest values in differential conductance, the brown curve at -3.0 V gate voltage has the lowest values in differential conductance. The signatures of the differential conductance do not change with the applied gate voltage. These curves let conclude that here the gate voltage add or remove energy of the molecule without effecting it. It is not clear why all the curves have the same value of the differential conductance at a bias voltage of 40 mV. The gate voltage sweep in figure 6.13 b) shows a constant value of differential conductance around 1.20 $\frac{e^2}{h}$ with some jumps. This is another indication for a not stable gate electrode.

Figure 6.14 shows the results of another structure from the same sample like above. Here the differential conductance shows no peaks but corresponds to the category in figure 6.10 d). The gate voltage sweeps in figure 6.14 b) show an unstable behavior with different peaks. The stability diagram in figure 6.14 c) shows again no Coulomb blockade. There are vertical lines with higher values of the differential conductance visible. These values correspond to the peaks in figure 6.14 b).

Figure 6.15 shows a second peak in the gate voltage sweep. This peak was not visible in the bias voltage sweep in figure 6.15 a). The second peak occurring in the gate dependence could be a sign for a Coulomb peak and therefore an excitation of the molecule.
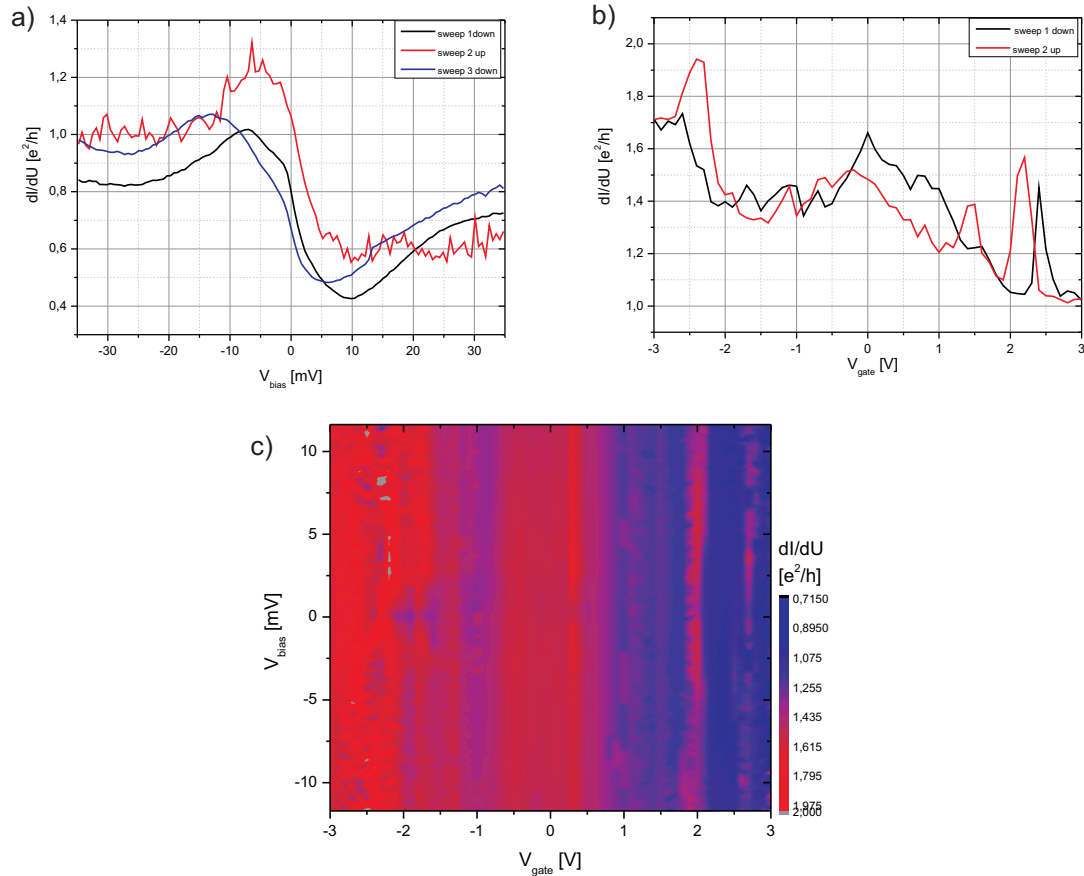
Figure 6.14: *a) Differential conductance as a function of the bias voltage. A ascending slope is visible. b) Differential conductance as a function of the gate voltage. Some peaks in the curve are visible. c) Stability diagramm of the differential conductance. The maximum values of the differential conductance are visible as vertical lines. These values correspond to the peaks in b).*

For some of the measured samples it was not possible to apply gate voltages due to defects in the gate oxide. Sometimes there was a conductive contact between the gate and the bias electrodes. This problem occurred after electromigration. For further measurements it is advised to make the complete electromigration not in the beginning of measurements. It would be better to electromigrate only one nanostructure and measure it immediately afterwards.
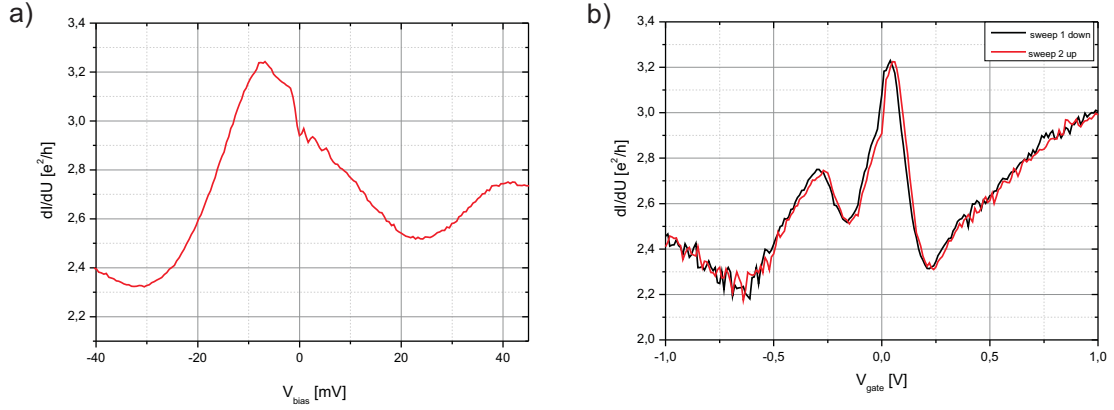
Figure 6.15: *a) Dependence on the differential conductance of bias voltage. b) Differential conductance as a function of gate voltage. A second peak indicating a Coulomb blockade is visible.*

6.2.3 Magnetic field measurements at low temperatures

The structures, which showed peaks in the bias voltage sweeps are further measured in magnetic fields. The setup has the possibility to apply magnetic fields from -11 to 11 T. Three structures showed a splitting of a peak in dependence of the magnetic field. The Zeeman splitting can be calculated with the following form of formula 2.8:

$$\Delta E_B = m_J \mu_e g_J B \tag{6.1}$$

with m_J the magnetic number $-|J|<m_J<|J|$, B is the magnetic field and μ_e is the Bohr magnetron. For the Landé-factor follows for spin 1/2 systems:

$$g = \frac{e\Delta V_{bias}}{\mu_e \Delta B} \tag{6.2}$$

The first results are presented in figure 6.16. The splitting occurs only for positive magnetic fields. The figures 6.16 a) and b) show color plots of the differentials conductivity in dependence on the magnetic field and the applied bias voltage. The plot on the left side shows the results for negative magnetic fields. There is no splitting in the conductivity visible. On the right side is the Zeeman splitting illustrated. The black line is drawn in the plot to make the splitting more clear and further indicates the values taken for the calculations of the Landé-factor with formula 6.2. These values and also results of the other two structures are noted in table 6.1. Figure 6.16 c) shows the dependence on the differential conductance of the applied bias voltage. A peak at zero bias indicates the Kondo effect. Here the peak is shifted to -3 mV, which is the offset of the DC-voltage channel used to apply the bias voltage (see figure 6.1). A second structure showed a splitting in positive and negative magnetic fields. Figure 6.17 illustrates the measurement results. In figure 6.17 a) are the bias voltage sweeps displayed. The differential conductivity shows
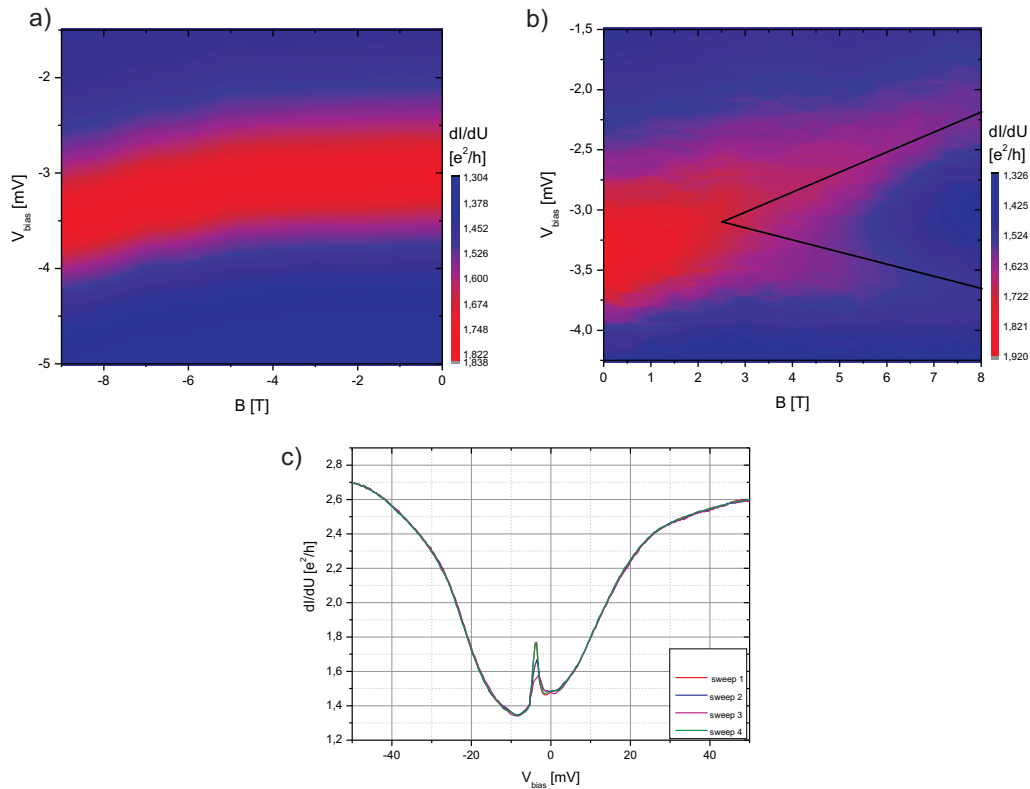
Figure 6.16: *a) Color plot of the differential conductance in dependence on the magnetic field and the bias voltage. There is no splitting for negative magnetic fields visible. b) Splitting of the differential conductance for positive magnetic fields. The black line indicates the values selected for the calculation of the Landé-factor. c) Differential conductance in dependence on the bias voltage at zero magnetic field.*

a peak at 0 V bias voltage. The sweeps are reproducible and show only one maximum. In the gate voltage sweeps were no peaks visible, therefor they are not illustrated. The other two pictures in figure 6.17 show color plots of the magnetic field dependence on the differential conductance. A high resolution plot for positive magnetic fields is shown in figure 6.17 b), the splitting of the differential conductivity is clearly visible. The color plot in figure 6.17 c) illustrates the splitting for positive and negative magnetic fields. The splitting is symmetric in 0 T. The bias voltage is again not exactly at 0 V. The reasons for this are explained above.

The third structure has very high values of the differential conductance. In figure 6.18 a) the differential conductance is plotted in dependence on the bias voltage. The magnetic field is varied for all curves in a range from 0 T to -1 T. The splitting of the peak at 0 V is visible and becomes more clear for higher magnetic fields. Figure 6.18 shows the color plot of the conductance in dependence on the bias voltage and for positive magnetic fields. The splitting for this structure occurs also for positive and negative magnetic fields.
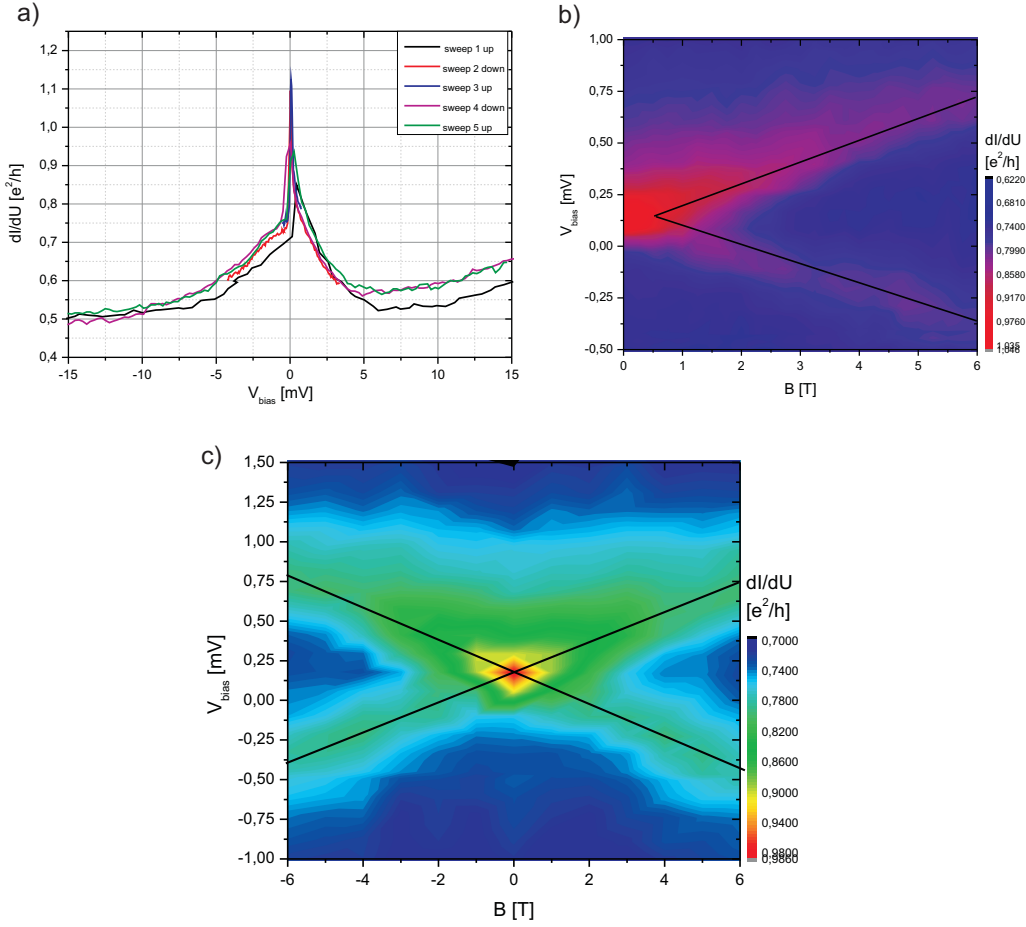
Figure 6.17: *a) Differential conductance in dependence on the bias voltage at zero magnetic field for the second structure. A Kondo peak at 0 V is visible. b) Color plot of the differential conductance in dependence on the magnetic field and the bias voltage. The splitting of the the peak in a) is visible. c) Color plot of the differential conductance for positive and negative magnetic fields. The splitting is symmetric.*

The splitting is higher than for structure one and two. However, the high values for the differential conductance are not understood.

The results of the three measured structures are presented in table 6.1. The Landé-factor is calculated with equation 6.2. The errors are given through the scale-reading precision. The Landé-factor of C_{60} is also measured by other groups [46] and [33] (see chapter 2.4). The values of the Landé-factor are very different from $g \approx 2$ reported in the literature. Therefor the Landé-factor of gold nanoparticles is reported to be 0.3 [65] and [66]. For the bulk material a g-factor of 2.1 is determined by electron spin resonance experiments [67]. The same value is reported by Houck et al. for electromigrated gold junctions [68].
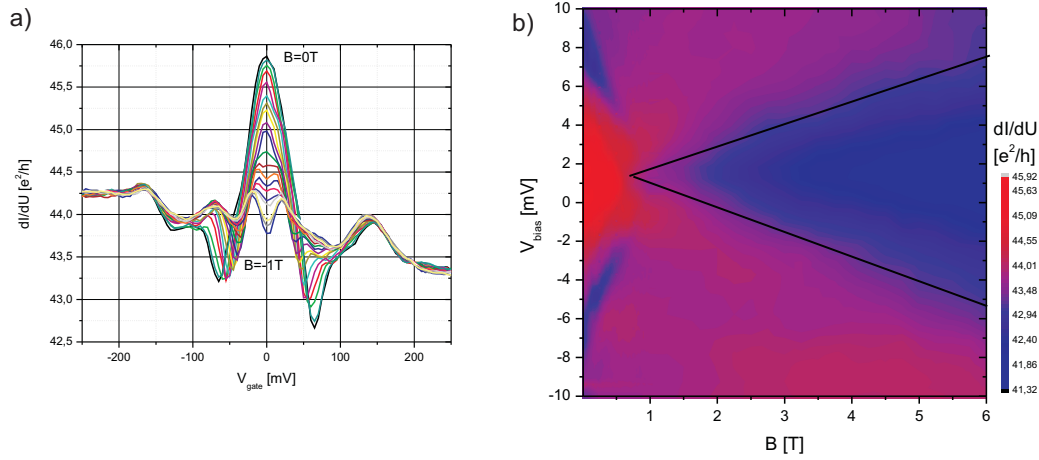
Figure 6.18: *a) Bias voltage sweeps of the differential conductance for different magnetic fields from 0 to -1 T in steps of 50 mT. The splitting starts at -650 mT (orange curve). b) Color plot of the differential conductance. The splitting starts for positive magnetic fields at 650 mT.*

Structure	ΔV_{bias} in mV	Δ B in T	g
figure 6.16	(1.5 ± 0.2)	(5.5 ± 0.2)	(4.7 ± 0.5)
figure 6.17	(1.2 ± 0.2)	(6.0 ± 0.2)	(3.5 ± 0.5)
figure 6.18	(12.7 ± 0.5)	(5.35 ± 0.2)	(41.0 ± 1.0)

Table 6.1: *Landé-factors for the three measured samples.*

6.3 Distinction between single-molecules and gold grains

The distinction between molecules and gold grains, after the electromigration in a nanogap, is important for the interpretation of the measurement results. Different groups showed that Coulomb blockade or Kondo effect could be measured on electromigrated nanogaps without the application of molecules [44], [68], [69]. Figure 6.19 shows the measurement results reported by van der Zant and Ward. For a clear distinction between gold or single-molecule various different measurements have to be performed. Chapter 2 describes the energy model of a single-molecule transistor. The size of the coulomb diamonds depends on the charging energy and on the level spacing of the molecule. For a gold grain the charging energy is the most important parameter and does not change with the number of electrons on the dot. The resulting picture of Coulomb diamonds is presented in figure 6.19 a) and b). The diamonds have the same size and do not change with the gate voltage. For a molecule the behavior shown in figure 6.19 c) is attended. The Coulomb diamonds have not the same size, there are less diamonds and the diamonds are less regular in size.
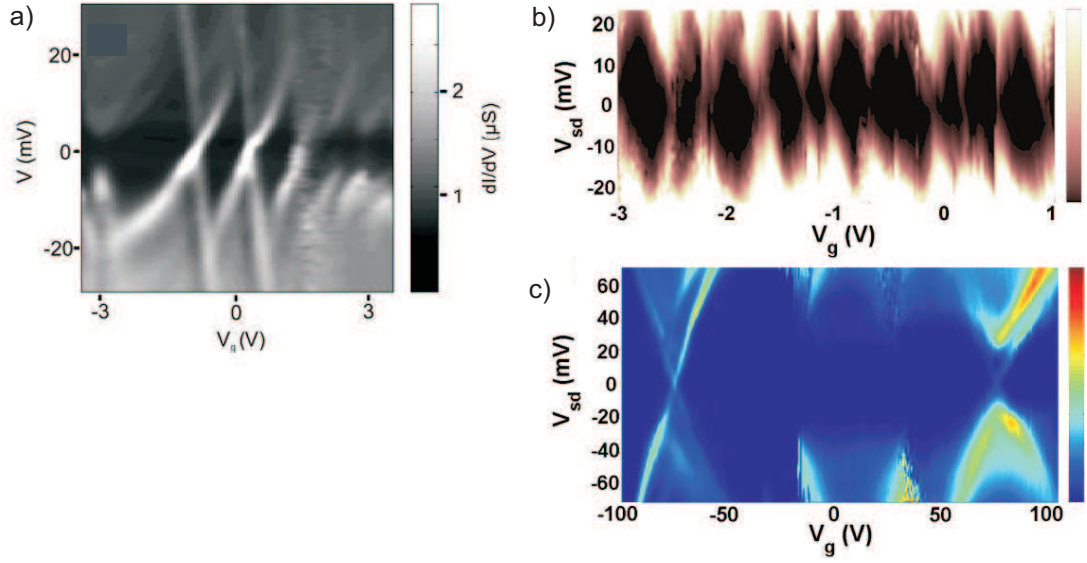
Figure 6.19: *a) Stability diagram of a gold particle from van der Zant et al. [44]. b) Stability diagram of a gold particle from Ward et al. [69]. c) Coulomb blockade of a C_{60} molecule also from Ward et al. [69].*

Another possibility for the distinction between molecule and gold grain is proposed by the group of van der Zant [70]. The gate coupling is different for molecule and gold grain. The gold grain is situated directly on the gate and has therefore a strong coupling. The molecule, applied before the electromigration, should lie somewhere between the electrodes and not directly on the gate. The coupling of the molecule is weak compared to the coupling of gold grains. For the comparison of the coupling the gate coupling factor β can be calculated out of the gate capacitance and the total capacitance of the device. Further it can be extracted out of the slopes of the coulomb diamond like described in chapter 2. The gate coupling factor can be determined with the following approximation:

$$\beta = \frac{C_g}{C} \approx \frac{1}{2}\frac{dV_{bias}}{dV_g} \tag{6.3}$$

with C_g is the gate capacitance and C is the total capacitance of the device. The approximation can be done in the case that $C_s \approx C_d$ and $C_g \ll C_s$, C_d. Van der Zant gives an value of $\beta > 0.2$ for a gold grain and smaller values than 0.2 for molecules [70].

The third way to proof the presence of a molecule in the SMT, is the behavior in magnetic fields. The Landé-factor is already known for much molecules and also for different metals. The g-factor for buckyball and gold are given in section 6.2.3. In the case of this thesis it seems to be the best way for the distinction between C_{60} and gold grains.

Unfortunately correspond the measured g-values not to the known values. The other two methods are also difficult to apply due to the problems with leakage currents in the gate electrode.

6.4 Measurements of short chain molecules

The short chain pentaphenylene molecules (molecule 1) are measured in the dilution cryostat at base temperature. The molecular structure of these molecules is shown in figure 6.20. The chain length of the molecules is 3.4 nm. This value is around three times higher than the size of the C_{60} fullerene molecules. The pentaphenylenes have thiol end groups which should assure the binding to the gold electrodes.
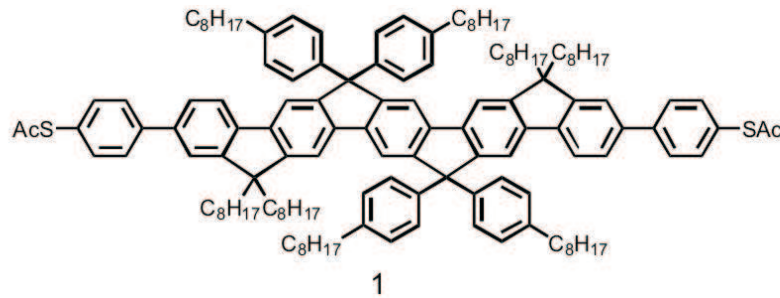

Figure 6.20: *Chemical structure of the short chain pentaphenylene molecules, with courtesy of Prof. Dr. Klaus Muellen, MPI Mainz.*

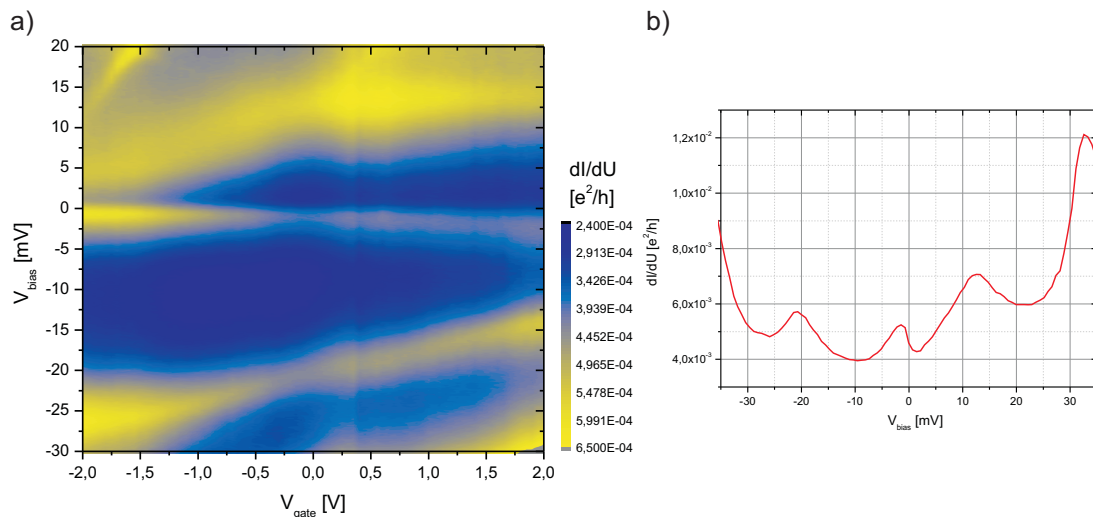### 6.4.1 Bias voltage and gate voltage measurements

Figure 6.21: *a) Two dimensional color plot of the differential conductance in dependence on the bias and gate voltage. There is no clear structure in the plot visible. b) Corresponding bias voltage sweep: different peaks are identifiable.*

In total 25 structures with the short chain pentaphenylene molecules are measured. The curves of 5 nanogaps showed a peak structure in the differential conductance in

dependence on the bias voltage. For these gaps also gate voltage measurements are performed. The results are shown in figures 6.21 to 6.25. The first two structures in figures 6.21 and 6.22 show further a splitting of the differential conductivity in dependence on the applied magnetic field. These results are presented in the next subsection in the figures 6.27 and 6.28. The differential conductivity of the first structure in figure 6.21 is one order of magnitude lower than for the other nanogaps. In the color plot on the left side a change of the conductivity depending on gate and bias voltage is visible. The interpretation of this result is difficult, thus there is no Coulomb blockade structure identifiable. The bias voltage sweep in figure 6.21 b) shows peaks at different values. This behavior was observed only for this gap.

The next structure illustrated in figure 6.22 shows a big peak at a differential con-
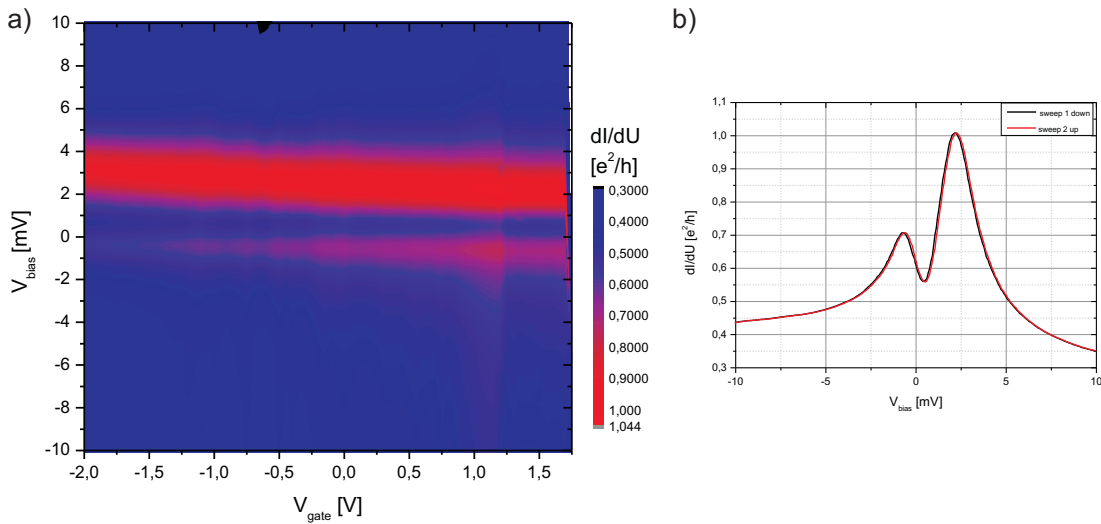

Figure 6.22: *a) Stability diagram of the differential conductance in dependence on the gate and bias voltage applied to the nanostructure. The small peak from b) vanishes for gate voltages lower than -1.5 V. b) Corresponding bias voltage sweep to the diagram on the left side.*

ductance of 1.0 $\frac{e^2}{h}$ at a bias voltage of 2 mV and a smaller peak at -0.5 mV. On the left side of the figure a color map of the differential conductance in dependence on the bias and the gate voltage is plotted. The small peak of the differential conductance vanishes at negative gate voltages higher than -1.5 V. Here again is no indication of a Coulomb blockade structure is possible. The values and the form of the differential conductance are comparable to type b) in figure 6.10.

The following two structures show similar behavior (see figures 6.23 and 6.24). The maximum of the differential conductance is for both at 0 V bias voltage and has a value at around 3 $\frac{e^2}{h}$. Further show the color plots of the differential conductance as a function of bias and gate voltage a coulomb blockade like structure. The color map in figure 6.23
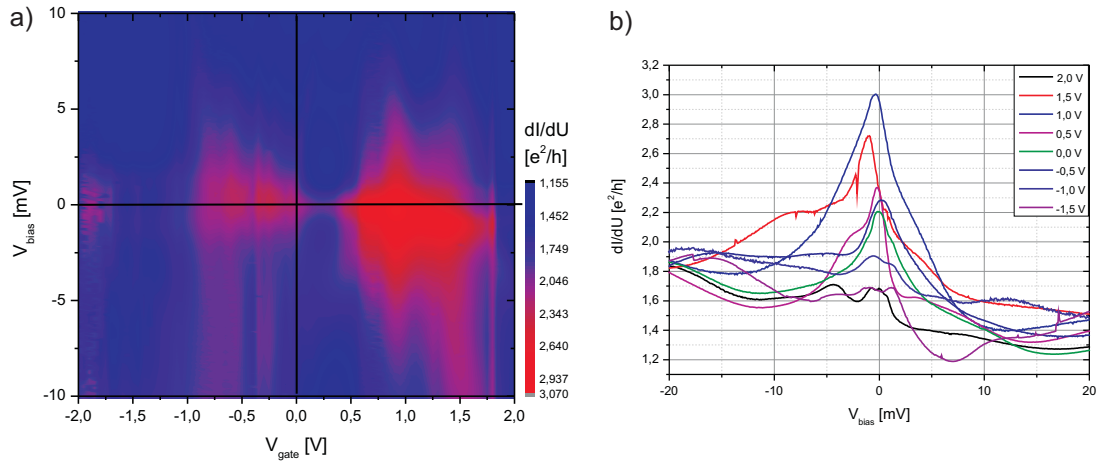
Figure 6.23: *a) Stability diagram of the differential conductance: two Coulomb diamond like structures are visible. The diamond for negative gate voltages is not so clear visible like for positive gate voltages. b) Bias voltage sweeps for different applied gate voltages. The differential conductance of the molecule depends strongly on the applied energy.*

a) indicates two Coulomb diamonds, one at negative gate voltages and a more clear diamond structure at positive gate voltages. On the right side of the figure the conductance is plotted for bias voltage sweeps at different gate voltages.

The measurements of the nanogap shown in figure 6.24 are comparable to the results in figure 6.23. Here also a Coulomb diamond is visible, but only for positive gate voltages. The two stability diagrams are measured on different days. There is a change in the profile of the diamond which could be a reason of a temperature change in the cryostat. The temperature was not measurable at the set-up but was at base temperature of the dilution unit. An other reason could be a instability in the behavior of the nanogap. The bias voltage sweeps in figure 6.24 c) show the same result. The red and the black curve correspond to the left color map, the violet and the blue graphs are measured before the stability diagram on the right side. These two structures which showed Coulomb blockade could not be measured in magnetic fields due to a defect of the switch heater of the magnet.

Figure 6.25 shows the results of the last nanogap which showed a signature in the bias voltage sweep (see inset). The differential conductance shows four peaks in a range of 16 mV. The values of the conductance are in a range from 2.20 to 2.40 $\frac{e^2}{h}$ and therefore smaller than for the other structures described above. The gate voltage shows some jumps indicating a instability in the gate voltage. Here the gate electrode is not stable enough for correct measurements. Similar curves are already described above. With the methods described above in section 6.3 it can be concluded that the Coulomb blockade structures,
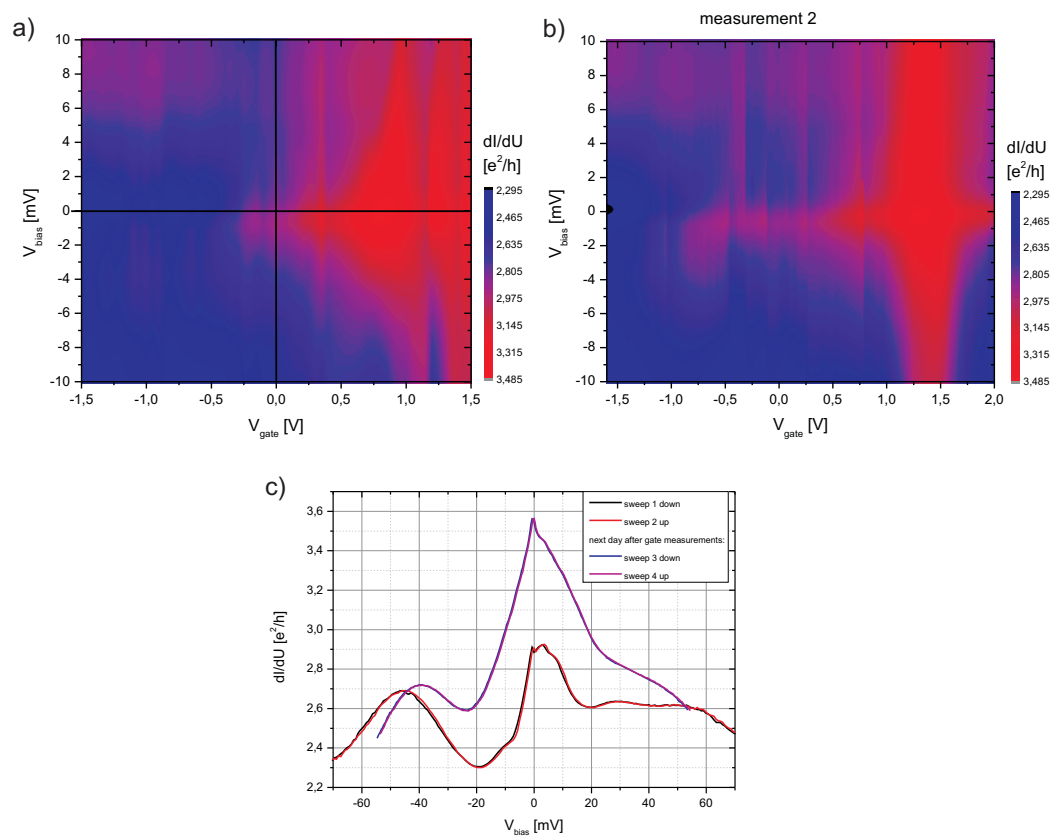
Figure 6.24: *a) Stability diagram of the differential conductance. A Coulomb diamond structure is visible. b) The same measurement performed one day later: The form and the position of the diamond have slightly changed. c) Bias voltage sweeps corresponding to the stability diagrams above. Here the change from one to the next day is also visible.*
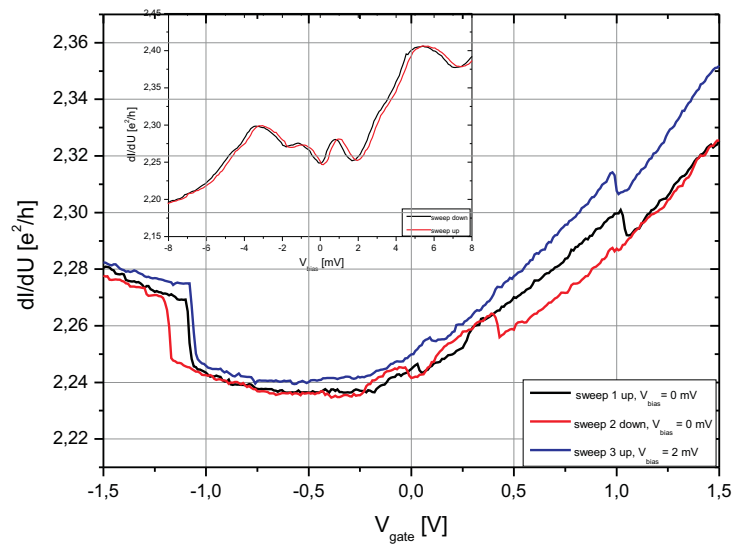
Figure 6.25: *Gate voltage sweep for different bias voltages. The curves shows jumps indicating a not properly working gate electrode. The inset shows the conductance in dependence on the bias voltage.*

visible in figure 6.23 and 6.24 are irregular. It follows that these structures do not come from gold grains. Hence, it can be deduced that a single-molecule or several molecules are measured.

6.4.2   Magnetic field dependence

The structures which showed a signature in the bias voltage sweeps were further measured in magnetic fields. Only five nanogaps showed a splitting when applying a magnetic field (figure 6.26 to figure 6.27). The interpretation of the results is very difficult because the values of the differential conductance are between 2.0 x 10^{-4} and 3.6 $\frac{e^2}{h}$. The positions of the peaks on the bias voltage axis, which are splitting in magnetic fields, are presented in table 6.2. Only the first structure shows a splitting in the color plot: $\Delta V_{bias} = (2.7 \pm 0.1)$

structure	peak position in mV	differential conductance in $\frac{e^2}{h}$
figure 6.26	-2.1	2.05
figure 6.29	-1.0	0.64
figure 6.28 a)	-1.0	0.63
figure 6.28 c)	-0.4	3.57
figure 6.27	33.0	1.1 x 10^{-3}

Table 6.2: *Summary of the peak positions and values of the differential conductance for the five structures which showed splitting in the magnetic fields.*

mV and $\Delta B = (8.0 \pm 0.1)$. The Landé-factor can be calculated with equation 6.2: g = $(5{,}8 \pm 0.1)$.

The second and the third structure in table 6.2 have similar values, but they showed no clear splitting in the color plot of the magnetic field (see figure 6.28 b)). The Landé-factor differs from the results of the C_{60} molecules, it could be characteristic for the pentaphenylene molecules.
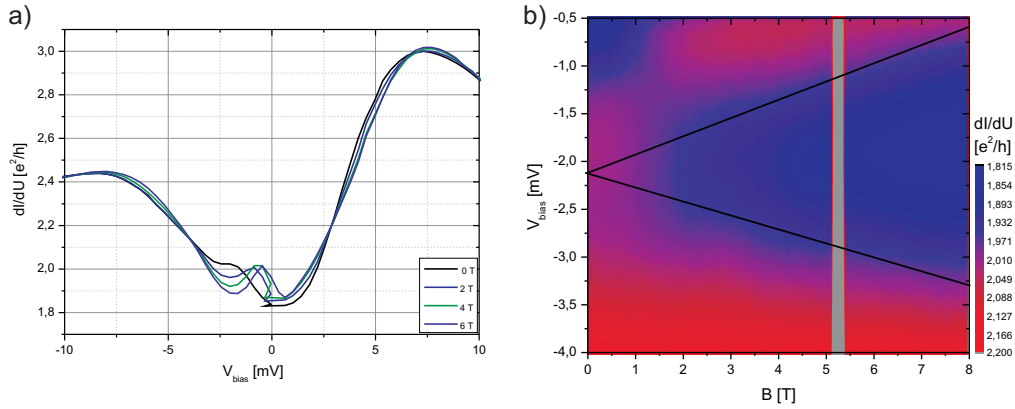
Figure 6.26: *a) Bias voltage sweeps for different magnetic fields: The black curve is measured without magnetic field. The other three curves show a shift and a different form of the peak at -2.0 mV. b) Color plot of the differential conductance: the splitting of the peak is clearly visible. The gray, vertical bar indicates a problem in the measurement. The values of the differential conductance were shifted to higher values than $2.2 \frac{e^2}{h}$. This could have been happened due to a unknown temperature shift during the measurement.*
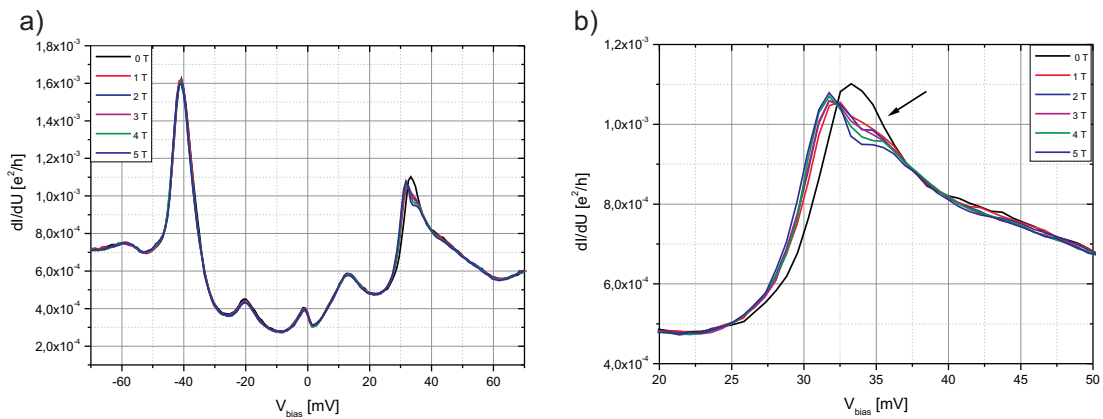

Figure 6.27: *a) Bias voltage sweeps in dependence of the magnetic field. For high magnetic field the peak at 35 mV forms a shoulder on the right side. b) Zoom of the peak: for more than 2 T the shoulder of the peak is formed.*
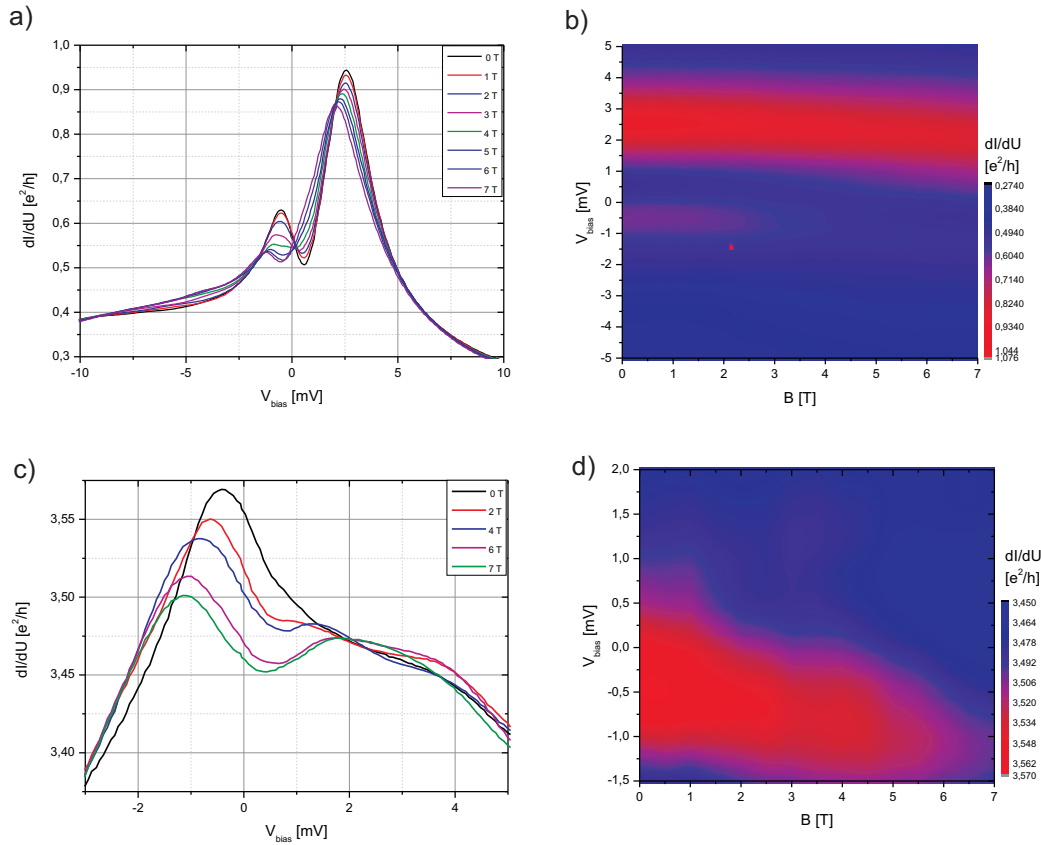
Figure 6.28: *a) Bias voltage sweeps for different magnetic fields. The peak and his smaller shoulder on the left side become smaller and shift to the left side for higher magnetic fields. b) Color plot of the differential conductance in dependence on the applied magnetic field and the swept bias voltage. There is no clear splitting of the conductance peak visible. The small peak for negative bias voltages vanishes for higher magnetic fields. The corresponding bias and gate voltage sweeps are illustrated in figure 6.22. c) Bias voltage sweeps in dependence on the magnetic field for another structure with similar behavior: for higher magnetic fields a small shoulder on the right side of the peak is formed. d) Color plot of the differential conductance in dependence on the applied magnetic field and the swept bias voltage: the peak on the left side decreases for high magnetic fields.*
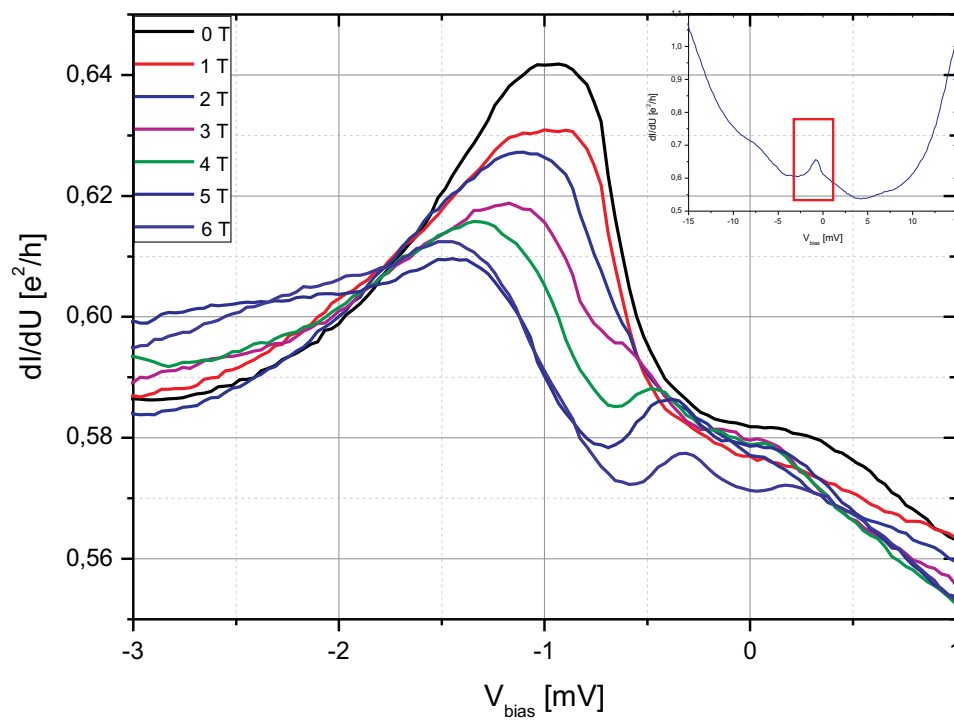
Figure 6.29: *a) Bias voltage sweeps for different magnetic fields. A second peak is formed for fields higher than 3 T. The inset shows the complete range of the bias voltage sweep at zero field. The red frame shows the voltage range for the sweeps in magnetic field.*

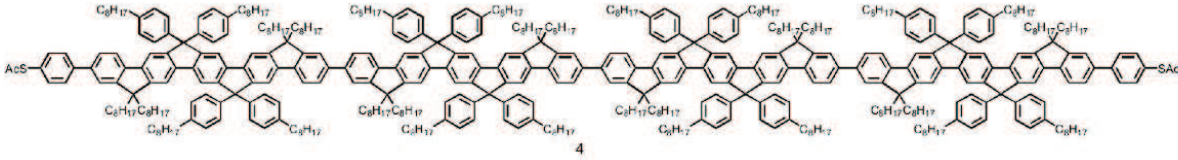# 6.5   Measurements of long chain molecules

Figure 6.30: *Chemical structure of the long chain pentaphenylene molecules, with courtesy of Prof. Dr. Klaus Muellen, MPI Mainz.*

6.5.1   Bias dependence

On one sample the long chain Pentaphenylene molecules (see figure 6.30) are applied out of a 0,1 mol solution and measured at base temperature of the dilution refrigerator. Only 4 out of 20 structures showed a measurable signal. The values of the differential conductance were very different for all four nanocontacts. The range of the differential conductance was from 0.011 to 9.0 $\frac{e^2}{h}$. The results of the bias voltage sweeps without an applied gate voltage or magnetic field are shown in figure 6.31 and 6.32. The position of the peaks for the first three structures is near to 0 V. The fourth nanocontact shows a different behavior. It is comparable to curves shown in figure 6.14 in section 6.2.1 above. The shifts in the differential conductance in figure 6.31 b) and 6.32 b) can be explained by the fact that the different sweeps were made on different days and the temperature of the cryostat may have changed. But it is clearly visible that the curves show the same features and peaks at reproducible values of the bias voltage for the different sweeps.

It was not possible to apply gate voltages to these structures due to a leakage in the gate oxide. This problem occurred after the electromigration. The reasons are too high electromigration currents, which can destroy the thin gate oxide layer. For further measurements it is proposed to electromigrate only one structure and to characterise this nanogap before further electromigration is performed.

6.5.2   Magnetic field dependence

The four nanostructures which showed measurable signal in the bias voltage sweeps, were also measured in dependence on magnetic fields. Only the last two structures showed a change in the curves (see figure 6.32 a) and b)). In figure 6.33 the bias voltage sweeps at different magnetic fields are shown. There is only a small shift in the position of the minimum visible, but no splitting of the peak.

The other structure shows a clear splitting of the signal in dependence on the magnetic field (see figure 6.34 b). The color plot shows a splitting which gives the values for the
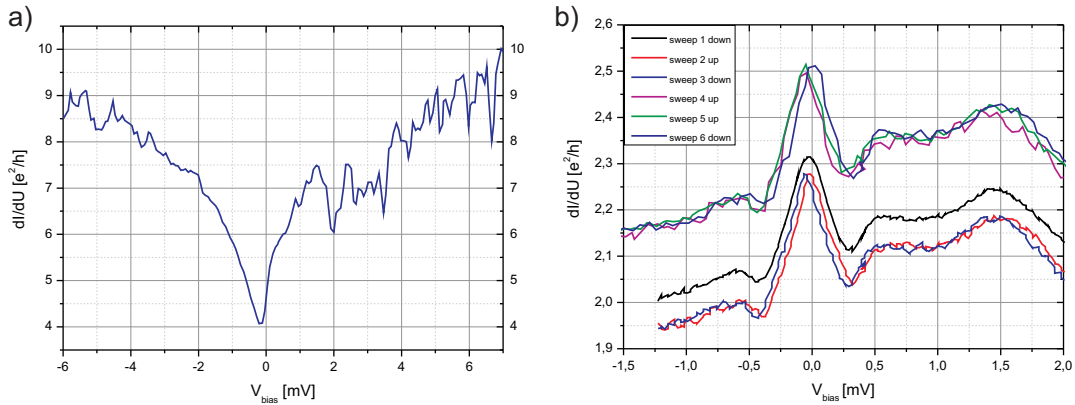
Figure 6.31: *a) Bias voltage sweep: the structure shows a minimum near 0 V. b) Bias voltage sweeps of another structure. This nanogap shows a peak at 0 V. The measurements were performed on different days. The position of the peak stays constant whereas the values for the differential conductance changes. This can be due to temperature differences in the cryostat.*
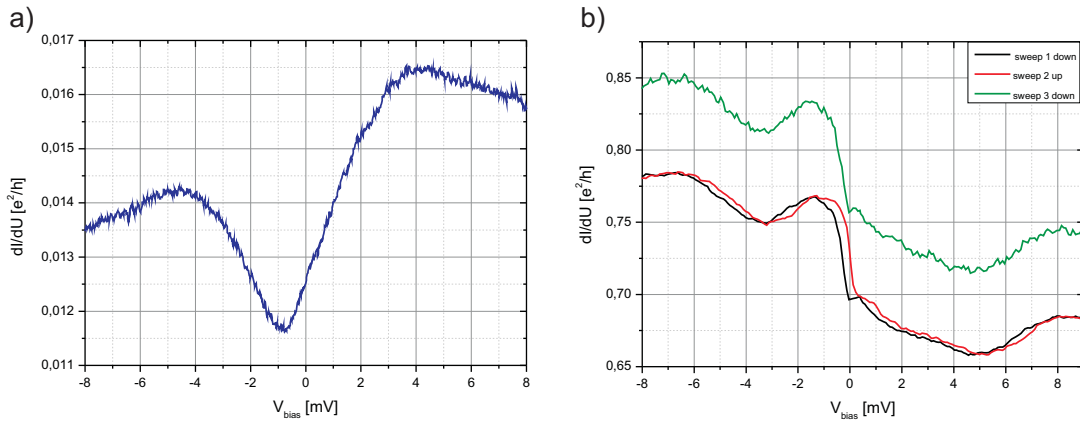

Figure 6.32: *a) Bias voltage sweep for the next structure: here again a minimum at - 1 mV is visible. The value of the differential conductance is much lower than for the other three nanogaps. b) Bias voltage sweeps of the last nanostructure: the differential conductance shows an ascending slope like in figure 6.14. The green curve was measured after the magnetic field measurements one day later. The shift can come due to a different temperature in the cryostat.*

calculation of the Landé-factor: $\Delta V_{bias} = (2.2 \pm 0.1)$ mV and $\Delta B = (11.0 \pm 0.1)$. The Landé-factor can be calculated with equation 6.1: g $= (3.5 \pm 0.5)$. This value is in the same range than the values of the buckyball molecules of table 6.1 in section 6.2.3. Osorio et al. found a g-factor of 2.56 for OPV-5 (oligophenylenevinylene molecules) [22]. These molecules are chains with five benzene rings and an easier construct than the
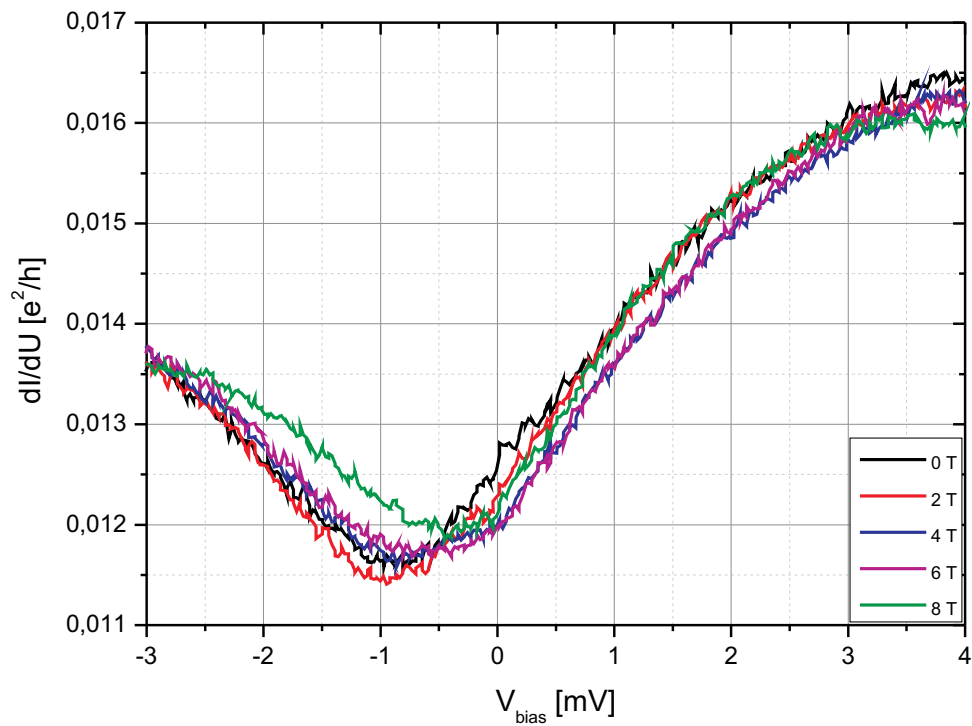
Figure 6.33: *Bias voltage sweeps at different magnetic fields. There is only a small shift of the minimum to higher bias voltages visible.*
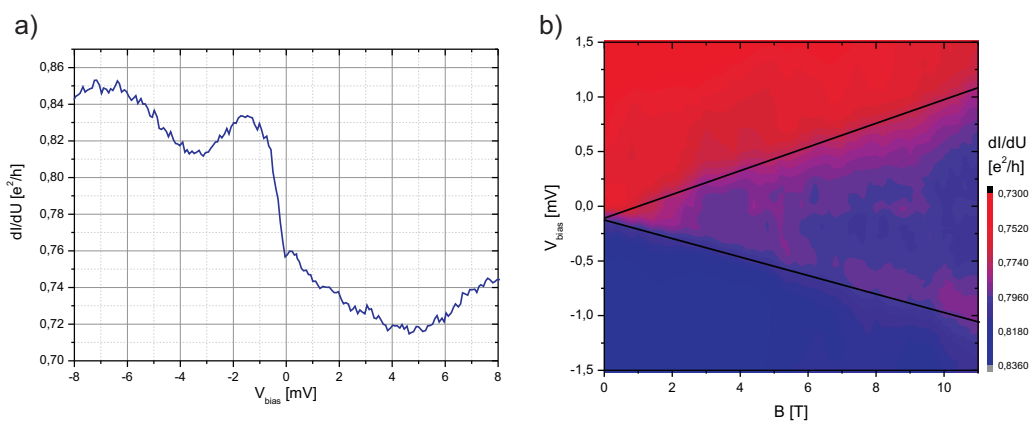
pentaphenylenes used here.

Figure 6.34: *Map of the differential conductance in dependence on the bias voltage and the magnetic field.*

Chapter 7

Conclusion and outlook

High resolution electron-beam lithography combined with the use of special resists makes it possible to structure electrodes with separations of a few nanometer. With this technologies it is possible to contact single molecules directly. Electrodes with a separation of less than 3 nm are presented. The processing for these structures is very delicate, but works reliably. This method provides the means to contact single molecules or also small graphene flakes directly.

Furthermore, a reliable process for the fabrication of nanostructures through electromigration is presented. The fabrication process of the three-dimensional devices is very stable and the geometry of the structures can be optimized by tuning the evaporation processes. The process of electromigration is investigated for our structures in detail and some process parameters are changed to our structures. These measures lead to an higher yield of good structures than previously reported [45], [50] or [51].

Single molecules are measured and the results are discussed. Due to the good yield after electromigration it was possible to measure multiple molecules in a short time. The measurements on buckyballs showed that our set-up is able to measure Kondo effect and Zeeman splitting. The distinction between gold grains after electromigration or real molecules in the gap is difficult due to problems with gate leakage currents. Here alternative methods for future measurements are proposed.

Finally, graphene-like molecules could be measured with our set-up. First results are presented. With the small number of structures measured with this molecules, the results are promising. The molecules seem to be a good candidate for measurements in the developed geometry.

For future experiments, the graphene discs (hexacoronene molecules) could be the most interesting type of molecules. With them the difference between chemical synthesized graphene, exfolitated graphene and with MBE grown graphene could be investigated. Moreover, the proposed devices gives the possibility to perform measurements on smaller features with a size of a few nanometer.

Appendix A

Temperature tests on photoresists

resist name	type +/-	(a) rpm/s	thickness μm	(b) min	(c) min	(d) min	(e) min	OK y/n
ARP5350	+	5000/40	0.9	105/5	2	7	10	n
ARU4040	+/-	5000/40	1.3	80/2	2	7	10	n
ARU4060S1	+/-	5000/40	0.6	80/2	2	7	10	y
SXARN4800/16	-	4000/40	0.8	85/5	2	7	10	y
ARN4340	-	5000/40	1.2	85/2	2	7	10	y
ARP3540	+	5000/40	1.2	105/2	2	7	10	n
ARP5460 ARP3540	+ +	2000/40 5000/40	1.4 1.2	150/5 100/2	8	10	0	n
ARP5460 ARP3540	+ +	5000/40 5000/40	0.9 1.2	150/5 100/2	8	10	0	n
ARP5480 ARP3540	+ +	2000/40 5000/40	0.7 1.2	150/5 100/2	8	10	0	n
ARP5480 ARP3540	+ +	5000/40 5000/40	0.5 1.2	150/5 100/2	8	10	0	n

Table A.1: **Thermal shock tests on optical resists.** After spin-coating (a) and baking (b) samples are transferred into the electron gun evaporation chamber and pumped down to about 10^{-5} mbar. Then the sample holder is cooled down to 77 K in about 2 minutes and kept there about minutes. In the next step, the sample holder is disconnected from the liquid nitrogen reservoir and flushed with room temperature nitrogen gas (c). A hot air gun is used to warm up the setup completely (d). After some relaxation time to get back to thermal equilibrium (e) the sample is taken out and examined by means of an optical microscope. These tests were performed during the diploma thesis of Simon Moser [40].

Appendix B

Single-Pixel-Lines

Gold single pixel lines	
resist bottom	Allresist AR-P 639 (50 K, 4 %)
spin coating	40 s @ 3000 rpm
baking	60 min @ 200 °C
resist top	Allresist PMMA AR-P 679 (950 K, 3 %)
spin coating	40 s @ 5000 rpm
baking	60 min @ 160 °C
exposure	EHT = 30 kV, aperture = 10 μm, magnification = 870,
	area dose = 1050 μC/cm^2, area step size = 10 nm
	line dose = 1350 - 1755 μC/cm^2, line step size = 2.5nm
	field size = 81.92 μm^2,
developer	isopropanol @ 25 °C
development	1 min
rinsing	1 min in deionized water
electron gun device	"Metallisierung"
Ti evaporation	$\perp$ 1 nm @ $\sim$ 0.03 nm/s, (upper chamber $\times$ 6.66)
Au evaporation	$\perp$ 10 nm @ $\sim$ 0.045 nm/s, (upper chamber $\times$ 6.66)
lift off	in acetone @ 50 °C over night, no ultrasonic
Step 2: creation of contact leads	

Table B.1: **Electron-beam lithography of the single-pixel-lines.** The sample is cleaned after the lithography process in an oxygen plasma to remove all organic contaminations from the samples.

Appendix C

Processes for Single-molecule transistor

In this appendix all processes for the fabrication of single-molecule transistor are described with all important details. First the cleaning process is described. The sample fabrication starts with two steps of optical lithography: the gold contact pads and the aluminum oxide gate. To create the nanoconstrictions there are different possibilities for the electron-beam lithography. The samples can be structured in one step of EBL and evaporated by shadow evaporation. This is the fastest way. It is also possible to write very small and thin lines. These lines have to be connected to the contact pads by a second EBL step. The exact preparation of the samples and the deposition of the molecules is described in table C.7. All processes are described in the following tables.

Preparations

Substrate and optical mask preparation	
Wafer cleavage	pieces of Si/SiO$_2$, $\sim 2.5 \times$ structure width
Wafer cleaning	5 min in acetone @ 50 °C, sonication
	5 min in isopropanol @ 50 °C, sonication
	10 min rinsing in deionized water
Mask cleaning	15 min in caro acid (H$_2$O$_2$: H$_2$SO$_4$ $\sim$ 1 : 4) @ 120 °C
	10 min rinsing in deionized water

Table C.1: **Substrate and mask preparation.** The slices of Si/SiO$_2$ wafer have to be big enough to guarantee homogeneous resist distribution. The mask has to be cleaned if necessary.

Optical lithography

Gold contact pads	
resist	Allresist AR-P 5350
spin coating	40 s @ 5000 rpm
baking	5 min @ 105 °C
UV exposure	$\sim$ 4.5 s @ UV
developer	AR-300-26 1:8 H_2O
development	15 - 20 s
electron gun evaporator	"Matallisierung"
Ti evaporation	$\perp$ 10 nm @ $\sim$ 0.2 nm/s, (lower chamber)
Au evaporation	$\perp$ 40 nm @ $\sim$ 0.5 nm/s, (lower chamber)
lift off	in acetone @ 50 °C for 30 min, sonication for 10 s

Table C.2: **Optical lithography of the gold contact pads.** The UV exposure time can change with the age and consistency of the used resist. For the gold evaporation the sample is mounted in the lower chamber of the evaporator.

Aluminum Gates	
resist	Allresist AR-U 4060
spin coating	40 s @ 5000 rpm
baking	2 min @ 94 °C
UV exposure	$\sim$ 6.5 s @ UV
developer	AR-300-26 1:4
development	15 - 20 s
electron gun device	"Käseglocke"
cooling	with LN_2 to about 77 K, let thermalise
Al evaporation	$\perp$ 25 nm @ 0.43 nm/s (cold chamber $\times$ 0.46)
warming up	30 min or longer low power hot air gun into LN_2-reservoir
oxidization	flood sample 30 min with $\sim$ 100 mbar O_2
	10 min with $\sim$ 1 mbar O_2-plasma @ 100 W
lift off	in acetone @ 50 °C over night, sonication if necessary

Table C.3: **Optical lithography of the aluminum oxide gates.** The UV exposure time can change with the age and consistency of the used resist. The sample holder is attached to the LN_2 reservoir. The crystal oscillator calibrated to another sample holder. Using the oscillator, there is 2.17 $\times$ more material on the sample than shown on the display. The second oxidation is done in the PICO plasma asher before the lift off process.

Electron-beam Lithography

Shadow evaporated gold nanoconstrictions	
resist bottom	Allresist PMMA/MA 33 % (AR-P 617 S1 (8 %))
spin coating	40 s @ 6000 rpm
baking	60 min @ 210 °C
resist top	Allresist PMMA AR-P 679 (950 K 3 %)
spin coating	40 s @ 6000 rpm
baking	60 min @ 180 °C
exposure	EHT = 30 kV, aperture = 30 μm, magnification = 870, electron current $\sim$ 0.235 nA, area dose = 1050 μC/cm^2, area step size = 5 nm, field size = 81.92 μm^2
developer	isopropanol @ 25 °C
development	1 min, dip sonication
rinsing	1 min in deionized water
electron gun device	"Metallisierung"
Ti evaporation	$\perp$ 2 nm @ $\sim$ 0.03 nm/s, (upper chamber $\times$ 6.6$\bar{6}$)
Au evaporation	+ 12.5 ° 7 nm @ $\sim$ 0.045 nm/s, (upper chamber $\times$ 6.6$\bar{6}$)
Au evaporation	$-$ 12.5 ° 7 nm @ $\sim$ 0.045 nm/s, (upper chamber $\times$ 6.6$\bar{6}$)
Au evaporation	$\perp$ 100 nm @ $\sim$ 0.5 nm/s, (lower chamber)
lift off	in acetone @ 50 °C over night, no ultrasonic

Table C.4: **Electron-beam lithography of the shadow evaporated constrictions.** The sample holder of the lower chamber is close to the evaporation source. The crystal oscillator is calibrated to this distance. The sample holder of the upper chamber is 1 m away from the evaporation source to avoid to heat up the sample during the evaporation. Using the oscillator, there is 6.6$\bar{6}$ $\times$ less material on the sample than shown on the display.

Shadow evaporated nanogaps	
resist bottom	Allresist PMMA 50 k (AR-P 639.04)
spin coating	40 s @ 3000 rpm
baking	60 min @ 200 °C
resist top	Allresist PMMA AR-P 679 (950 K 3 %)
spin coating	40 s @ 5000 rpm
baking	60 min @ 160 °C
exposure	EHT = 30 kV, aperture = 20 μm, magnification = 870, area dose = 1050 μC/cm^2, area step size = 10 nm field size = 81.92 μm^2
developer	isopropanol @ 25 °C
development	1 min
rinsing	1 min in deionized water
electron gun device	"Metallisierung"
Ti evaporation	$\perp$ 1 nm @ $\sim$ 0.1 nm/s, (upper chamber $\times$ 6.66), oxidized in load lock for 5 min
Au evaporation	+ 30 - 20 ° 7 - 10 nm @ $\sim$ 0.07 nm/s, (upper chamber $\times$ 6.66)
Au evaporation	$-$ 30 -20 ° 7 - 10 nm @ $\sim$ 0.07 nm/s, (upper chamber $\times$ 6.66)
Au evaporation	$\perp$ 100 nm @ $\sim$ 0.5 nm/s, (lower chamber)
lift off	in acetone @ 50 °C 30 min, in deionized water for 1 min

Table C.5: **Electron-beam lithography of the shadow evaporated nanogaps.** Samples with different evaporation angles and gold thicknesses are fabricated.

Lines	
Step 1: writing of the lines	
resist	Allresist PMMA AR-P 679 (950 K, 3 %)
spin coating	40 s @ 5000 rpm
baking	60 min @ 180 °C
exposure	EHT = 30 kV, aperture = 10 μm, magnification = 870,
	electron current $\sim$ 0.027 nA, field size = 81.92 μm^2,
	big structures: area dose = 500 μC/cm^2, area step size = 25 nm
	small structures: area dose = 540 - 790 μC/cm^2, area step size = 25 nm
developer	isopropanol @ 25 °C
development	1 min, dip sonication
rinsing	1 min in deionized water
electron gun device	"Metallisierung"
Au evaporation	$\perp$ 15 nm @ $\sim$ 0.045 nm/s, (upper chamber $\times$ 6.66)
lift off	in acetone @ 50 °C over night, no ultrasonic
Step 2: creation of contact leads	
resist bottom	Allresist PMMA/MA 33 % (AR-P 617 S1 (8 %))
spin coating	40 s @ 6000 rpm
baking	60 min @ 210 °C
resist top	Allresist PMMA AR-P 679 (950 K 3 %)
spin coating	40 s @ 6000 rpm
baking	60 min @ 180 °C
exposure	EHT = 30 kV, aperture = 30 μm, magnification = 870,
	electron current $\sim$ 0.235 nA, area dose = 500 μC/cm^2,
	area step size = 10 nm, field size = 81.92 μm^2
developer	isopropanol @ 25 °C
development	1 min, dip sonication
rinsing	1 min in deionized water
electron gun device	"Metallisierung"
Ti evaporation	$\perp$ 5 nm @ $\sim$ 0.2 nm/s, (lower chamber)
Au evaporation	$\perp$ 100 nm @ $\sim$ 0.5 nm/s, (lower chamber)
lift off	in acetone @ 50 °C over night, no ultrasonic
plasma incinerator	final cleaning 5 min in O$_2$-plasma @ 100 W

Table C.6: **Electron-beam lithography of small lines.** The sample is cleaned after the lithography process in an oxygen plasma to remove all organic contaminations from the samples.

Deposition of the molecules on the samples

Substrate preparation for the molecule deposition	
sample test	fast test of the sample resistance
	with the probe station in the clean room
	selection of a structure with 14 working constrictions
	(Resistance should be between 50 and 250 Ω)
protection layer	Allresist PMMA AR-P 679 (950 K 3 %)
spin coating	40 s @ 6000 rpm
baking	60 min @ 180 °C
cleaving	carefully cleaving the wafer in a suitable sized
	piece for the chip carrier
	with the selected structure in the middle
cleaning	1 h in acetone @ 50 °C
	5 min rinsing in deionized water
	5 min in O_2-plasma @ 100 W
molecule deposition	clean a pipette with solvent: toluene
	pipette a droplet of the molecule solution on the sample
	wait some seconds and then blow dry the sample with nitrogen
	repeat this process several times
mount in chip carrier	glue with G.E.vanish in a chip carrier,
	5 min @ 90 °C
bonding	gold contact pads: gold wire
	aluminum oxide gate: aluminum wire

Table C.7: **Sample preparation and molecule deposition.** The sample preparation and the molecule deposition has to be done very carefully. For cleaving the waver a resist protection layer is spun on the sample. This avoids the destruction of the nanostructures during the cleaving. The finished sample should be mounted in the cryostat as fast as possible.

Bibliography

[1] G. E. Moore. Cramming more components onto integrated circuits. *Electronics*, 38, 1965.

[2] Intel. Moores Law Inspires Intel Innovation. *online: http://www.intel.com/content/www/us/en/silicon-innovations/moores-law-technology.html*, 2011.

[3] A. Aviram and M. A. Ratner. Molecular rectifiers. *Chemical Physics Letters*, 29(2):277 – 283, 1974.

[4] H. S. J. Van der Zant, E. A. Osorio, M. Poot, and K. O'Neill. Electromigrated molecular junctions. *Physica Status Solidi B-basic Solid State Physics*, 243(13):3408–3412, November 2006.

[5] A. C. Grimsdale and K. Muellen. The Chemistry of Organic Nanomaterials. *Angewandte Chemie International Edition*, 44(35):5592–5629, 2005.

[6] C. W. J. Beenakker. Colloquium: Andreev reflection and Klein tunneling in graphene. *Rev. Mod. Phys.*, 80:1337–1354, Oct 2008.

[7] A. H. Castro Neto, F. Guinea, N. M. R. Peres, K. S. Novoselov, and A. K. Geim. The electronic properties of graphene. *Rev. Mod. Phys.*, 81:109–162, Jan 2009.

[8] K. S. Novoselov, A. K. Geim, S. V. Morozov, D. Jiang, Y. Zhang, S. V. Dubonos, I. V. Grigorieva, and A. A. Firsov. Electric Field Effect in Atomically Thin Carbon Films. *Science*, 306(5696):666–669, 2004.

[9] K. S. Novoselov, A. K. Geim, S. V. Morozov, D. Jiang, M. I. Katsnelson, I. V. Grigorieva, S. V. Dubonos, and A. A. Firsov. Two-dimensional gas of massless Dirac fermions in graphene. *Nature*, 438(7065):197–200, November 2005.

[10] A. K. Geim and K. S. Novoselov. The rise of graphene. *Nat Mater*, 6(3):183–191, March 2007.

[11] Y. Zhang, Y. Tan, H. L. Stormer, and P. Kim. Experimental observation of the quantum Hall effect and Berry's phase in graphene. *Nature*, 438(7065):201–204, November 2005.

[12] N. Tombros, C. Jozsa, Mi. Popinciuc, H. T. Jonkman, and B. J. van Wees. Electronic spin transport and spin precession in single graphene layers at room temperature. *Nature*, 448(7153):571–574, August 2007.

[13] K. I. Bolotin, K. J. Sikes, Z. Jiang, M. Klima, G. Fudenberg, J. Hone, P. Kim, and H. L. Stormer. Ultrahigh electron mobility in suspended graphene. *Solid State Communications*, 146(9-10):351 – 355, 2008.

[14] C. Stampfer, E. Schurtenberger, F. Molitor, J. Güttinger, T. Ihn, and K. Ensslin. Tunable Graphene Single Electron Transistor. *Nano Letters*, 8(8):2378–2383, 2008. PMID: 18642958.

[15] C. Stampfer, J. Güttinger, S. Hellmüller, F. Molitor, K. Ensslin, and T. Ihn. Energy Gaps in Etched Graphene Nanoribbons. *Phys. Rev. Lett.*, 102:056403, Feb 2009.

[16] F. Molitor, S. Droscher, J. Güttinger, A. Jacobsen, C. Stampfer, T. Ihn, and K. Ensslin. Transport through graphene double dots. *Applied Physics Letters*, 94(22):222107, 2009.

[17] E. A. Osorio, T. Bjornholm, J.-M. Lehn, M. Ruben, and H. S. J. van der Zant. Single-molecule transport in three-terminal devices. *Journal of Physics: Condensed Matter*, 20(37):374121, 2008.

[18] C. W. J. Beenakker. Theory of Coulomb-blockade oscillations in the conductance of a quantum dot. *Phys. Rev. B*, 44:1646–1656, Jul 1991.

[19] L. P. Kouwenhoven, D. G. Austing, and S. Tarucha. Few-electron quantum dots. *Reports on Progress in Physics*, 64(6):701, 2001.

[20] I. L. Aleiner, P. W. Brouwer, and L. I. Glazman. Quantum effects in Coulomb blockade. *Physics Reports*, 358(5-6):309 – 440, 2002.

[21] A. Nitzan and M. A. Ratner. Electron Transport in Molecular Wire Junctions. *Science*, 300(5624):1384–1389, 2003.

[22] E. A. Osorio, K.n O'Neill, M. Wegewijs, N. Stuhr-Hansen, J. Paaske, T. Bjornholm, and H. S. J. van der Zant. Electronic Excitations of a Single Molecule Contacted in a Three-Terminal Configuration. *Nano Letters*, 7(11):3336–3342, November 2007.

[23] L. P. Kouwenhoven, N. C. van der Vaart, A. T. Johnson, W. Kool, C. J. P. M. Harmans, J. G. Williamson, A. A. M. Staring, and C. T. Foxon. Single electron charging effects in semiconductor quantum dots. *Zeitschrift für Physik B Condensed Matter*, 85:367–373, 1991. 10.1007/BF01307632.

[24] S. De Franceschi, S. Sasaki, J. M. Elzerman, W. G. van der Wiel, S. Tarucha, and L. P. Kouwenhoven. Electron Cotunneling in a Semiconductor Quantum Dot. *Phys. Rev. Lett.*, 86:878–881, Jan 2001.

[25] Y. Selzer and D. L. Allara. Single-Molecule Electrical Junctions. *Annual Review of Physical Chemistry*, 57(1):593–623, 2006.

[26] J. Kondo. Resistance Minimum in Diluted Magnetic Alloys. *Progress of Theoretical Physics*, 32:37, Oct 1964.

[27] W. G. van der Wiel, S. De Franceschi, J. M. Elzerman, T. Fujisawa, S. Tarucha, and L. P. Kouwenhoven. Electron transport through double quantum dots. *Rev. Mod. Phys.*, 75:1–22, Dec 2002.

[28] N. Roch, C. B. Winkelmann, S. Florens, V. Bouchiat, W. Wernsdorfer, and F. Balestro. Kondo effects in a C60 single-molecule transistor. *physica status solidi (b)*, 245(10):1994–1997, 2008.

[29] W. H. Green, S. M. Gorun, G. Fitzgerald, P. W. Fowler, A. Ceulemans, and B. C. Titeca. Electronic Structures and Geometries of C60 Anions via Density Functional Calculations. *The Journal of Physical Chemistry*, 100(36):14892–14898, 1996.

[30] G. Seifert, K. Vietze, and R. Schmidt. Ionization energies of fullerenes - size and charge dependence. *Journal of Physics B: Atomic, Molecular and Optical Physics*, 29(21):5183, 1996.

[31] K. Kaasbjerg, K.and Flensberg. Strong Polarization-Induced Reduction of Addition Energies in Single-Molecule Nanojunctions. *Nano Letters*, 8(11):3809–3814, 2008. PMID: 18954146.

[32] K. S. Thygesen and A. Rubio. Renormalization of Molecular Quasiparticle Levels at Metal-Molecule Interfaces: Trends across Binding Regimes. *Phys. Rev. Lett.*, 102:046802, Jan 2009.

[33] L. H. Yu and D. Natelson. The Kondo Effect in C60 Single-Molecule Transistors. *Nano Letters*, 4(1):79–83, 2004.

[34] N. Roch, S. Florens, V. Bouchiat, W. Wernsdorfer, and F. Balestro. Out-of-Equilibrium Singlet-Triplet Kondo Effect in a Single C60 Quantum Dot. *Journal of Low Temperature Physics*, 153:350–358, 2008. 10.1007/s10909-008-9840-4.

[35] J. Güttinger, T. Frey, C. Stampfer, T. Ihn, and K. Ensslin. Spin States in Graphene Quantum Dots. *Phys. Rev. Lett.*, 105:116801, Sep 2010.

[36] Allresist. PMMA Polymere: 50K, 200K, 600K, 950K als E-Beam Resistserien AR-P 631, 641, 661, 671. online: http://www.allresist.de, January 2008.

[37] Allresist. Copolymer PMMA/MA 33 % als E-Beam Resistserien AP-R 617. online: http://www.allresist.de, January 2008.

[38] W. M. Moreau. *Semiconductor Lithography*. Plenum Press, 1988.

[39] Allresist. Thermostabiler Photoresist X AR-P 3220/7. online: http://www.allresist.de, January 2007.

[40] S. K. Moser. Nanostructures for Transport Measurements in Single Molecule Transistors. *Diplomarbeit, Physikalisches Insitut der Julius-Maximilians-Universität Würzburg*, 2010.

[41] D. F. Kyser and N. S. Viswanathan. Monte Carlo simulation of spatially distributed beams in electron-beam lithography. *Journal of Vacuum Science and Technology*, 12(6):1305–1308, 1975.

[42] F. Lehmann, G. Richter, T. Borzenko, V. Hock, G. Schmidt, and L. W. Molenkamp. Fabrication of sub-10-nm Au-Pd structures using 30 keV electron beam lithography and lift-off. *Microelectronic Engineering*, 65(3):327 – 333, 2003.

[43] F. Lehmann. *Prozessierung und elektrische Charakterisierung von ZnSe Heterostrukturen in verschiedenen Messgeometrien zum eindeutigen Nachweis der elektrischen Spininjektion.* PhD thesis, Julius-Maximilians-Universität Würzburg, 2005.

[44] H. S. J. van der Zant, Y. V. Kervennic, M. Poot, K. O'Neill, Z. de Groot, J. M. Thijssen, H. B. Heersche, N. Stuhr-Hansen, T. Bjornholm, D. Vanmaekelbergh, C. A. van Walree, and L. W. Jenneskens. Molecular three-terminal devices: fabrication and measurements. *Faraday Discussions*, 131:347–356, 2006.

[45] E. A. Osorio, K. O'Neill, N. Stuhr-Hansen, O. F. Nielsen, T. Bjornholm, and H. S. J. van der Zant. Addition Energies and Vibrational Fine Structure Measured in Electromigrated Single-Molecule Junctions Based on an Oligophenylenevinylene Derivative. *Advanced Materials*, 19(2):281–285, 2007.

[46] N. Roch, S. Florens, V. Bouchiat, W. Wernsdorfer, and F. Balestro. Quantum phase transition in a single-molecule quantum dot. *Nature*, 453(7195):633–637, May 2008.

[47] Allresist. Photoresistsystem für Lift-off-Technik AR-P 5300. online: http://www.allresist.de, January 2009.

[48] C. A. M. Knechten. *Plasma Oxidation for Magnetic Tunnel Junctions*. PhD thesis, Technische Universiteit Eindhoven, 2004.

[49] Allresist. Image Reversal Resistsystem AR-U 4000. online: http://www.allresist.de, January 2007.

[50] H. Park, A. K. L. Lim, A. P. Alivisatos, J. Park, and P. L. McEuen. Fabrication of metallic electrodes with nanometer separation by electromigration. *Applied Physics Letters*, 75(2):301–303, 1999.

[51] D. R. Strachan, D. E. Smith, D. E. Johnston, T.-H. Park, Michael J. Therien, D. A. Bonnell, and A. T. Johnson. Controlled fabrication of nanogaps in ambient environment for molecular electronics. *Applied Physics Letters*, 86(4):043109, 2005.

[52] A. R. Champagne, A. N. Pasupathy, and D. C. Ralph. Mechanically Adjustable and Electrically Gated Single-Molecule Transistors. *Nano Letters*, 5(2):305–308, 2005.

[53] Y.-V. Kervennic, J. M. Thijssen, D. Vanmaekelbergh, R. Dabirian, L.W. Jenneskens, C. A. van Walree, and H. S. J. van der Zant. Charge Transport in Three-Terminal Molecular Junctions Incorporating Sulfur-End-Functionalized Tercyclohexylidene Spacers. *Angewandte Chemie International Edition*, 45(16):2540–2542, 2006.

[54] J. R. Black. Electromigration failure modes in aluminium metallization for semiconductor devices. *Proceedings of the IEEE*, 57:1587 – 1594, 1969.

[55] I. A. Blech and E. S. Meieran. Electromigration in Thin Al Films. *Journal of Applied Physics*, 40(2):485–491, 1969.

[56] E. Kinsbron, I. A. Blech, and Y. Komem. The threshold current density and incubation time to electromigration in gold films. *Thin Solid Films*, 46(2):139 – 150, 1977.

[57] J. R. Lloyd. Electromigration in thin film conductors. *Semiconductor Science and Technology*, 12(10):1177, 1997.

[58] R. S. Sorbello. Theory of Electromigration. volume 51 of *Solid State Physics*, pages 159 – 231. Academic Press, 1997.

[59] H. B. Huntington and A. R. Grone. Current-induced marker motion in gold wires. *Journal of Physics and Chemistry of Solids*, 20(1-2):76 – 87, 1961.

[60] M. Araidai and M. Tsukada. Diffusion processes in single-atom electromigration along a gold chain: First-principles calculations. *Phys. Rev. B*, 80:045417, Jul 2009.

[61] P. Fries. Herstellung von Nanokontakten zur Einzelmolekülmessung. *Diplomarbeit, Physikalisches Insitut der Julius-Maximilians-Universität Würzburg*, 2007.

[62] *ADwin-light-16 Handbuch Version 3.0, November 2007, Jäger Computergesteuerte Messtechnik*, 2007.

[63] R. Vogelgesang. Lock-In Amplifier Theory. *online: http://www.nanoopt.org/teaching/personal-lecture-notes/165-lock-in-amplifier-theory.html*, 2004.

[64] Kempf A. Konsistenzmessungen an Einzelmolekültransitoren. *Bachelor Arbeit, Physikalisches Insitut der Universität Würzburg*, 2010.

[65] D. Davidovic and M. Tinkham. Spectroscopy, Interactions, and Level Splittings in Au Nanoparticles. *Phys. Rev. Lett.*, 83:1644–1647, Aug 1999.

[66] J. R. Petta and D. C. Ralph. Studies of Spin-Orbit Scattering in Noble-Metal Nanoparticles Using Energy-Level Tunneling Spectroscopy. *Phys. Rev. Lett.*, 87:266801, Dec 2001.

[67] P. Monod and A. Janossy. Conduction electron spin resonance in gold. *Journal of Low Temperature Physics*, 26:311–316, 1977. 10.1007/BF00654575.

[68] A. A. Houck, J. Labaziewicz, E. K. Chan, J. A. Folk, and I. L. Chuang. Kondo Effect in Electromigrated Gold Break Junctions. *Nano Letters*, 5(9):1685–1688, 2005.

[69] D. R. Ward, G. D. Scott, Z. K. Keane, N. J. Halas, and D. Natelson. Electronic and optical properties of electromigrated molecular junctions. *Journal of Physics: Condensed Matter*, 20(37):374118, 2008.

[70] K. O'Neill, E. A. Osorio, and H. S. J. van der Zant. Self-breaking in planar few-atom Au constrictions for nanometer-spaced electrodes. *Applied Physics Letters*, 90(13):133109, 2007.

Acknowledgements

There are lots of people I would like to thank for their contributions to this work.